Nonlinear deformations of a thick-walled hyperelastic tube under external pressure

by

Yunfei Zhu

A thesis submitted to the

Faculty of Information and Mathematical Sciences

at the University of Glasgow

for the degree of

Doctor of Philosophy

December 2009

Abstract

This research deals with several novel aspects of the nonlinear behaviour of thick-walled cylindrical hyperelastic tubes under external pressure.

Initially, we consider bifurcation from a circular cylindrical deformed configuration of a thick-walled circular cylindrical tube of incompressible isotropic elastic material subject to combined axial loading and external pressure. In particular, we examine both axisymmetric and asymmetric modes of bifurcation. The analysis is based on the three-dimensional incremental equilibrium equations, which are derived and then solved numerically for a specific material model using the Adams-Moulton method. We assess the effects of wall-thickness and the ratio of length to (external) radius on the bifurcation behaviour.

The problem of the finite axisymmetric deformation of a thick-walled circular cylindrical elastic tube subject to pressure on its external lateral boundaries and zero displacement on its ends is formulated for an incompressible isotropic neo-Hookean material. The formulation is fully nonlinear and can accommodate large strains and large displacements. The governing system of nonlinear partial differential equations is derived and then solved numerically using the C++ based object-oriented finite element library Libmesh. The weighted residual-Galerkin method and the Newton-Krylov nonlinear solver are adopted for solving the governing equations. Since the nonlinear problem is highly sensitive to small changes in the numerical scheme, convergence was obtained only when the analytical Jacobian matrix was used. A Lagrangian mesh is used to discretize the governing partial differential equations. Results are presented for different parameters, such as wall thickness and aspect ratio, and comparison is made with the corresponding linear elasticity formulation of the problem, the results of which agree with those of the nonlinear formulation only for small external pressure. Not surprisingly, the nonlinear results depart significantly from the linear ones for larger values of the pressure and when the strains in the tube wall become large. Typical nonlinear characteristics exhibited are the "corner

bulging" of short tubes, and multiple modes of deformation for longer tubes.

Finally the general fully nonlinear governing equations in Lagrangian form for the three dimensional large deformations of an elastic tube under external pressure are developed.

Acknowledgements

I would like to thank my supervisors, Professor Xiaoyu Luo and Professor Ray W. Ogden, for their continued support and advice through out the period of this study. I feel extremely fortunate to have been given the chance to work under them as a postgraduate and to continue working with them as a research assistant. I am also grateful to the Overseas Research Students Awards Scheme, and the Faculty of Information and Mathematical Science, and the Department of Mathematics at Glasgow University for the generous scholarships.

I also wish to thank Dr. David Haughton, University of Glasgow, and Professor Chris Berttram, University of New South Wales, for their valuable advice on Chapter 4. I also want to express my appreciation to Libmesh developers at the University of Texas and Dr. Boyce Griffith at New York University for their help with using Libmesh.

My parents and elder sister deserve the deepest thanks for their never-ending support during my education.

Finally, I would like to thank the cool kids in my office, such as Robert, Stephen, Ehsan, Susan, Monica and Marjory for their help in the last three years.

Contents

Chapter 1

Introduction

In this thesis, we focus on modelling and simulating the collapse of a cylindrical tube under external pressure. The collapse of a circular tube is of interest not only in many engineering applications, such as in the design of undersea or underground pipelines and pressure vessels, particularly submarine structures, but it is also of great interest in the biomechanics context.

The main motivation for this research comes from the investigation of the behaviour of physiological conduits within our body subject to external pressure, such as veins and arteries conveying blood flow and large bronchi conducting air into the lungs. Due to the high flexibility of the soft biological tissue, these conduits may collapse under certain conditions of external and internal fluid pressure. For example, intramyocardial arteries collapse during systole [29]. More generally, the collapse of cardiovascular vessels plays an important role in the delivery of blood to other organs [30], [63]. A long cylindrical elastic tube when subjected to a transmural (internal minus external) pressure may collapse into a two-lobed configuration, as illustrated in Fig.1.1. In elastic buckling the collapse is usually sudden and catastrophic, which is a process involving some nonlinear dynamical deformations of great complexity. Depending on geometry, material properties, the pressure and boundary conditions, the tubes may collapse differently. In essence, these kinds of problems involve two physical systems interacting with each other, which are the elastic wall of the conduit and the biological fluid inside or around the conduit. Such systems are also known as coupled and such coupling may be weak or strong depending on the degree of interaction.

A general definition of coupled systems may be given as [80]
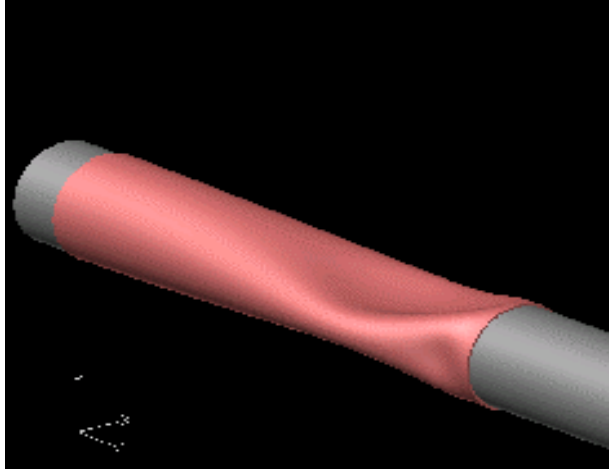
Figure 1.1: Collapsed tube (from paper by Marzo et al. [52]).

Definition 1.0.1 *Coupled systems and formulations are those applicable to multiple domains and dependent variables which usually but not always describe the different physical phenomena and in which*

(a) neither domain can be solved while separated from the other;

(b) neither set of dependent variables can be explicitly eliminated at the differential equation level.

The topic of flow through collapsible tubes, an obvious coupled problem, has been studied for several decades. This subject has been reviewed briefly by Kamm and Pedley [42]. Experiments [14], [12] on a Starling resistor prototype of the system have presented a rich dynamic behaviour, with various types of self-excited oscillations. One- or two-dimensional theoretical models has been established by Pedley [61], Luo [49], [50], [51], Cai [17] and Jensen [41] and much computational work has been carried out to reveal the mechanisms of such oscillations. Luo and Pedley [49] studied steady flow in a 2-D channel with one plane rigid wall and the other wall replaced by an elastic segment, which is treated as a elastic membrane, as illustrated in Fig.1.2. Following their previous work [49] on steady flow in a two-dimensional fluid-membrane model of the collapsible tube, Luo and Pedley [50] investigated the instability of the steady solution by developing a time-dependent simulation of the coupled flow-membrane problem. These studies provided a detailed picture of the fluid and solid mechanics involved in the large-amplitude self-excited oscillations in this simplified system and have shown rich dynamical behaviour of the system.
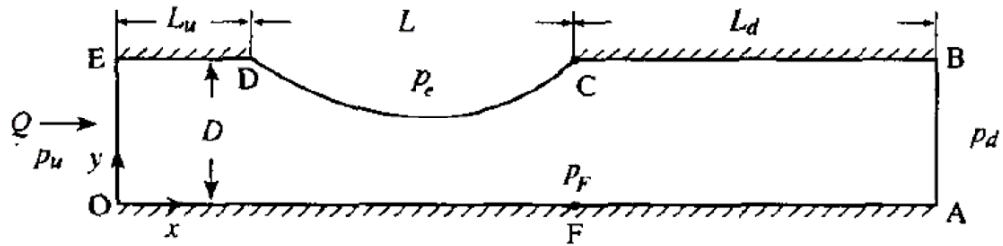
Figure 1.2: The geometry of a 2-D collapsible channel (from paper by Luo [48]).

To overcome the inadequacy of the fluid-membrane model on flow in collapsible chan-
nels, Cai and Luo [17] developed a fluid-beam model, which employs a plane strained
elastic beam with large deflection and incrementally linear extension. This model repre-
sents a more realistic and general description of the problem and can be reduced to several
simpler models including the fluid-membrane model under special parameter ranges. Both
asymptotic and numerical approaches are used to study the problem.

Heil investigated the steady deformations of the fully coupled three-dimensional system
in another series of studies [38], [36], [39]. The wall of the tube was modelled as a circular
cylindrical shell and geometrically nonlinear shell theory was used to describe the large non-
axisymmetric post-buckling deformation. The fluid flow was modelled by using lubrication
theory. But some of the assumptions used in the simplification of the fluid equations were
violated, which caused the wall slope at the downstream end to tend to be quite large,
after the buckling, although this model provides a very accurate description of the tube's
deformation. Heil [37] developed the entirely three-dimensional self-consistent model of the
viscous flow in a collapsible tube by abandoning the small-slope assumption and replacing
the lubrication theory by a solution of the steady three-dimensional Stokes equations which
describe the flow in arbitrary geometries at zero Reynolds number.

In order to develop a more general three-dimensional model requires one ultimately to
extend the Heil model [37] to replace the geometrically nonlinear shell theory by a theory
which can accommodate the large displacements (geometric nonlinearity) and as well as
large strains (material nonlinearity) and also to include the coupling of unsteady, three-
dimensional, nonlinear Navier-Stokes equations for oscillations to arise. Because of the
complexities and large computational requirements for the full three-dimensional solution
of the above problems, such a work, however, is still a daunting task. Although some
attempts have been made, self-excited oscillations are still not yet captured [71], [70], [65].

To reduce the complexity we simplify the actual physiological problem by replacing the transmural (internal minus external) pressure due to the flow in and out the tube by the external hydrostatic pressure P only. This simplification allows us to avoid tackling the fully coupled fluid-structure interactions and to focus on investigating the material and geometrical nonlinearity of the tubes. We consider the simplified problem in 3 stages

(1) Bifurcation analysis of thick-walled circular cylindrical elastic tubes under axial loading and external pressure.

(2) Nonlinear axisymmetric deformations of an elastic tube under external pressure.

(3) Nonlinear three-dimensional deformations of an elastic tube under external pressure.

We give a brief review of the stability analysis here. To gain a full understanding of this particular area, we refer to the recent review article by Fu and Ogden [26], in which they summarized the progress of development of the nonlinear stability analysis of thick elastic bodies subjected to finite elastic deformations. The stability of elastic shells has been analyzed over the course of the past century since the initial work on the topic by von Mises [72], who derived an equation for the buckling pressure of a thin-walled elastic tube. This gives the pressure as proportional to the cube of the ratio of wall thickness to mean diameter. Since then buckling of circular cylindrical tubes under external pressure based has been studied extensively, for instance by Batdorf [7], Nash [54] and Flügge [25]. In these studies, a simple one-term deflection function was used and the problem was solved under special boundary conditions. More accurate solutions were obtained by Ho [40], Sobel [66] and Yamaki [75] for a variety of loading and boundary conditions where the pre-buckling state was given in terms of membrane theory. The same problem was then treated by Yamaki [76] but with pre-buckling effects. His key finding was that the mode number of the most unstable mode increases as the tube length is decreased, and for a sufficiently long tube mode 2 bifurcation is the most unstable mode. The length of the tube at which the transition between the higher mode and mode 2 occurs, however, depends on the thickness ratio; the thicker the tube the shorter the length for which mode 2 becomes the most unstable mode [77]. Good agreement between these studies and various experiments [74] has led to the buckling prediction for a cylindrical tube being regarded as a solved problem (at least for thin shells).

With different emphases, related extensive studies on stabilities of circular cylindrical

shells have also been carried out. Some of these, concerning geometrically nonlinear vibrations and dynamics of circular cylindrical shells, were reviewed by Amabili [1], with and without fluid-structure interactions. Other recent advances in post-buckling analysis of thin-walled structures were reported by Kounadis [46]. With a particular interest in post-buckling behaviour, Heil and Pedley [39] examined the stability of cylindrical shells under external pressure using a geometrically non-linear shell theory and confirmed that the mode number of the most unstable mode increases as the tube length is decreased, as predicted by Yamaki [77]. Heil and Pedley [39] also found that the bifurcation is not significantly affected by the presence of a full fluid-solid coupling (as long as the critical loading is the same), although the subsequent post-buckling behaviour can be very different with and without the internal flow.

In experimental studies for these kinds of problems the tube wall thickness typically exceeds that which might be appropriate for thin-shell theories [10, 11, 13]. It is therefore reasonable to ask if the bifurcation predictions of the classical theories remain valid. Bertram [10] studied experimentally the effects of wall thickness on the collapse of tubes and obtained agreement with the results of [74]. In Bertram's study, wall thickness ratio h/R values used were 0.38 and 0.5, where h is the thickness and R is the internal radius. The thick-walled tube problem was also analyzed by Marzo [52] using the finite element method, and good agreement with the experiments of [10] and [74] was achieved. However, in [10] and [52] results were presented only for mode 2 bifurcation and for limited values of the wall thickness. Therefore, it remains unclear how far the bifurcation predictions of thin-shell theory can be extended to thick-walled tubes, for which nonlinear elastic deformations can no longer be neglected.

There is also an extensive literature on plastic buckling of circular tubes. Experimental and modelling aspects of the compression of steel tubes in the plastic regime have been reviewed in the recent works by Bardi [5] and [6]. They found that the carbon steel tubes may buckle into different modes as the increase of the external pressure. Figure 1.3 shows the plastic buckling of circular tubes under compression with axisymmetric collapse and non-axisymmetric collapse, with mode 2 and 3. This figure can give the reader directly an idea of the shape of the tube after axisymmetric or non-axisymmetric buckling. We refer to these papers for references to the relevant literature.

For problems involving nonlinear elastic deformations, a rigorous bifurcation theory has been established based on the analysis of infinitesimal deformations superimposed on
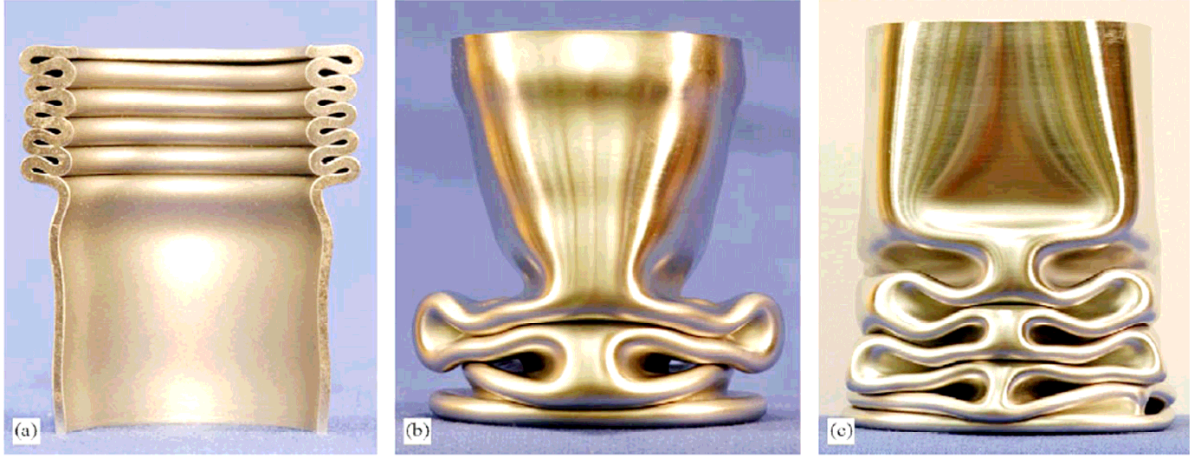
Figure 1.3: (a) Carbon steel tube that developed axisymmetric concertina folding, (b) mode 2 folding and (c) mode 3 folding of stainless steel tubes (from paper by Bardi [5]).

a known large deformation [28]. Using this theory, Nowinski and Shahinpoor [56] examined the stability of an infinitely long circular cylinder of neo-Hookean material under external pressure assuming a plane strain deformation, and Wang and Ertepinar [73] investigated the stability of infinitely long cylindrical shells and spherical shells subjected to both internal and external pressure. On the same basis but for different (incompressible, isotropic) material models Haughton and Ogden [35] examined in some detail the bifurcation behaviour of circular cylindrical tubes of finite length under *internal* pressure and axial loading.

Bifurcation from a circular cylindrical configuration of a thick-walled tube subject to combined axial loading and *external* pressure was investigated on the basis of the nonlinear theory of elasticity by Zhu et al. [78]. Our work showed that the wall thickness and aspect ratio play important roles in the occurrence of the most unstable bifurcation mode. Different from the results based on thin shell theories, which show that higher modes should occur for shorter tubes, Zhu et al. [78] showed that mode-2 becomes more persistent for shorter tubes if a suitable nonlinear model is used. This observation was in agreement with experimental findings on thick-walled tubes subject to external pressure, in particular those of [10, 11] and [13].

However, a limitation of this work is that the bifurcation analysis was initiated from a deformed circular cylindrical configuration of an elastic tube with rather special incremental boundary conditions imposed on the ends of the tube. Thus, the results only apply for the initial bifurcation behaviour, and might preclude realistic post-buckling behaviour

involving large displacements near the ends of the tube.

In many engineering and biomechanical applications cylindrical tubes are subject to external pressures and as a result undergo large (nonlinear) deformations. In another work we investigated the behaviour of thick-walled tubes with large deformations including large strains and large displacements under external pressure by deriving the general differential equations, free of unnecessary assumptions. This is a challenging work due to the lack of the good and general numerical methods for solving the final fully nonlinear differential equations we obtained based on the theory of nonlinear finite deformation and the large computational requirements for simulation of the full three dimensional problems, so initially, we assume the deformation is axisymmetric. Then, we will try to move forward to the full three-dimensional problems.

In early engineering approaches to the analysis of this problem it was typically assumed that the material response is linearly elastic, but this led to predictions which were inaccurate except for very small deformations. It is well known that for biological materials deformations of the order 50–100% can occur, and in this case a fully nonlinear problem formulation is essential. However, fully nonlinear material and geometrical analysis is challenging due to the difficulty of solving such problems. To facilitate solutions simplifications are often made, such as the adoption of thin shell theories, which have been successful for describing thin-walled structures [47, 75, 77]. Some researchers have focused on geometrically nonlinear problems, with small strains but large displacements, and this approach has often proved to be adequate. Erbay and Demiray [23] considered the finite axisymmetric deformation of a circular cylindrical tube of neo-Hookean material by using an asymptotic expansion method. Their perturbation solution is based on the smallness of the ratio of thickness to inner radius of the tube. Normal and tangential tractions were applied on the inner surface of the tube but no boundary conditions were considered at the ends of the tube. Heil [38] and Marzo [52] performed a numerical simulation of the post-buckling behaviour of tubes under external pressure.

Propagation of finite amplitude waves in fluid-filled elastic or viscoelastic thin-walled tubes has been investigated [64], [2], [53], and [23]. However, for thick-walled tubes there are few results available in the literature due to the difficulties arising from the variation of field quantities with the radial coordinate. Demiray studied weakly nonlinear waves in a fluid filled thick-walled elastic tube, first using an artificial estimated pressure dependence [20] on the axial coordinate, which was later improved upon [21].

The ability to predict the bifurcation character of the solutions is also an important practical problem. Negrón-Marrero [55] studied the bifurcation of the axisymmetric hyperelastic cylinders subject to nonlinear mixed boundary conditions and found that the eigenfunctions can be classified into those that are symmetric about the mid-plane, representing either necked or barrelled configurations of the cylinder, and those that break this symmetry. Finite axisymmetric deformations of thick-walled carbon-black filled rubber tubes were also studied experimentally by Beatty and Dadras [9]. They found that for aspect ratios less than 5 tubes exhibit radially or axially symmetric bulging modes of deformation, distinct from the familiar Euler buckling that occurs for longer tubes. Significantly, they found that the experimentally observed critical compression load is considerably lower than that predicted on the basis of the linear theory.

In chapter 2, we introduce the theory of nonlinear elasticity, which will be used throughout the thesis.

In chapter 3, the finite element process and techniques that are used in Chapter 5 are presented. Particular attention and details are provided to introduce the object-oriented finite element library libmesh, which will be adopted for solving the nonlinear partial differential equations in Chapters 5 and 6.

In chapter 4, following the analysis of [35], we consider the bifurcation of incompressible, isotropic thick-walled circular cylindrical tubes of finite length when subject to both axial loading and external pressure. A new feature of the present work is the combination of finite deformations of thick-walled tubes of hyperelastic material with *external* pressure and axial loading.

For the thinner tubes it is found that under external pressure axisymmetric bifurcation occurs only for $0 < \lambda_z < 1$, where λ_z is the principal stretch in the axial direction of the finite deformation. Moreover, the trend of the bifurcation curves is very different from that of a tube under internal pressure. Since externally pressurized tubes are particularly prone to asymmetric bifurcations, we devote most of our effort to the study of asymmetric bifurcations. The bifurcation modes are characterized by azimuthal mode number m and the tube length (which can be taken as a proxy for the axial mode number n). The bifurcation curves for modes $m = 1$ to $m = 4$ are presented, and the effects of wall thickness and the ratio of tube length to external radius on the buckling pressure are also examined. For the simpler cases, our results are in agreement with the published results in [52], [74], [10] and [73], and, in particular, with the von Mises equation [72, 74]. We

observe that the von Mises equation can only predict the buckling pressure well for thin shells. By contrast, the general analysis of bifurcation based on 3D finite deformation elasticity theory presented herein is valid for both thin and thick shells.

In chapter 5, we formulate the fully nonlinear problem of the large *axisymmetric* deformations of thick-walled cylindrical tubes of finite length made of incompressible hyperelastic material subject to zero displacements on the ends of the tube and hydrostatic pressure on the exterior of the lateral surface. The general governing differential equations that describe the deformation of the tube are derived, with both geometrical and material nonlinearity included. The corresponding radially symmetric and linear problems are also examined for the purpose of comparison. The sets of equations are solved numerically using the object-oriented C++ finite element package Libmesh. Results for tubes with different aspect ratios are presented to show how the wall thickness and tube length affect the nonlinear behaviour. The major findings are that for a short tube with smaller aspect ratio, the nonlinear deformation is characterized by a corner bulging, which changes all the stress distributions, especially for the shear stress. For longer tubes, the nonlinear model exhibits higher modes of deformation while for the corresponding linear model only mode-2 is present. The agreement between the linear and nonlinear models is only good for small values of the pressure, corresponding to maximum strains of about 5%.

In chapter 6, without any assumptions on the magnitude of the geometrical deformation or material nonlinearity we derived the general three dimensional governing equations for the large deformations of a thick-walled tube composed of incompressible isotropic elastic material in both cylindrical polar and Cartesian coordinates. Generally, it is convenient that we formulate our equations for a circular cylindrical tube based on cylindrical polar coordinates. However, we note that the expression of deformation gradient **F** in cylindrical polar coordinates is much more complex than the one in Cartesian coordinates and this complexity can be enlarged in the expression of nominal stress **S** and even the equilibrium equations. The form of the final equilibrium equations in cylindrical polar coordinates is also more complicated, with several redundant terms. Both of the complexities will add difficulty when the numerical discretization of the equation system and computations are carried out. In order to avoid the complexities in formulation, we prefer to adopt the corresponding Cartesian equation systems, although dealing with the boundary condition may seem to be not rational compared with an approach based on cylindrical polar coordinates. The only thing we need do is to get the expression of the unit normal to the internal and

external surfaces of the cylindrical tube. The corresponding linear equations in Cartesian coordinates are also presented for the purpose of comparison with the nonlinear ones.

Results from Chapters 4 and 5 have been published in International Journal of Solids and Structures [78] and European Journal of Mechanics A solids [79], respectively. Further results from Chapter 6 are still in preparation and will appear soon.

Chapter 2

Basic equations

In this chapter a brief summary of the static theory of nonlinear elasticity is given, including the analysis of deformation, strain, stress and the governing equations of equilibrium, and a short description of the constitutive equations for a Cauchy elastic material. For more important details we refer to the relevant literature such as the classic book by Ogden [60], in which a complete and precise account of the mathematical theory of non-linear elasticity with application to the analysis of the large elastic deformation of hyperelastic materials is presented and the book by Fu and Ogden [27], which provides not only fundamentals of nonlinear elasticity but also modern topics in this field.

2.1 Deformation

We will deal with deformations of elastic material in which both rotations and stretches are arbitrarily large, the so-called finite strain theory. In this case, a clear distinction is necessary to be made between undeformed and deformed configurations of an elastic body. Consider a deformable continuous body for which we take $\mathbf{X}$ to be the position vector of an arbitrary material point in the reference configuration, denoted by $\mathfrak{B}_r$. Similarly, in the current configuration, $\mathfrak{B}_t$ say, let $\mathbf{x}$ be the position vector of the same material point.

Suppose that the deformation from $\mathfrak{B}_r$ to $\mathfrak{B}_t$ is defined by the vector function $\boldsymbol{\chi}$, if there is no time dependence we have that (see Fig.2.1) $\mathbf{x} = \boldsymbol{\chi}(\mathbf{X})$. We assume that $\boldsymbol{\chi}$ is twice-continuously differentiable with respect to position here.

The displacement vector $\mathbf{u}$ is defined by

$$\mathbf{x} = \mathbf{X} + \mathbf{u}. \tag{2.1}$$
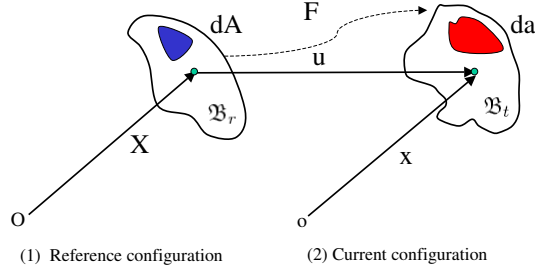
Figure 2.1: Reference and current configurations.

Then the deformation gradient tensor $\mathbf{F}$ is defined by

$$\mathbf{F} = \text{Grad}\,\mathbf{x}. \tag{2.2}$$

With respect to Cartesian basis vectors $\mathbf{E}_i$ in reference configuration and $\mathbf{e}_i$ in current configuration, we have

$$\mathbf{F} = \frac{\partial(x_i\mathbf{e}_i)}{\partial X_j} \otimes \mathbf{E}_j = \frac{\partial x_i}{\partial X_j}\mathbf{e}_i \otimes \mathbf{E}_j \quad i,j = 1,2,3. \tag{2.3}$$

The local ratio of current to reference volume is

$$J = \det \mathbf{F} > 0, \tag{2.4}$$

and for an incompressible material the constraint

$$J = \det \mathbf{F} \equiv 1 \tag{2.5}$$

must be satisfied for every material point $\mathbf{X}$.

For any non-singular second order tensor $\mathbf{F}$, we note that the tensor can be written uniquely in the form

$$\mathbf{F} = \mathbf{R}\mathbf{U} = \mathbf{V}\mathbf{R}, \tag{2.6}$$

where $\mathbf{R}$ is a proper orthogonal tensor, so that

$$\mathbf{R}\mathbf{R}^{\text{T}} = \mathbf{R}^{\text{T}}\mathbf{R} = \mathbf{I}, \tag{2.7}$$

where $\mathbf{I}$ is the identity tensor. The tensors $\mathbf{U}$ and $\mathbf{V}$ are positive definite and symmetric, the so-called right and left stretch tensors, respectively. The eigenvalues of $\mathbf{U}$ are the (strictly positive) principal stretches of the deformation, denoted λ_i, $i = 1,2,3$. Please note that λ_i are also the eigenvalues of $\mathbf{V}$. Then by using (2.7) we can easily get

$$J = \det \mathbf{F} = \det \mathbf{U} = \det \mathbf{V}, \tag{2.8}$$

In 1839, George Green [18] introduced a deformation tensor called the right Cauchy-Green deformation tensor or Green's deformation tensor, which is defined as

$$\mathbf{C} = \mathbf{F}^{\mathrm{T}}\mathbf{F} = \mathbf{U}^2. \tag{2.9}$$

Physically, the tensor $\mathbf{C}$ gives us a measure of local change in length of an line element due to deformation.

It is also useful to note that the Nanson's formula is given by

$$\mathbf{n}\mathrm{d}a = J\mathbf{F}^{-\mathrm{T}}\mathbf{N}\mathrm{d}A, \tag{2.10}$$

where dA is the area element of material surface in $\mathfrak{B}_r$ and da is the corresponding area element in $\mathfrak{B}_t$; See Fig.2.1. $\mathbf{n}$ and $\mathbf{N}$ are the unit outward normals in the current and reference configurations, respectively. The connection (2.10) can be used to map from areas in the current configuration to the corresponding areas in the reference configuration and vice versa.

2.2 Stress theory and equilibrium

Let $\mathbf{t}$ denote surface (contact) force, per unit deformed area, which depend continuously on $\mathbf{x}$ and $\mathbf{n}$.

Theorem 2.2.1 *Cauchy's theorem: if* $\mathbf{t}(\mathbf{x}, \mathbf{n})$ *is continuous in* $\mathbf{x}$*, then there exists a second-order tensor field* $\boldsymbol{\sigma}$ *such that*

$$\mathbf{t}(\mathbf{x}, \mathbf{n}) = \boldsymbol{\sigma}(\mathbf{x})\mathbf{n}, \tag{2.11}$$

where the tensor $\boldsymbol{\sigma}$ *is also called the Cauchy stress tensor and is independent of* $\mathbf{n}$*.*

The Cauchy stress tensor $\boldsymbol{\sigma}$ is symmetric, i.e. $\boldsymbol{\sigma}^T = \boldsymbol{\sigma}$, and satisfies the Eulerian form of the equilibrium equation, namely

$$\mathrm{div}\,\boldsymbol{\sigma} + \rho\mathbf{b} = \rho\mathbf{a}, \tag{2.12}$$

where ρ is the mass density of the material of the body in current configuration $\mathfrak{B}_t$ and $\mathbf{b}$ is the body forces, measured per unit volume. $\mathbf{a}$ is the acceleration.

We can write the surface force on an area element $\mathbf{n}\mathrm{d}a$ in the current configuration as following by using (2.10) and Cauchy theorem (2.11)

$$\mathbf{t}\mathrm{d}a = \boldsymbol{\sigma}\mathbf{n}\mathrm{d}a = J\boldsymbol{\sigma}\mathbf{F}^{-\mathrm{T}}\mathbf{N}\mathrm{d}A = \mathbf{S}^{\mathrm{T}}\mathbf{N}\mathrm{d}A, \tag{2.13}$$

where the relation of nominal stress tensor $\mathbf{S}$ and Cauchy stress tensor $\boldsymbol{\sigma}$ is given by

$$\mathbf{S} = J\mathbf{F}^{-1}\boldsymbol{\sigma}. \tag{2.14}$$

The corresponding nominal stress tensor $\mathbf{S}$, also referred to as the engineering stress, which, in general, is not symmetric, satisfies

$$\mathbf{FS} = \mathbf{S}^{\mathrm{T}}\mathbf{F}^{\mathrm{T}}. \tag{2.15}$$

Please note that $\mathbf{S}^{\mathrm{T}}$ is the first Piola-Kirchhoff stress tensor.

The Lagrangian alternative to the Eulerian equilibrium equation (2.12) is

$$\operatorname{Div}\mathbf{S} + \rho_r\mathbf{b} = \rho_r\mathbf{a}, \tag{2.16}$$

where the Div is the divergence operator with respect to $\mathbf{X}$ and the mass density ρ_r is related to ρ by the mass conservation equation

$$J = \rho_r/\rho. \tag{2.17}$$

Then, in the static case, if there are no body forces the local equilibrium equation for the body has the (Lagrangian) form

$$\operatorname{Div}\mathbf{S} = \mathbf{0}, \tag{2.18}$$

or, in terms of Cauchy stress,

$$\operatorname{div}\boldsymbol{\sigma} = \mathbf{0}. \tag{2.19}$$

2.3   Constitutive law for a Cauchy elastic material

In solid mechanics, a constitutive equation approximates the actual response of a material to external forces. To be more precise it connects the stresses to strains or stretches.

A simple elastic material is one for which the stress at each material point is dependent solely on the current state of deformation with respect to an arbitrary reference configuration. However, the work done by the stress does in general depend on the path of deformation and the stress cannot be derived from a scalar potential function.

Neglecting the effect of temperature the constitutive equation for a homogeneous elastic material can be written as

$$\boldsymbol{\sigma} = \mathbf{g}(\mathbf{F}), \tag{2.20}$$

where $\mathbf{g}$ is called response function of the material relative to $\mathfrak{B}_r$, which is a symmetric tensor-valued function. We can see that the Cauchy stress $\boldsymbol{\sigma}$ at an arbitrary material point $\mathbf{X}$ is determined only by the deformation gradient $\mathbf{F}$ at this point and doesn't depend on the history of deformation.

The principle of objectivity requires that material properties should be independent of superposed rigid-body motions. This means the constitutive law $\mathbf{g}$ must satisfy

$$\mathbf{g}(\mathbf{QF}) = \mathbf{Qg}(\mathbf{F})\mathbf{Q}^{\mathrm{T}}, \tag{2.21}$$

for each $\mathbf{F}$ and any rotation $\mathbf{Q}$, which is a proper orthogonal second-tensor.

If for all proper orthogonal second-order tensors $\mathbf{Q}$, we have

$$\mathbf{g}(\mathbf{FQ}) = \mathbf{g}(\mathbf{F}), \tag{2.22}$$

then the material is said to be isotropic relative to $\mathfrak{B}_r$. In essence, this means the material properties have no preferred direction.

In equation (2.22), with $\mathbf{Q}$ replaced by $\mathbf{R}^{\mathrm{T}}$ and use of polar composition (2.6), we get

$$\boldsymbol{\sigma} = \mathbf{g}(\mathbf{F}) = \mathbf{g}(\mathbf{VRR}^{\mathrm{T}}) = \mathbf{g}(\mathbf{V}). \tag{2.23}$$

Using material objectivity (2.21) combined with the definition of isotropy (2.22) and (2.23), we obtain

$$\mathbf{g}(\mathbf{QFP}^{\mathrm{T}}) = \mathbf{Qg}(\mathbf{FP}^{\mathrm{T}})\mathbf{Q}^{\mathrm{T}} = \mathbf{Qg}(\mathbf{F})\mathbf{Q}^{\mathrm{T}} = \mathbf{Qg}(\mathbf{V})\mathbf{Q}^{\mathrm{T}}, \tag{2.24}$$

then choose $\mathbf{P} = \mathbf{QR}$, and we have

$$\mathbf{g}(\mathbf{QVQ}^{\mathrm{T}}) = \mathbf{Qg}(\mathbf{V})\mathbf{Q}^{\mathrm{T}}, \tag{2.25}$$

which then shows that $\mathbf{g}$ is an isotropic tensor function of $\mathbf{V}$. It can be shown that the Cauchy stress $\boldsymbol{\sigma}$ may be written in the form

$$\boldsymbol{\sigma} = \sum_{i=1}^{3} \sigma_i \mathbf{v}^{(i)} \otimes \mathbf{v}^{(i)}, \tag{2.26}$$

where

$$\sigma_i = \phi_0 + \phi_1 \lambda_i + \phi_2 \lambda_i^2 \quad i = 1, 2, 3. \tag{2.27}$$

$\phi_i = \phi_i(I_1, I_2, I_3)$ and the invariants are defined by

$$I_1 = \mathrm{tr}(\mathbf{C}), \quad I_2 = \frac{1}{2}[I_1^2 - \mathrm{tr}(\mathbf{C}^2)], \quad I_3 = \det \mathbf{C}. \tag{2.28}$$

2.4 Green elastic material

A Green elastic or hyperelastic material is an ideal special case of a Cauchy elastic material for which a strain-energy function exists. The observed material behaviour of rubber, filled elastomers and biological tissues are often described by the hyperelastic idealization. The constitutive relation of such a material can be defined as isotropic, incompressible, non-linearly elastic and generally independent of strain rate.

The strain-energy function $W(\mathbf{F})$ is given by

$$\frac{\partial}{\partial t} W(\mathbf{F}) = J tr(\boldsymbol{\sigma}\mathbf{L}), \tag{2.29}$$

where the velocity gradient tensor $\mathbf{L}$, is defined as

$$\mathbf{L} = \operatorname{grad}\mathbf{v}, \tag{2.30}$$

where $\mathbf{v}$ is the velocity vector. Physically, $W(\mathbf{F})$ is a measure of the work per unit reference volume done by stress as a result of deformation and is independent of the path of deformation.

We also have

$$\frac{\partial}{\partial t} W(\mathbf{F}) = \operatorname{tr}\left(\frac{\partial W}{\partial \mathbf{F}} \dot{\mathbf{F}} \right), \tag{2.31}$$

combined with $\dot{\mathbf{F}} = \mathbf{L}\mathbf{F}$, we can get

$$\frac{\partial}{\partial t} W(\mathbf{F}) = \operatorname{tr}\left(\frac{\partial W}{\partial \mathbf{F}} \mathbf{L}\mathbf{F} \right) = \operatorname{tr}\left(\mathbf{F}\frac{\partial W}{\partial \mathbf{F}} \mathbf{L} \right). \tag{2.32}$$

Comparison of this with (2.29) shows that stress tensor $\boldsymbol{\sigma}$ can be written in terms of $W(\mathbf{F})$ as

$$\boldsymbol{\sigma} = J^{-1}\mathbf{F}\frac{\partial W}{\partial \mathbf{F}}, \tag{2.33}$$

or in component form (Cartesian coordinates),

$$\sigma_{ij} = J^{-1}F_{ik}\frac{\partial W}{\partial F_{jk}}. \tag{2.34}$$

Note that the components of $\partial W/\partial \mathbf{F}$ are defined by the convention

$$\left(\frac{\partial W}{\partial \mathbf{F}} \right)_{ij} = \frac{\partial W}{\partial F_{ji}}. \tag{2.35}$$

Using the connection (2.14) between the nominal stress $\mathbf{S}$ and the Cauchy stress tensor $\boldsymbol{\sigma}$, it follows that

$$\mathbf{S} = \frac{\partial W}{\partial \mathbf{F}}, \tag{2.36}$$

and the component form is

$$S_{ij} = \frac{\partial W}{\partial F_{ji}}. \tag{2.37}$$

Definition 2.4.1 *Since W is a scalar function objectivity requires that it is unaffected by a superimposed rigid-body rotation after deformation, i.e.*

$$W(\mathbf{QF}) = W(\mathbf{F}) \tag{2.38}$$

for all rotations $\mathbf{Q}$ and for each deformation gradient $\mathbf{F}$.

Definition 2.4.2 *For a hyperelastic material which is isotopic relative to $\mathfrak{B}_r$, W is unaffected by rotations in $\mathfrak{B}_r$ (prior to deformation), such that*

$$W(\mathbf{FP}^{\mathrm{T}}) = W(\mathbf{F}) \tag{2.39}$$

for all rotations $\mathbf{P}$.

Using the definitions of objectivity and isotropy of $W(\mathbf{F})$, we could deduce

$$W(\mathbf{QVQ}^{\mathrm{T}}) = W(\mathbf{V}), \tag{2.40}$$

for all rotations $\mathbf{Q}$. This means that W is an isotropic scalar function of $\mathbf{V}$. Thus, the strain energy function W has all the properties associated with the isotropic scalar function, i.e. it is expressible as a function of the principal invariants I_1, I_2, I_3 or equivalently, as a symmetric function of the principal stretches $\lambda_1, \lambda_2, \lambda_3$. So, we have

$$W(\lambda_1, \lambda_2, \lambda_3) = W(\lambda_1, \lambda_3, \lambda_2) = W(\lambda_3, \lambda_1, \lambda_2). \tag{2.41}$$

2.4.1 Stress-deformation relations in terms of invariants

We regard W as a function of the invariants I_1, I_2, I_3, defined in equation (2.28), i.e. $W(I_1, I_2, I_3)$. Then, we could express nominal stress $\mathbf{S}$ as

$$\mathbf{S} = \sum_{i=1}^{3} \frac{\partial W}{\partial I_i} \frac{\partial I_i}{\partial \mathbf{F}}. \tag{2.42}$$

Using the connection of (2.14) between the nominal stress $\mathbf{S}$ and the Cauchy stress tensor $\boldsymbol{\sigma}$, we could easily get the corresponding Cauchy stress

$$\boldsymbol{\sigma} = \sum_{i=1}^{3} J^{-1} \frac{\partial W}{\partial I_i} \mathbf{F} \frac{\partial I_i}{\partial \mathbf{F}}. \tag{2.43}$$

where the derivatives are

$$\frac{\partial I_1}{\partial \mathbf{F}} = 2\mathbf{F}^{\mathrm{T}}, \quad \frac{\partial I_2}{\partial \mathbf{F}} = 2I_1 \mathbf{F}^{\mathrm{T}} - 2\mathbf{F}^{\mathrm{T}} \mathbf{F} \mathbf{F}^{\mathrm{T}}, \quad \frac{\partial I_3}{\partial \mathbf{F}} = 2I_3 \mathbf{F}^{-1}. \tag{2.44}$$

2.5 Internal constraints

To simplify the constitutive response models and also represent a good first approximation to the actual material behaviour, some form of local constraints are used, such as incompressibility or inextensibility. In mathematical theory, the question is how the constraints influence the evaluation of the stress tensor.

Suppose the deformation is constrained by the single scalar function

$$C(\mathbf{F}) = 0. \tag{2.45}$$

Differentiation of (2.45) with respect to time gives

$$\dot{C} \equiv \mathrm{tr}\left(\frac{\partial C}{\partial \mathbf{F}}\dot{\mathbf{F}}\right) = 0. \tag{2.46}$$

Compared with the stress power defined by (2.31), we could accommodate the constraint in the stress-deformation relation by adding an arbitrary scalar multiple of $C(\mathbf{F})$, without affecting the stress power i.e.

$$W(\mathbf{F}) + qC(\mathbf{F}), \tag{2.47}$$

where the hydrostatic pressure q functions is a Lagrange multiplier, in general, q is independent of $\mathbf{F}$ and dependent on $\mathbf{X}$.

The Cauchy stress tensor $\boldsymbol{\sigma}$ and nominal stress tensor $\mathbf{S}$ defined by (2.33) and (2.36) respectively are modified to

$$J\boldsymbol{\sigma} = \mathbf{F}\frac{\partial W}{\partial \mathbf{F}} + q\mathbf{F}\frac{\partial C}{\partial \mathbf{F}}, \tag{2.48}$$

and

$$\mathbf{S} = \frac{\partial W}{\partial \mathbf{F}} + q\frac{\partial C}{\partial \mathbf{F}}. \tag{2.49}$$

For a material constrained by incompressibility, we have

$$C(\mathbf{F}) = J - 1 = \lambda_1\lambda_2\lambda_3 - 1 = 0. \tag{2.50}$$

To ensure the incompressibility of an elastic material, we can replace strain energy function $W(\mathbf{F})$ by

$$W(\mathbf{F}) - p(\det \mathbf{F} - 1). \tag{2.51}$$

Thus, the nominal stress $\mathbf{S}$ and Cauchy stress $\boldsymbol{\sigma}$ are given by

$$\boldsymbol{\sigma} = \mathbf{F}\frac{\partial W}{\partial \mathbf{F}} - p\mathbf{I}, \tag{2.52}$$

and

$$\mathbf{S} = \frac{\partial W}{\partial \mathbf{F}} - p\mathbf{F}^{-1}. \tag{2.53}$$

2.6 Example strain-energy functions for isotropic elastic material

The neo-Hookean material model is given by

$$W(\lambda_1, \lambda_2, \lambda_3) = \frac{1}{2}\mu(\lambda_1^2 + \lambda_2^2 + \lambda_3^2 - 3), \tag{2.54}$$

where $\mu(> 0)$ is a material constant referred to as the shear modulus of the material. This is an extension of Hooke's law for the case of large deformations and can be applied to plastics and rubber-like substances. However, the neo-Hookean material model usually provides sufficient accuracy for materials under moderate straining up to 30-70%.

The Mooney-Rivlin material model, a generalization of the neo-Hookean model, is defined by

$$W(\lambda_1, \lambda_2, \lambda_3) = \frac{1}{2}\mu_1(\lambda_1^2 + \lambda_2^2 + \lambda_3^2 - 3) - \frac{1}{2}\mu_2(\lambda_1^2\lambda_2^2 + \lambda_2^2\lambda_3^2 + \lambda_3^2\lambda_1^2 - 3), \tag{2.55}$$

where $\mu_1(\geq 0)$ and $\mu_1(\leq 0)$ are material constants such that $\mu_1 - \mu_2 = \mu(> 0)$.

For complex materials such as rubbers, polymers, and biological tissue subject to even larger deformation, more sophisticated models are necessary. The Ogden material model, which was developed by Ray W. Ogden in 1972, like other hyperelastic material models, assumes that the material behaviour can be described by a strain energy density function, from which the stress-deformation relationships can be derived.

The Ogden material model is given by

$$W(\lambda_1, \lambda_2, \lambda_3) = \sum_{n=1}^{N} \frac{\mu_n}{\alpha_n}(\lambda_1^{\alpha_n} + \lambda_2^{\alpha_n} + \lambda_3^{\alpha_n} - 3) \tag{2.56}$$

where μ_n and α_n are material constants and satisfy the constraint as follows

$$\sum_{n=1}^{N} \mu_n\alpha_n = 2\mu, \quad n = 1, 2, 3, ..., N, \tag{2.57}$$

where N is a positive number. Note that choosing appropriate material constants μ_n, α_n and N, the Ogden model can be reduced to Mooney-Rivlin or neo-Hookean material model.

For more details of strain-energy functions in terms of principle stretches we refer to Ogden [57], [59].

2.7 Incremental deformations

We now consider a deformation relative to a given reference configuration $\mathfrak{B}_r$, defined by

$$\mathbf{x} = \boldsymbol{\chi}(\mathbf{X}), \tag{2.58}$$

then superimpose an infinitesimal deformation on the known deformation $\boldsymbol{\chi}(\mathbf{X})$, such that

$$\mathbf{x}' = \boldsymbol{\chi}'(\mathbf{X}). \tag{2.59}$$

The infinitesimal displacement of the body due to this change is denoted by

$$\delta\mathbf{x} = \mathbf{x}' - \mathbf{x}. \tag{2.60}$$

Here we assume the displacement $\delta\mathbf{x}$ is small enough so that the terms of order $|\delta\mathbf{x}|^2$ and higher order can be neglected in comparison with those of order $|\delta\mathbf{x}|$. $\delta\mathbf{x}$ is referred to as an incremental deformation from the configuration described by $\boldsymbol{\chi}(\mathbf{X})$.

The corresponding change of deformation gradient due to the incremental displacement $\delta\mathbf{x}$ is then given by

$$\mathrm{Grad}\,\delta\mathbf{x} = \delta\mathrm{Grad}\,\mathbf{x} = \delta\mathbf{F}. \tag{2.61}$$

Using the definition of the differentiation of a scalar function of a tensor, described in Section 4.2.8 in the book by Ogden [60], and the Taylor series, we obtain the change of a scalar function as

$$\delta\phi(\mathbf{F}) = \mathrm{tr}\left(\frac{\partial\phi}{\partial\mathbf{F}}\delta\mathbf{F}\right) + \frac{1}{2}\mathrm{tr}\left(\left(\frac{\partial^2\phi}{\partial\mathbf{F}^2}\delta\mathbf{F}\right)\delta\mathbf{F}\right) + \text{higher orders.} \tag{2.62}$$

In terms of Cartesian components the first term in equation (2.62) is defined by

$$\mathrm{tr}\left(\frac{\partial\phi}{\partial\mathbf{F}}\delta\mathbf{F}\right) = \left(\frac{\partial\phi}{\partial F_{ji}}\right)\delta F_{ji}, \tag{2.63}$$

and the second term in component form is defined by

$$\frac{1}{2}\mathrm{tr}\left(\left(\frac{\partial^2\phi}{\partial\mathbf{F}^2}\delta\mathbf{F}\right)\delta\mathbf{F}\right) = \frac{1}{2}\frac{\partial^2\phi}{\partial F_{ji}\partial F_{lk}}\delta F_{lk}\delta F_{ji}. \tag{2.64}$$

Let $\phi = J$ and neglect the terms of second and higher order in the definition of (2.62), then δJ, the change in the determinant of deformation gradient can be written as

$$\delta J = J \mathrm{tr}(\mathbf{F}^{-1}\delta\mathbf{F}) \tag{2.65}$$

The increment of a tensor function $\mathbf{G}$ can be treated in a similar manner, so that

$$\delta\mathbf{G} = \frac{\partial\mathbf{G}}{\partial\mathbf{F}}\delta\mathbf{F} + \frac{1}{2}\left(\frac{\partial^2\mathbf{G}}{\partial\mathbf{F}^2}\delta\mathbf{F}\right)\delta\mathbf{F} + \text{higher orders}, \tag{2.66}$$

with Cartesian components

$$\left(\frac{\partial\mathbf{G}}{\partial\mathbf{F}}\delta\mathbf{F}\right)_{ij} = \frac{\partial G_{ij}}{\partial F_{kl}}\delta F_{kl}, \tag{2.67}$$

and

$$\left(\left(\frac{\partial^2\mathbf{G}}{\partial\mathbf{F}^2}\delta\mathbf{F}\right)\delta\mathbf{F}\right)_{ij} = \frac{\partial^2 G_{ij}}{\partial F_{kl}\partial F_{mn}}\delta F_{mn}\delta F_{kl}. \tag{2.68}$$

Then the linear approximation of the nominal stress increment may be written in accordance with (2.66)

$$\delta\mathbf{S} = \boldsymbol{\mathcal{A}}\delta\mathbf{F} \tag{2.69}$$

where the notation $\boldsymbol{\mathcal{A}}$, referred to as the tensor of first-order elastic moduli associated with the conjugate pair $(\mathbf{S}, \mathbf{F})$, is defined by

$$\boldsymbol{\mathcal{A}} = \frac{\partial\mathbf{S}}{\partial\mathbf{F}}, \tag{2.70}$$

which is also called the tensor of fixed-reference moduli.

If we take the reference configuration to coincide with the current configuration $\mathfrak{B}_t$, then the increment of the deformation gradient relative to current configuration takes the form

$$\delta\mathbf{F}_0 = \delta\mathbf{F}\mathbf{F}^{-1}, \tag{2.71}$$

where the subscript zero indicates a quantity evaluated in $\mathfrak{B}_t$.

We also have the corresponding connection

$$\delta\mathbf{S}_0 = J^{-1}\mathbf{F}\delta\mathbf{S}, \tag{2.72}$$

Then the resulting elastic moduli are referred to as the instantaneous moduli and the relation between instantaneous moduli and fixed-reference moduli is given by (for details, see [60])

$$\mathcal{A}_{0ijkl} = J^{-1}F_{i\alpha}F_{k\beta}\mathcal{A}_{\alpha j\beta l}. \tag{2.73}$$

Please note that we also introduce the alternative notation $\dot{\mathbf{x}} = \delta\mathbf{x} = \boldsymbol{\eta}, \dot{\mathbf{F}} = \delta\mathbf{F}, \dot{\mathbf{S}} = \delta\mathbf{S}$ and the instantaneous moduli $\boldsymbol{\mathcal{A}}_0 = \boldsymbol{\mathcal{B}}$ in Chapter 4.

Chapter 3

Finite element method, libmesh library

3.1 Finite element nonlinear analysis in solid mechanics

3.1.1 Introduction

The finite element method, which originated from the need for finding approximate solutions to complicated structural analysis and elasticity problems in civil and aeronautical engineering, is now an important and indispensable tool in scientific research, engineering analysis and design, such as in the thermal, electromagnetic, solid, fluid, and structural working environments.

An alternative way of solving partial differential equations is the finite difference method. Compared to the finite difference method, the most attractive feature of the finite element method is its ability to handle complicated geometries with relative ease. While finite difference methods can be very easy to implement, in general, the accuracy of a finite element method approximation is often more precise than in the corresponding finite difference method.

To alleviate difficulties in solving problems with localized features that are not efficiently resolved by mesh refinement, the extended finite element method, also known as the generalized finite element method was developed in 1999 by Belytschko and collaborators. This method has been used to model the propagation of various discontinuities, such as cracks and material interfaces.

Over the past 20 years, meshfree methods have been developed to facilitate simulations

in problems where the ability to handle discontinuities and singularities, large deformations, advanced materials is needed. For example, the melting of a solid or the freezing process can be simulated using meshfree methods.

3.1.2   Procedure for finite element solution with libmesh

Discussions on the finite element method in detail are obviously beyond the scope of this work. However, we will summarize the particular techniques and the processes related to the finite element analysis in Chapter 5.

For discretization of the differential equations, the weighted residual-Galerkin method has been used. This method is frequently adopted in the finite element literature since it usually (but by no means always) leads to symmetric matrices [80]. In essence the original shape functions are used as weighting functions for the approximations used in the integral formulations (see Appendix 1).

The displacement-based finite element procedures are not sufficiently effective for the analysis of incompressible materials, and mixed finite element models have therefore been adopted to obtain good solution accuracy [8], as illustrated in Fig. 3.1. This figure shows that, for a 6-node triangle element, the displacements are interpolated using the six nodes and the pressure, which is a Lagrange multiplier coming from the incompressibility constraint, see equation (2.5), is interpolated by using only three corner nodes. On the other hand, for 9-node quadrilateral elements, the displacements are interpolated using nine nodes and the pressure using 4 corner nodes only. Mathematically, the linear and bilinear pressure interpolations are used respectively for the above two cases, i.e.

$$p = p_0 + p_1 x + p_2 y,$$
$$p = p_0 + p_1 x + p_2 y + p_3 xy. \tag{3.1}$$

In general, once a mathematical model has been developed, the numerical finite element procedure can be followed to solve the governing equations approximately. In the following we summarize the implementation of these procedures with an object-oriented parallel finite element library, which will be covered in the next section. The procedure is depicted in Fig. 3.2. Discretization of the governing equations leads to expressions of the element stiffness matrices $\mathbf{K}^e$. We could obtain the modified element stiffness matrices $\widehat{\mathbf{K}}^\mathbf{e}$ using boundary conditions. Instead of forming all elements first and then assembling them, we will construct elements one at a time in a loop, and immediately merge them into

(a)   (b)
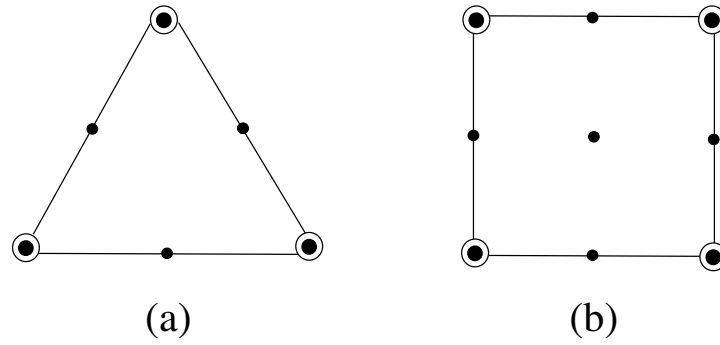
●   Node with displacement variables

⊙   Node with displacement and pressure variables

Figure 3.1: Mixed elements: (a) 6-node Triangle (b) 9-node Quadrilateral.
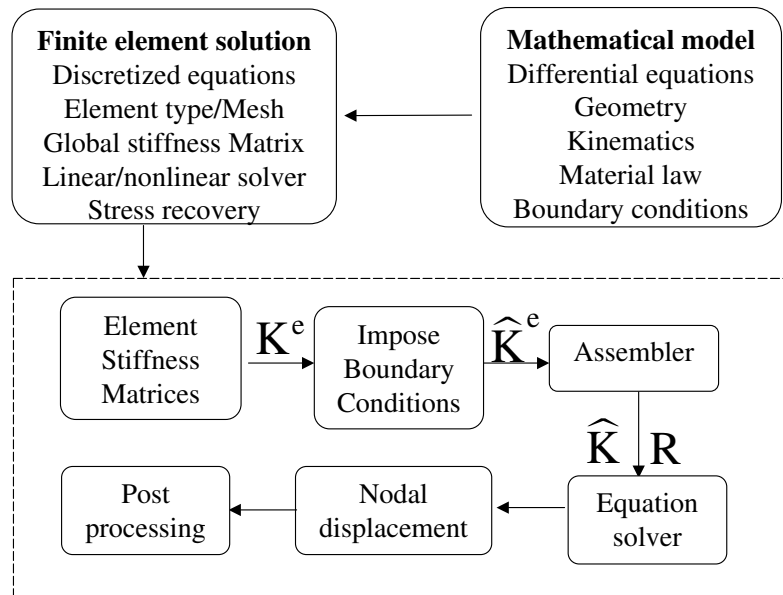
Figure 3.2: Procedures in a Finite element program.

the Global matrix $\widehat{\mathbf{K}}$. The residual vector $\mathbf{R}$ can be obtained based on $\widehat{\mathbf{K}}$. Then, the linear/nonlinear solver can be called to solve the final algebra equations. Once we get the values of the displacements and the pressure, post processing can be carried out to obtain the stresses or stretches. We could use libmesh to assemble the system and call the equation solvers to find the approximate solution. However, since libmesh is not a black box tool and still underdeveloped now, we have to create our own mesh files in 2D problems or use Tetgen (an open-source tetrahedral mesh generator) to mesh the tube in

our 3D problem. Also, we have to write code for the purpose of post processing.

3.1.3   Stress recovery

It is very important to evaluate the stresses at each node for all the elements in engineering application. A quite straightforward approach is to evaluate the stresses at the nodes of a given element by substituting the natural coordinates of the nodes to the shape functions then using the connection between stress and displacements. Another approach is to evaluate the stresses at Gauss integration points and then extrapolate to the element nodes [22]. The latter approach provides more accurate stress values for quadrilateral elements, since the best accuracy for gradients and stresses is obtained at the Gauss points. We will adopt the second approach for the calculation of stresses in Chapter 5. Other variables such as the principal stresses/stretches are also evaluated in a similar way; see details in Chapter 5. The detailed explanation of this method is given as below. However, for triangle elements both of the above approaches give similar results. Note that this discussion is mainly based on the course materials from the Department of Aerospace Engineering Sciences, University of Colorado at Boulder; for details, see the website: http://www.colorado.edu/engineering/cas/courses.d/IFEM.d/.

Taking a 4-node quadrilateral element for example, the four Gauss points, denoted as $1', 2', 3', 4'$ are composed of the "Gauss element", as illustrated in Fig.3.3. The natural coordinates of both the nodes of the quadrilateral element and the nodes of Gauss element are listed in Table 3.1. The "Gauss element", denoted by (e'), is also a 4-node quadrilateral, with its coordinates denoted by ξ' and η'. The connections between two sets of coordinates are

$$\xi = \xi'/\sqrt{3}, \quad \eta = \eta'/\sqrt{3}. \tag{3.2}$$

An arbitrary scalar quantity u can be approximated by

$$u(\xi', \eta') = \sum_{i=1}^{4} N_i^{(e')}(\xi', \eta')u_i', \tag{3.3}$$

where $N_i^{(e')}, i = 1, 2, 3, 4$ are the shape functions, defined by

$$N_1^{(e')} = \frac{1}{4}(1 - \xi')(1 - \eta'),$$
$$N_2^{(e')} = \frac{1}{4}(1 + \xi')(1 - \eta'),$$
$$N_3^{(e')} = \frac{1}{4}(1 + \xi')(1 + \eta'),$$
$$N_4^{(e')} = \frac{1}{4}(1 - \xi')(1 + \eta'). \tag{3.4}$$

When the stresses at Gauss element points are evaluated, the extrapolation procedure can be done. For example, to extrapolate u to node 1, we replace its coordinates $(\xi', \eta') = (-\sqrt{3}, -\sqrt{3})$ into equation (3.3).

Table 3.1: Natural coordinates of Quadrilateral nodes.

Corner nodes	ξ	η	ξ'	η'	Gauss nodes	ξ	η	ξ'	η'
1	-1	-1	$-\sqrt{3}$	$-\sqrt{3}$	$1'$	$-1/\sqrt{3}$	$-1/\sqrt{3}$	-1	-1
2	$+1$	-1	$+\sqrt{3}$	$-\sqrt{3}$	$2'$	$+1/\sqrt{3}$	$-1/\sqrt{3}$	$+1$	-1
3	$+1$	$+1$	$+\sqrt{3}$	$+\sqrt{3}$	$3'$	$+1/\sqrt{3}$	$+1/\sqrt{3}$	$+1$	$+1$
4	-1	$+1$	$-\sqrt{3}$	$+\sqrt{3}$	$4'$	$-1/\sqrt{3}$	$+1/\sqrt{3}$	-1	$+1$
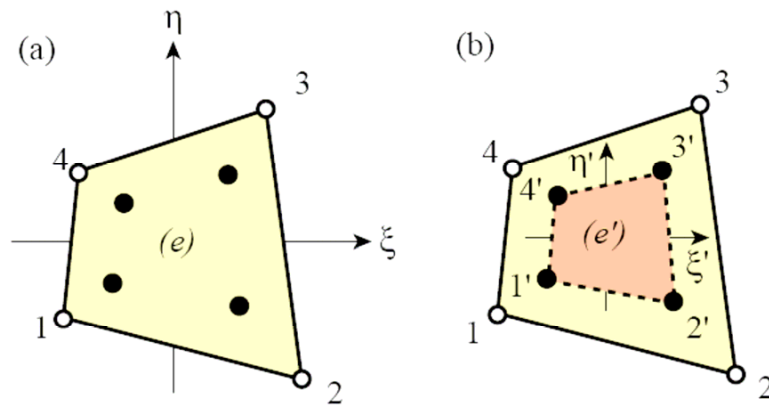
Figure 3.3: (a) 4-node quadrilateral element (e); (b) Gauss element (e')

Figure 3.4 shows Gauss elements for 8-node and 9-node quadrilaterals and a 6-node triangle. Extrapolation in these higher order elements can be evaluated in a similar way easily. However, it is a process demanding great caution for the implementation of this stress recovery technique compatibly with libmesh.

In finite element analysis, it is an assumption that the elements must be complete and compatible. The compatibility condition requires the displacements and their mth derivatives are continuous across the adjacent element for a C^m variational problem [8]. In the analysis of a plate bending problem, for example, the transverse displacement u is the only unknown variable. The transverse displacement u and its derivatives $\partial u/\partial x, \partial u/\partial y$ are continuous. This continuity condition can't guarantee the continuity of the stresses calculated at the same node of adjacent elements. This indicates some necessary process
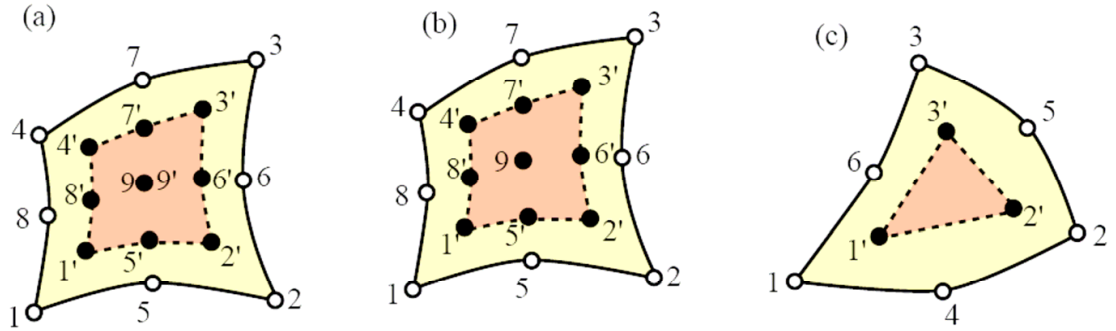
Figure 3.4: Gauss elements for high order quadrilaterals and triangles (a) 9-node element with 3×3 Gauss rule (b) 9-node element with 3×3 Gauss rule (c) 6-node element with 3-interior rule.

of stress averaging is needed to smooth and improve the accuracy of the stresses. The stress averaging might be followed in two ways in practice:

1. Unweighted averaging: assign the same weight to all elements that share a common node.

2. Weighted averaging: the weight assigned to element contributions depends on the stress component and the element geometry and possibly the element type.

For the problems in Chapter 5 the unweighted averaging is chosen to compute the averaged nodal stresses σ_{ij} as well as other nodal variables such as the principal stretches λ_i.

3.2   Libmesh library

The open-source finite element library libmesh [44] provides a software framework for parallel adaptive finite element simulations of partial differential equations using arbitrary unstructured discretization. It is also integrated with third party software packages such as (1) PETSc and LASPack for the solution of linear systems on both serial and parallel platforms, (2) METIS and ParMETIS for mesh partitioning, (3) Triangle and Tetgen for mesh generation. libmesh has been developed at The University of Texas at Austin in the CFD Lab since March 2002. The libmesh library itself is not tied to any particular application. The simulations presented in Chapter 5 were performed by the author using application codes built on top of this framework. The libmesh library is coded by the object-oriented C++ programming language. In the following section, an overview of Object-Oriented

scientific computing is presented, which is a key to gaining better understanding of the libmesh framework.

3.2.1 Object-Oriented Scientific Computing

The C++ programming language provides many useful features for simulating complex scientific computing problems [15], [16], [68], such as abstraction, encapsulation, inheritance, polymorphism. A critical feature missing in Fortran 90 is the template techniques, which allows C++ programmers to build portable, reusable code and to dramatically improve the efficiency of the evaluation of complex expressions involving user-defined data types. In recent years the performance of the C++ programming language has improved. Many high performance, object-oriented scientific softwares have been developed using C++.

There are two distinct paradigms for implementing software algorithms, namely procedure-oriented and object-oriented approaches.

The procedural approach has dominated numeric computation and scientific computing for decades. One of the most popular procedural programming language is Fortran. In this approach a sequence of algorithmic steps operates on some set of data structures to implement a given algorithm. In consequence the data storage and procedure implementation are intimately related. Suppose a standard array were used to store the individual elements of a vector, for example. If for some reason, a linked-list would be a more efficient data structure, due to dynamic insertion and removal of elements, for example, then it would require substantial changes to all codes which use such a vector.

On the other hand, object-oriented approaches provide user-defined classes which define the attributes and the behaviours of a particular data type. The class concept is a tool that can be used to create new data types. Within a given class, data and function members can be declared as either public, protected, or private in order to explicitly enforce encapsulation. A significant feature of classes is encapsulation. As a result, the actual data is separated from operations which are performed on the data. Considering the vector example again, object-oriented programming allows that the specific data structure used to store the elements of the vector can be completely encapsulated within an object and the codes which use such an object don't need to have any access to this data structure. Then, if the algorithmic implementation or data storage techniques of an object are changed for some reason, the codes using such an object need not to change. For this and many other reasons, object-oriented programming has been used widely since the mid-1990s

to build more maintainable and extensible software. The application of object-oriented techniques in scientific numerical simulations has been slow but much effort is being made to implement high performance object-oriented scientific software [3], [4], [44].

3.2.2 libmesh: Adaptive mesh refinement scheme
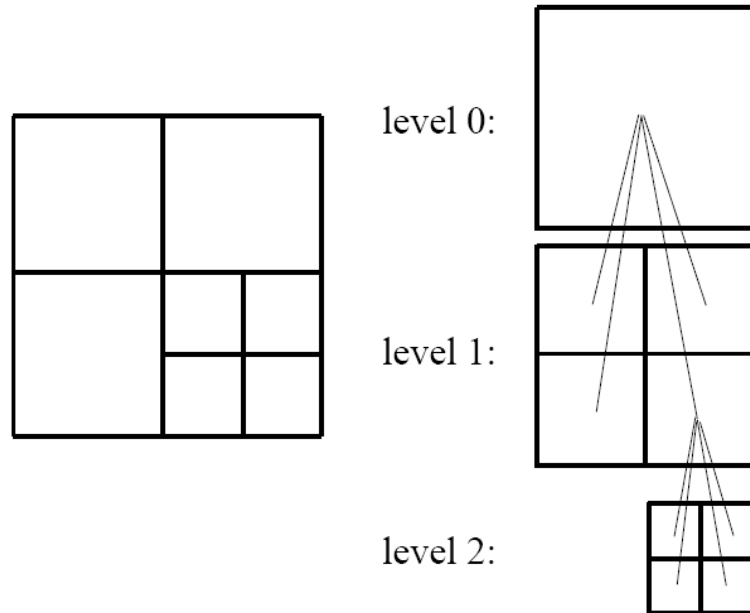
Figure 3.5: Element refinement hierarchy for a 2D quadrilateral mesh (from PhD thesis by Kirk [45]).

One of the main features of libmesh is the support for adaptive mesh refinement. In an adaptive refinement procedure, when a solution on a given mesh is obtained, the error of this solution will be estimated to get local error indicators which can be used as the criteria for selective local mesh refinement. Two main categories of procedures for the adaptive refinement of the finite element solutions are the h-refinement and p-refinement. In h-refinement the elements are changed in size, as illustrated in Fig. 3.5; some of the elements are made larger and others are smaller. By contrast, p-refinement keeps the size of the elements but increases the order of the polynomial used in their definition [19], [80]. Both of the refinement approaches are provided in the libmesh library. In a refinement process used by libmesh a new set of children elements is created from the parent elements through a linear map, which is provide by an "embedding matrix". On the other hand, in the coarsening process all the children of a given element are removed and the parent element

is re-activated. For details of the error indicators and refinement criteria, we refer to the work done by Kelly [43]. Figure 3.6 shows the solution to the nonlinear model (described in Chapter 5) for an adapted quadrilateral mesh using the *KellyErrorEstimator* class in libmesh.
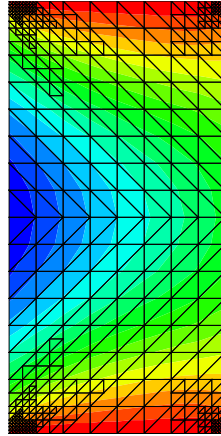
Figure 3.6: Adaptive mesh refinement on a rectangle domain.

3.2.3 Data structure of libmesh

Most of this section is based on the libmesh web page: http://libmesh.sourceforge.net/, the paper [44] and the dissertation by Kirk [45].

The `Mesh` class provides a description of a geometric entity. A mesh is composed of elements and nodes, which are stored in the mesh. These data are encapsulated by abstract classes which provide an interface for a variety of possible implementations. To access the particular subset or all the nodes and elements in the mesh, the user just needs to create a node/element iterator object. In addition, this class provides functions for implementing mesh input/output in various formats, including GMV format from Los Alamos National Labs, TetGen, Tecplot, Exodus II from Sandia National Labs, and GMSH.

The abstract base class `Elem` provides an interface for implementation of a geometric element. The derived classes, such as `Hex8` support the actual operation and calculations for a given geometric elements via virtual functions. Figure 3.7 shows a simplified inheritance diagram, in which a `Cell` is an abstract `Elem` in three-dimensions and a cell could be a tetrahedron, a pyramid, a prism, or a hexahedron. The concrete subclass `Hex8` is

an element composed of 8 nodes in three dimensions. The user can conveniently obtain the number of the nodes of all geometric element types by calling the virtual function `n_nodes()` on an `Elem` pointer. These virtual functions allow for defining a new element type by the user without affecting the external application programming interface; for example, the original code used to return the number of nodes of a given element type.
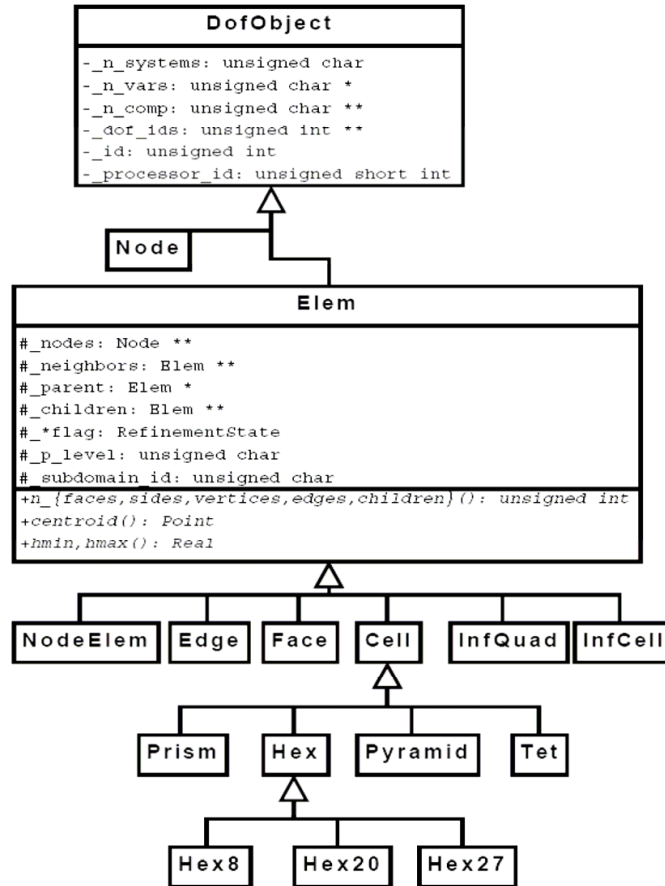
Figure 3.7: A simplified inheritance diagram for the *DofObject* class (from PhD thesis by Stogner [67]).

In a classic finite element data structure, the element connectivity is usually given in terms of the node indices, while in the libmesh library the `Elem` class stores pointers to the nodes to which the element is connected. This approach can enable the element to determine the location of its nodes with a single pointer dereference. Elements also contain pointers to their face neighbours and their parent or child elements. When at least one side of the element is on the physical boundary of the domain, it means the element has a `Null` neighbour with a `Null` pointer added into the array of the pointers to its neighbour. It is convenient to apply boundary conditions by finding all the elements with a `Null`

pointer neighbour.

The abstract `System` class contains information related to a set of differential equations that might be simulated. Several concrete systems are derived, such as `LinearImplicitSystem`, `NonlinearImplicitSystem` which will be used to solve the linear and nonlinear sets of equations in Chapters 5 and 6. Note that a system is uniquely tied to a particular mesh; in a simulation multiple meshes are used, and then multiple systems are needed.

The base class `NonlinearSolver` provides a uniform interface for nonlinear solvers in packages like PETSc. PETSc, a portable and extensible library for scientific computing, is the underlying parallel linear solver used in this work, which was developed in the Mathematics and Computer Science Division at Argonne National Laboratory [4].

Although libmesh offers all the standard geometric element types, such as triangles, quadrilaterals, tetrahedra, hexahedra, prisms and pyramids, it can't automatically generate meshes for complex geometries but is only limited to simple geometries like a rectangle, a circle and a cube. For the two dimensional problem described in more details in Chapter 5, a symmetric mesh is necessary to obtain the correct solution, since the geometry of the tube section and the boundary conditions, including pressure on lateral surface of the tube and zero-displacement end conditions, are all symmetric. We have written several mesh files (for details, see Appendix) in XDA format to store the coarse symmetric mesh data and then using uniform refinement loops to obtain the final mesh. For the three dimensional problems in Chapter 6, we use the mesh generator TetGen [31] to generate tetrahedral meshes, which then can be read into libmesh. The C++ code used to obtain the tetrahedral mesh (as illustrated in Fig. 3.8) is provided in Appendix 2.
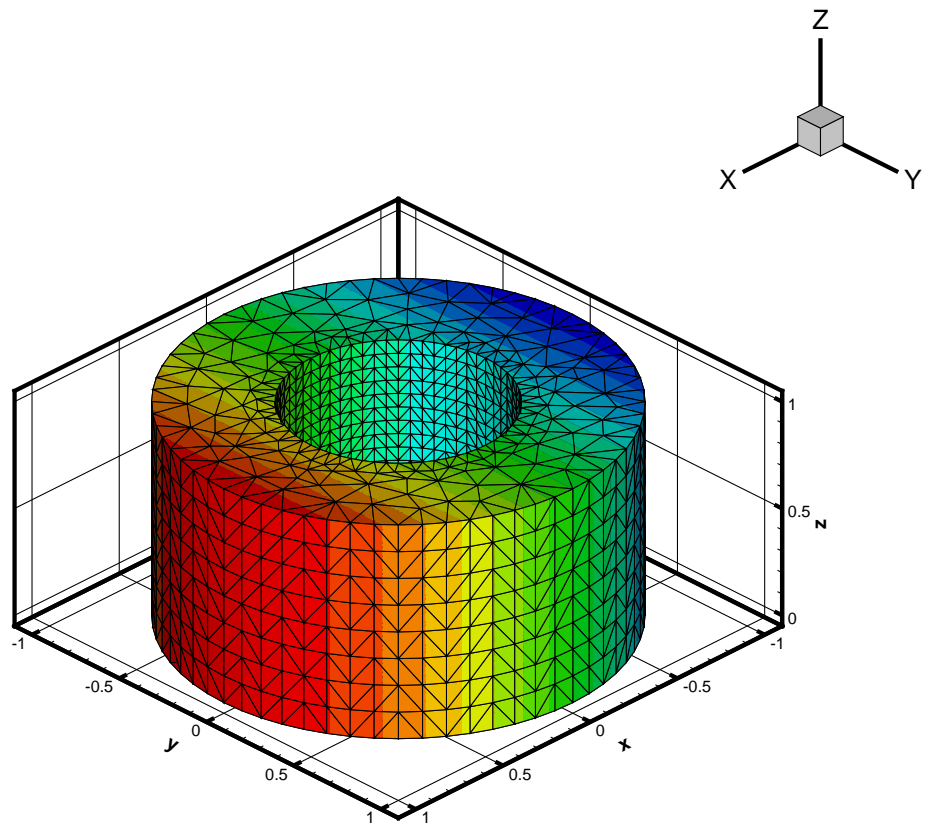
Figure 3.8: A 3D tube discretized by tetrahedral element.

Chapter 4

Bifurcation

In this chapter we restrict our attention to buckling of circular cylindrical tubes under external pressure.

In Section 1 we summarize the necessary constitutive equations that describe finite elastic deformations, while in Section 2 these are specialized to the circular cylindrical geometry of a thick-walled tube that maintains its circular cylindrical shape under axial extension and external pressure. The equations that describe a general (three-dimensional) incremental deformation superimposed on the deformed circular cylindrical tube are then given in Section 3. The three coupled partial differential equations governing the incremental displacement components are highlighted in Section 4 along with the relevant incremental boundary conditions. Based on an appropriate Ansatz for the displacement components the equations reduce to coupled ordinary differential equations, for the solution of which a numerical scheme is then described. In Section 5 the numerical method is used in respect of a specific material model in order to obtain details of the onset of bifurcation in either an axisymmetric or asymmetric mode.

4.1   The elastic constitutive law and strain-energy function

We consider the material body to be composed of an elastic material, whose properties are described in terms of a strain-energy function, which we denote by $W = W(\mathbf{F})$ per unit reference volume. Here we confine attention to incompressible materials, so that the stress-deformation relation is given by either

$$\mathbf{S} = \frac{\partial W}{\partial \mathbf{F}} - p\mathbf{F}^{-1},$$ (4.1)

where p (an arbitrary hydrostatic stress) is a Lagrange multiplier associated with the constraint (2.5), or

$$\boldsymbol{\sigma} = \mathbf{F}\frac{\partial W}{\partial \mathbf{F}} - p\mathbf{I}, \tag{4.2}$$

where $\mathbf{I}$ is the identity tensor.

Here we take the material to be isotropic, so that W depends on $\mathbf{F}$ only through the principal stretches λ_i, $i = 1, 2, 3$, and is a symmetric function of the stretches. We therefore represent W in the form $W = W(\lambda_1, \lambda_2, \lambda_3)$, and, for an incompressible material, the constraint (2.5) may be written in terms of the stretches as

$$\lambda_1 \lambda_2 \lambda_3 = 1. \tag{4.3}$$

Moreover, (4.2) can be decomposed on principal axes as

$$\sigma_i = \lambda_i \frac{\partial W}{\partial \lambda_i} - p, \quad i = 1, 2, 3 \text{ (no summation)}, \tag{4.4}$$

σ_i, $i = 1, 2, 3$, being the principal Cauchy stresses.

For subsequent convenience it is useful to regard W as a function of just two independent stretches, λ_1 and λ_2 say, and to introduce the notation $\hat{W}$ defined by

$$\hat{W}(\lambda_1, \lambda_2) = W(\lambda_1, \lambda_2, \lambda_1^{-1}\lambda_2^{-1}). \tag{4.5}$$

It then follows from (4.4) that the principal stress differences can be written

$$\sigma_1 - \sigma_3 = \lambda_1 \frac{\partial \hat{W}}{\partial \lambda_1}, \quad \sigma_2 - \sigma_3 = \lambda_2 \frac{\partial \hat{W}}{\partial \lambda_2}. \tag{4.6}$$

4.2   The circular cylindrical configuration

We now consider a thick-walled circular cylindrical tube with reference geometry described by

$$A \leq R \leq B, \quad 0 \leq \Theta \leq 2\pi, \quad 0 \leq Z \leq L, \tag{4.7}$$

where R, Θ, Z are cylindrical polar coordinates, A and B are the inner and outer radii, respectively, and L is the length of the tube. This is depicted in Fig. 4.1(a).

The initial deformed configuration of the tube, under the action of axial loading and external pressure, is assumed also to be circular cylindrical, with geometry described by

$$a \leq r \leq b, \quad 0 \leq \theta \leq 2\pi, \quad 0 \leq z \leq l, \tag{4.8}$$
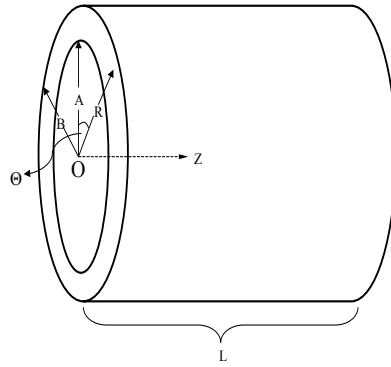
(a)
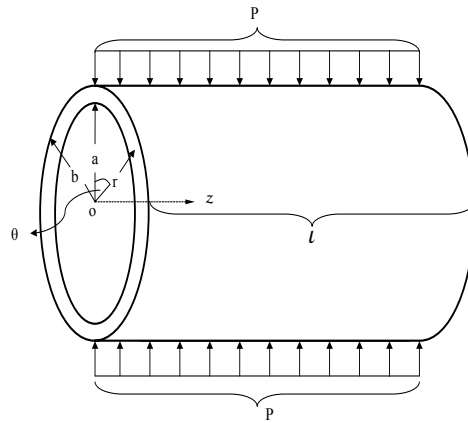
(b)

Figure 4.1: The circular cylindrical tube in its reference configuration (a) and deformed configuration when subject to axial load and external pressure (b).

where r, θ, z are cylindrical polar coordinates, a and b are the internal and external radii, respectively, and l is the length. Since the material is incompressible, the deformation is described by the equations

$$r^2 = a^2 + \lambda_z^{-1}(R^2 - A^2), \quad \theta = \Theta, \quad z = \lambda_z Z, \tag{4.9}$$

where λ_z is the axial extension ratio (or axial stretch), which is uniform.

We use $\mathbf{e}_1, \mathbf{e}_2, \mathbf{e}_3$ to denote the unit basis vectors corresponding to the coordinates θ, z, r, respectively. For the considered deformation, since the material is isotropic, these

define the principal directions of both the stretch tensor $\mathbf{U}$ and the Cauchy stress $\boldsymbol{\sigma}$. Let $\lambda_1, \lambda_2, \lambda_3$ denote the corresponding principal stretches and $\sigma_1, \sigma_2, \sigma_3$ the associated principal Cauchy stresses, which are given by (4.4). From the incompressibility constraint together with (4.9), we have

$$\lambda_2 = \lambda_z, \quad \lambda_1 = \frac{r}{R} \equiv \lambda, \quad \lambda_3 = (\lambda_1 \lambda_z)^{-1}. \tag{4.10}$$

For the symmetric configuration considered here, the only equilibrium equation not satisfied trivially is

$$r \frac{d\sigma_3}{dr} + \sigma_3 - \sigma_1 = 0, \tag{4.11}$$

and we have the associated boundary conditions

$$\sigma_3 = \begin{cases} 0 & \text{on } r = a \\ -P & \text{on } r = b. \end{cases} \tag{4.12}$$

Using $\hat{W}$, as defined in (4.5), (4.6)$_1$, and the definitions (4.10), integration of (4.11) and application of the boundary conditions (4.12) yields

$$P = -\int_a^b \lambda \hat{W}_\lambda \frac{dr}{r}. \tag{4.13}$$

On application of the connections $r = \lambda R$ and (4.9) this may be re-written with λ as the integration variable in the form

$$P = \int_{\lambda_a}^{\lambda_b} \frac{\hat{W}_\lambda}{(\lambda^2 \lambda_z - 1)} d\lambda, \tag{4.14}$$

where

$$\lambda_a = \frac{a}{A}, \quad \lambda_b = \frac{b}{B}. \tag{4.15}$$

We note here that if there is, additionally, an internal pressure, $P_i > 0$ say, then the left-hand sides of (4.13) and (4.14) are replaced by $P - P_i$. Thus, the effect of an internal pressure can be captured by taking $P < 0$ in the above formulas, this corresponding to a radial external tension on $r = b$.

4.3 Incremental equations

Detailed derivation of the incremental equations can be found in [35] for a thick-walled and [34] for a thin-walled tube (see [32] and [33] for corresponding results for spherical shells). Here we provide a summary of the main results needed for our analysis. A superposed

dot signifies an increment in the quantity concerned, and a subscript 0 indicates that the quantity to which it is attached is calculated with respect to the deformed configuration as reference configuration. First, let $\dot{\mathbf{x}}(\mathbf{X})$ denote the incremental displacement vector, and then define $\mathbf{u}(\mathbf{x})$ through $\mathbf{u}(\mathbf{x}) = \mathbf{u}(\boldsymbol{\chi}(\mathbf{X})) = \dot{\mathbf{x}}(\mathbf{X})$. Note that $\mathbf{u}$ was used earlier for the displacement in equation (2.1) in Chapter 1, which does not appear in this chapter so there is no conflict of notation. Next, introduce the notation $\boldsymbol{\eta}$ defined by

$$\boldsymbol{\eta} = \dot{\mathbf{F}}_0 \equiv \dot{\mathbf{F}}\mathbf{F}^{-1} = \operatorname{grad}\mathbf{u}. \tag{4.16}$$

The incremental form of the incompressibility condition can then be written

$$\operatorname{tr}\boldsymbol{\eta} = 0. \tag{4.17}$$

The increment of the constitutive law (4.1) has the form

$$\dot{\mathbf{S}} = \boldsymbol{\mathcal{A}}\dot{\mathbf{F}} - \dot{p}\mathbf{F}^{-1} + p\mathbf{F}^{-1}\dot{\mathbf{F}}\mathbf{F}^{-1}, \tag{4.18}$$

where $\boldsymbol{\mathcal{A}}$ is the elasticity tensor with components defined by

$$\mathcal{A}_{\alpha i\beta j} = \frac{\partial^2 W}{\partial F_{i\alpha}\partial F_{j\beta}}. \tag{4.19}$$

When the reference configuration is updated to the current configuration this becomes

$$\dot{\mathbf{S}}_0 = \boldsymbol{\mathcal{B}}\boldsymbol{\eta} + p\boldsymbol{\eta} - \dot{p}\mathbf{I}, \tag{4.20}$$

where $\mathbf{I}$ is again the identity tensor and $\boldsymbol{\mathcal{B}}$ is the 4th-order tensor of instantaneous elastic moduli, whose (Cartesian) components are related to those of $\boldsymbol{\mathcal{A}}$ by

$$\mathcal{B}_{piqj} = F_{p\alpha}F_{q\beta}\mathcal{A}_{\alpha i\beta j}. \tag{4.21}$$

For an incompressible isotropic elastic material the non-vanishing components of $\boldsymbol{\mathcal{B}}$ referred to the principal axes of $\boldsymbol{\sigma}$ can be written (see, for example, [58])

$$\mathcal{B}_{iijj} = \mathcal{B}_{jjii} = \lambda_i\lambda_j W_{ij}, \tag{4.22}$$

$$\mathcal{B}_{ijij} = \frac{\lambda_i W_i - \lambda_j W_j}{\lambda_i^2 - \lambda_j^2}\lambda_i^2, \quad \lambda_i \neq \lambda_j, \tag{4.23}$$

$$\mathcal{B}_{ijji} = \mathcal{B}_{jiij} = \mathcal{B}_{ijij} - \lambda_i W_i, \quad i \neq j, \tag{4.24}$$

where $W_i = \partial W/\partial\lambda_i$, $W_{ij} = \partial^2 W/\partial\lambda_i\partial\lambda_j$.

The incremental form of the equilibrium equation (2.18) is $\operatorname{Div}\dot{\mathbf{S}} = \mathbf{0}$ and when updated it becomes

$$\operatorname{div}\dot{\mathbf{S}}_0 = \mathbf{0}, \tag{4.25}$$

the incremental counterpart of (2.19).

For the problem to be considered in the following sections we shall be making use of the pressure boundary condition, which, referred to the original reference configuration, may be written

$$\mathbf{S}^{\mathrm{T}}\mathbf{N} = -P\mathbf{F}^{-\mathrm{T}}\mathbf{N}, \tag{4.26}$$

where $\mathbf{N}$ is the unit outward normal vector to the boundary of the body in the reference configuration and P is the pressure on the boundary per unit area of the deformed configuration. On taking the increment of (4.26) and updating to the deformed configuration we obtain

$$\dot{\mathbf{S}}_0^{\mathrm{T}}\mathbf{n} = P\boldsymbol{\eta}^{\mathrm{T}}\mathbf{n} - \dot{P}\mathbf{n}, \tag{4.27}$$

which is the form of incremental boundary condition that we shall use.

We now specialize (4.25) to circular cylindrical coordinates based of the underlying solution discussed in Section 3. The curvilinear coordinates are ordered so that $(x^1, x^2, x^3) = (\theta, z, r)$. Then, we have, in component form,

$$\dot{S}_{0ji,j} + \dot{S}_{0ji}\mathbf{e}_k \cdot \mathbf{e}_{j,k} + \dot{S}_{0kj}\mathbf{e}_i \cdot \mathbf{e}_{j,k} = 0, \quad i = 1, 2, 3, \tag{4.28}$$

with summation over indices j and k from 1 to 3, where the subscript $j\,(= 1, 2, 3)$ following a comma represents the derivatives $(\partial/r\partial\theta, \partial/\partial z, \partial/\partial r)$. The only non-zero components of $\mathbf{e}_i \cdot \mathbf{e}_{j,k}$ are

$$\mathbf{e}_1 \cdot \mathbf{e}_{3,1} = \frac{1}{r}, \quad \mathbf{e}_3 \cdot \mathbf{e}_{1,1} = -\frac{1}{r}. \tag{4.29}$$

Referred to the cylindrical polar axes the incremental displacement $\mathbf{u}$ is written in terms of its components (v, w, u) as

$$\mathbf{u} = v\mathbf{e}_1 + w\mathbf{e}_2 + u\mathbf{e}_3. \tag{4.30}$$

Then, from the definition $\boldsymbol{\eta} = \operatorname{grad}\mathbf{u}$ we obtain the component matrix of $\boldsymbol{\eta}$ referred to the axes in question as

$$[\boldsymbol{\eta}] = \begin{pmatrix} (u + v_\theta)/r & v_z & v_r \\ w_\theta/r & w_z & w_r \\ (u_\theta - v)/r & u_z & u_r \end{pmatrix}, \tag{4.31}$$

where the square brackets indicate the matrix of components of the enclosed quantity and the subscripts (r, θ, z) signify standard partial derivatives.

The incompressibility condition (4.17) can now be given explicitly as

$$\operatorname{tr}\boldsymbol{\eta} \equiv u_r + (u + v_\theta)/r + w_z = 0. \tag{4.32}$$

4.4 Asymmetric bifurcations and numerical methods

We now substitute (4.20), (4.31), (4.32) and the expressions for the components of $\mathcal{B}_{ijkl}$ into (4.28) to obtain

$$\dot{p}_\theta = (r\mathcal{B}'_{3131} + \mathcal{B}_{3131})(u_\theta + rv_r - v)/r + (\mathcal{B}_{1111} - \mathcal{B}_{1122} - \mathcal{B}_{2112})(u_\theta + v_{\theta\theta})/r$$
$$+ \mathcal{B}_{2121}rv_{zz} + \mathcal{B}_{3131}rv_{rr} + (\mathcal{B}_{1133} - \mathcal{B}_{1122} - \mathcal{B}_{2112} + \mathcal{B}_{3113})u_{r\theta}, \tag{4.33}$$

$$\dot{p}_z = (r\mathcal{B}'_{3232} + \mathcal{B}_{3232})(u_z + w_r)/r + \mathcal{B}_{1212}(w_{\theta\theta} - ru_z)/r^2 + \mathcal{B}_{3232}w_{rr}$$
$$+ (\mathcal{B}_{2222} - \mathcal{B}_{1221} - \mathcal{B}_{1122})w_{zz} + (\mathcal{B}_{2233} + \mathcal{B}_{3223} - \mathcal{B}_{1221} - \mathcal{B}_{1122})u_{rz}, \tag{4.34}$$

$$\dot{p}_r = (r\mathcal{B}'_{1133} - r\mathcal{B}'_{2233} - \mathcal{B}_{1111} + \mathcal{B}_{1122})(u + v_\theta)/r^2 + \mathcal{B}_{1313}(u_{\theta\theta} - v_\theta)/r^2 + \mathcal{B}_{3223}w_{rz}$$
$$+ (\mathcal{B}_{1331} + \mathcal{B}_{1133} - \mathcal{B}_{2233})v_{r\theta}/r + (\mathcal{B}_{3333} - \mathcal{B}_{2233})u_{rr} + \mathcal{B}_{2323}u_{zz}$$
$$+ (r\mathcal{B}'_{3333} + rp' - r\mathcal{B}'_{2233} + \mathcal{B}_{3333} - 2\mathcal{B}_{2233} + \mathcal{B}_{1122})u_r/r. \tag{4.35}$$

On the cylindrical boundaries we apply the specialization of (4.27) to the present situation, with the inner boundary free of incremental traction and the outer boundary subject to pressure P. Taking $\dot{P} = 0$ in (4.27) we then have, for $i = 1, 2, 3$,

$$\dot{S}_{03i} = \begin{cases} 0 & \text{on } r = a \\ P\eta_{3i} & \text{on } r = b. \end{cases} \tag{4.36}$$

At the ends of the tube we apply the incremental boundary conditions

$$u = v = 0, \quad \dot{S}_{022} = 0 \quad \text{on } z = 0, l. \tag{4.37}$$

This means that the ends of the tube are constrained so that no incremental rotation or radial displacement is allowed, while the axial component of traction is of dead-load type.

To solve the equations, we assume that the solution takes the form

$$\left.\begin{array}{ll} u = f(r)\cos m\theta \sin \alpha z, & v = g(r)\sin m\theta \sin \alpha z, \\ w = h(r)\cos m\theta \cos \alpha z, & \dot{p} = k(r)\cos m\theta \sin \alpha z, \end{array}\right\} \tag{4.38}$$

where $m = 0, 1, 2, 3, \ldots$ is the azimuthal mode number, $m = 0$ corresponding to an axisymmetric solution. Substitution into the incompressibility condition (4.32) then yields

$$rf'(r) + f(r) + mg(r) - \alpha rh(r) = 0. \tag{4.39}$$

Also, on inserting (4.38) into (4.33)–(4.35) and using (4.39) to eliminate $h(r)$, we obtain

three coupled equations for $f(r), g(r)$ and $k(r)$, namely

$$(r\mathcal{B}'_{3131} + \mathcal{B}_{3131} + \mathcal{B}_{1111} - \mathcal{B}_{1122} - \mathcal{B}_{2112})mf(r) + (\mathcal{B}_{1133} - \mathcal{B}_{1122} + \mathcal{B}_{3113} - \mathcal{B}_{2112})mrf'(r)$$
$$+ [r\mathcal{B}'_{3131} + \mathcal{B}_{3131} + m^2(\mathcal{B}_{1111} - \mathcal{B}_{1122} - \mathcal{B}_{2112}) + \alpha^2 r^2 \mathcal{B}_{2121}]g(r)$$
$$- (r\mathcal{B}'_{3131} + \mathcal{B}_{3131})rg'(r) - \mathcal{B}_{3131}r^2 g''(r) - mrk(r) = 0, \tag{4.40}$$

$$[r\mathcal{B}'_{3232} - \mathcal{B}_{3232} + m^2\mathcal{B}_{1212} - \alpha^2 r^2(r\mathcal{B}'_{3232} + \mathcal{B}_{3232} - \mathcal{B}_{1212} + \mathcal{B}_{1122} + \mathcal{B}_{1221} - \mathcal{B}_{2222})]f(r)$$
$$- [r\mathcal{B}'_{3232} - \mathcal{B}_{3232} - m^2\mathcal{B}_{1212} - \alpha^2 r^2(\mathcal{B}_{2222} - \mathcal{B}_{2233} - \mathcal{B}_{3223})]rf'(r)$$
$$- (r\mathcal{B}'_{3232} + 2\mathcal{B}_{3232})r^2 f''(r) - \mathcal{B}_{3232}r^3 f'''(r)$$
$$+ [r\mathcal{B}'_{3232} - \mathcal{B}_{3232} + m^2\mathcal{B}_{1212} + \alpha^2 r^2(\mathcal{B}_{2222} - \mathcal{B}_{1122} - \mathcal{B}_{1221})]mg(r)$$
$$- (r\mathcal{B}'_{3232} - \mathcal{B}_{3232})mrg'(r) - \mathcal{B}_{3232}mr^2 g''(r) + \alpha^2 r^3 k(r) = 0, \tag{4.41}$$

$$(r\mathcal{B}'_{1133} - r\mathcal{B}'_{2233} - \mathcal{B}_{1111} + \mathcal{B}_{1122} + \mathcal{B}_{3223} - m^2\mathcal{B}_{1313} - \alpha^2 r^2 \mathcal{B}_{2323})f(r)$$
$$+ (r\mathcal{B}'_{3333} + rp' - r\mathcal{B}'_{2233} + \mathcal{B}_{3333} - 2\mathcal{B}_{2233} + \mathcal{B}_{1122} - \mathcal{B}_{3223})rf'(r)$$
$$+ (\mathcal{B}_{3333} - \mathcal{B}_{2233} - \mathcal{B}_{3223})r^2 f''(r)$$
$$+ (r\mathcal{B}'_{1133} - r\mathcal{B}'_{2233} - \mathcal{B}_{1111} + \mathcal{B}_{1122} + \mathcal{B}_{3223} - \mathcal{B}_{1313})mg(r)$$
$$+ (\mathcal{B}_{1133} - \mathcal{B}_{2233} + \mathcal{B}_{1331} - \mathcal{B}_{3223})mrg'(r) - r^2 k'(r) = 0. \tag{4.42}$$

Next, on substituting the expression for u from (4.38) in the boundary condition $(4.37)_1$, we deduce that

$$\alpha = n\pi/(\lambda_2 L), \tag{4.43}$$

where $n = 1, 2, 3, \ldots$ is the axial mode number. The boundary conditions for v are then automatically satisfied. It is therefore clear that the behaviour for different mode numbers n can be captured, equivalently, by varying the length L. Thus, in what follows it suffices to set $n = 1$ and to consider L as a parameter that reflects either changes in the axial mode number or changes in length.

¿From equations (4.40)–(4.42), we can express $f'''(r)$, $g''(r)$ and $k'(r)$ in terms of $f(r)$, $f'(r)$, $f''(r)$, $g(r)$, $g'(r)$ and $k(r)$, and hence we write the equations as a first-order system in the compact form

$$\frac{d\mathbf{y}}{dr} = \mathbf{G}(\mathbf{y}, r), \tag{4.44}$$

where $\mathbf{y} = (y_1, y_2, y_3, y_4, y_5, y_6)^{\mathrm{T}}$, $\mathbf{G} = (G_1, G_2, G_3, G_4, G_5, G_6)^{\mathrm{T}}$,

$$y_1 = f(r), \quad y_2 = f'(r), \quad y_3 = f''(r), \quad y_4 = g(r), \quad y_5 = g'(r), \quad y_6 = k(r), \tag{4.45}$$

and

$$G_1 = y_2, \quad G_2 = y_3, \quad G_4 = y_5, \tag{4.46}$$

while G_3, G_5, G_6 are lengthy expressions obtained by rearranging equations (4.40)–(4.42) and are not listed here.

In the same notation, the components of the incremental pressure boundary condition (4.27) are given as

$$
\left.
\begin{aligned}
&my_1 + y_4 - ry_5 = 0, \\
&(\alpha^2 r^2 + m^2 - 1)y_1 + ry_2 + r^2 y_3 = 0, \\
&(\mathcal{B}_{1133} - \mathcal{B}_{2233})(y_1 + my_4) + (\mathcal{B}_{3333} - \mathcal{B}_{2233} + \lambda_3 W_3)ry_2 - ry_6 = 0,
\end{aligned}
\right\}
\tag{4.47}
$$

each of which must hold on both $r = a$ and $r = b$. To obtain these use has been made of the conditions $\sigma_3 = \lambda_3 W_3 - p = 0$ on $r = a$ and $\sigma_3 = \lambda_3 W_3 - p = -P$ on $r = b$, and we have set $\dot{P} = 0$ on $r = b$.

To solve the system of first-order ordinary differential equations (with three independent solutions), we choose starting values at $r = a$ for three independent solutions given by

$$
\begin{pmatrix}
y_1^1(a) \; y_1^2(a) \; y_1^3(a) \\
y_4^1(a) \; y_4^2(a) \; y_4^3(a) \\
y_6^1(a) \; y_6^2(a) \; y_6^3(a)
\end{pmatrix}
=
\begin{pmatrix}
1 \; 0 \; 0 \\
0 \; 1 \; 0 \\
0 \; 0 \; 1
\end{pmatrix},
\tag{4.48}
$$

where, for each entry $y_i^j(a)$ in (4.48), subscripts $i = 1, 4, 6$, correspond to dependent variables in (4.44) while the superscript j refers to the jth set of initial values ($j = 1, 2, 3$).

Substituting each set of the initial values, that is each column of the matrix (4.48), into the boundary conditions (4.47) for $r = a$, we obtain

$$
\begin{pmatrix}
y_2^1(a) \; y_2^2(a) \; y_2^3(a) \\
y_3^1(a) \; y_3^2(a) \; y_3^3(a) \\
y_5^1(a) \; y_5^2(a) \; y_5^3(a)
\end{pmatrix}
=
\begin{pmatrix}
a_{11} & my_2^1(a) & a_{13} \\
a_{21} & -my_2^1(a)/a & -y_2^3(a)/a \\
m/a & 1/a & 0
\end{pmatrix},
\tag{4.49}
$$

where, for conciseness, we have introduced the notations

$$
a_{11} = \frac{\mathcal{B}_{2233} - \mathcal{B}_{1133}}{a(\mathcal{B}_{3333} - \mathcal{B}_{2233} + \lambda_3 W_3)}, \quad
a_{13} = \frac{1}{\mathcal{B}_{3333} - \mathcal{B}_{2233} + \lambda_3 W_3},
$$

$$
a_{21} = \frac{1 - m^2 - a^2\alpha^2 - ay_2^1(a)}{a^2},
$$

all terms being evaluated for $r = a$.

Equations (4.48) and (4.49) together give the initial values for equations (4.44). This initial value problem is solved numerically using the Adams-Moulton method (Gerald and Wheatley, 1984), with Predictor and Corrector given by

$$
\text{Predictor: } \mathbf{y}_{n+1} = \mathbf{y}_n + \frac{h}{24}(55\mathbf{G}_n - 59\mathbf{G}_{n-1} + 37\mathbf{G}_{n-2} - 9\mathbf{G}_{n-3}),
\tag{4.50}
$$

$$\text{Corrector: } \mathbf{y}_{n+1} = \mathbf{y}_n + \frac{h}{24}(9\mathbf{G}_{n+1} + 19\mathbf{G}_n - 5\mathbf{G}_{n-1} + \mathbf{G}_{n-2}), \qquad (4.51)$$

where $h = (b-a)/\omega$ is the step size and ω is the iteration number. Note that the Adams-Moulton method requires four sets of initial values at previous steps. These are calculated using the fourth-order Runge-Kutta method. Each method has local errors of $O(h^5)$. The solutions can be expressed as a linear combination of the three independent solutions $\mathbf{y}^1, \mathbf{y}^2, \mathbf{y}^3$. Thus,

$$\mathbf{y} = C_1\mathbf{y}^1 + C_2\mathbf{y}^2 + C_3\mathbf{y}^3, \qquad (4.52)$$

where $\mathbf{y}^i = (y_1^i, y_2^i, y_3^i, y_4^i, y_5^i, y_6^i)^{\mathrm{T}}$, $i = 1, 2, 3$.

Bifurcation may occur if there exist constants C_1, C_2, C_3, at least one of which is non-zero. For purposes of numerical computation in Section 6 we shall specialize to a particular strain-energy function, for which $\mathcal{B}_{1133} = \mathcal{B}_{2233} = 0$. On introducing this specialization and substituting (4.52) into the boundary conditions (4.47), we obtain three equations for C_1, C_2, C_3, namely

$$\left. \begin{array}{l} [my_1^i(b) + y_4^i(b) - by_5^i(b)]C_i = 0, \\[2mm] [(m^2 + \alpha^2 b^2 - 1)y_1^i(b) + b(y_2^i(b) + by_3^i(b))]C_i = 0, \\[2mm] [b(\mathcal{B}_{3333} + \lambda_3 W_3)y_2^i(b) - by_6^i(b)]C_i = 0, \end{array} \right\} \qquad (4.53)$$

evaluated for $r = b$, in each of which there is summation over the index i from 1 to 3. Thus, the bifurcation criterion is obtained by the vanishing of the determinant of coefficients of C_1, C_2, C_3, viz.

$$\begin{vmatrix} my_1^1(b) + y_4^1(b) - by_5^1(b) & my_1^2(b) + y_4^2(b) - by_5^2(b) & my_1^3(b) + y_4^3(b) - by_5^3(b) \\ My_1^1(b) + by_2^1(b) + b^2y_3^1(b) & My_1^2(b) + by_2^2(b) + b^2y_3^2(b) & My_1^3(b) + by_2^3(b) + b^2y_3^3(b) \\ bNy_2^1(b) - by_6^1(b) & bNy_2^2(b) - by_6^2(b) & bNy_2^3(b) - by_6^3(b) \end{vmatrix} = 0,$$

$$\qquad (4.54)$$

again with all terms evaluated for $r = b$, where $M = m^2 + \alpha^2 b^2 - 1$ and $N = \mathcal{B}_{3333} + \lambda_3 W_3$.

Substituting the equation

$$b^2 = a^2 + \lambda_z^{-1}(B^2 - A^2), \qquad (4.55)$$

i.e. equation $(4.9)_1$ with $R = B$, into (4.54), we obtain an equation for the value of a that satisfies the bifurcation criterion (4.54). The corresponding bifurcation pressure can be obtained from (4.14).

4.5   Numerical results and discussion

In the experiments of [74] and [10] silicone rubber tubes were used, and the numerical results of [52] were compared with experimental data for two thick-walled collapsible tubes reported by [10]. It is therefore appropriate to employ a strain-energy function that has been used extensively for fitting data on experiments for a wide range of rubberlike solids. Specifically, we apply the foregoing theory to the strain-energy function given by

$$W = \sum_{r=1}^{3} \mu_r(\lambda_1^{\alpha_r} + \lambda_2^{\alpha_r} + \lambda_3^{\alpha_r} - 3)/\alpha_r, \tag{4.56}$$

where μ_r and α_r, $r = 1, 2, 3$, are material constants (see, for example, [60]). Using the incompressibility condition (4.3) and the energy function $\hat{W}(\lambda_1, \lambda_2)$ defined by (4.5), we have

$$\hat{W}(\lambda_1, \lambda_2) = \sum_{r=1}^{3} \mu_r(\lambda_1^{\alpha_r} + \lambda_2^{\alpha_r} + (\lambda_1\lambda_2)^{-\alpha_r} - 3)/\alpha_r. \tag{4.57}$$

For the numerical calculations we use the material constants given by

$$\alpha_1 = 1.3, \quad \alpha_2 = 5.0, \quad \alpha_3 = -2.0,$$

$$\mu_1^* = 1.491, \quad \mu_2^* = 0.003, \quad \mu_3^* = -0.023, \tag{4.58}$$

as in [33], where $\mu_r^* = \mu_r/\mu$, $r = 1, 2, 3$, and μ is the shear modulus of the material in the reference configuration given by (see, for example, [57])

$$2\mu = \sum_{r=1}^{3} \mu_r\alpha_r. \tag{4.59}$$

Representative values of the aspect ratios of the tube are taken as $L/B = 1, 2.5, 5, 10$, and for numerical purposes, without loss of generality, we set $B = 1$ and change the value of the inner radius A to vary the thickness of the tube. Two thickness ratios are considered, namely, $A/B = 0.85$ (thinner tube) and $A/B = 0.5$ (thicker tube).

The qualitative nature of the results presented below are not unduly sensitive to the choice of material parameters in (4.56), and there are also many other forms of strain-energy function that could equally well be used to produce similar qualitative behaviour.

4.5.1   Equilibrium pressure curves

The dependence of the non-dimensional pressure $P^* = P/\mu$ on the circumferential stretch λ_a is illustrated in Fig. 4.2(a) in respect of the strain-energy function (4.57) with material constants (4.58) and for $A/B = 0.85$ and several values of λ_z. Figure 4.2(a) shows that

initially the external pressure increases slowly in order to compress the tube radially as λ_a is reduced from 1. Thereafter, there is a plateau where a significant increase in pressure does not produce significant further radial deformation of the tube. This trend becomes more pronounced as the value of λ_z increases. This graph should be compared with the pressure-area (internal cross sectional area of the tube) diagram, also known as the "tube law" and most commonly used for collapsible tubes [24]. Although the tube law is based on the post-buckling behaviour of tubes it doesn't take account of axial forces and bending moments.

The equal pressure curves corresponding to $P^* = 0, 0.5, 1$ are plotted in (λ_z, λ_a) space for $A/B = 0.5$ and 0.85 in Fig. 4.2(b), again using equation (4.14), except for $P^* = 0$, for which we have the connection

$$\lambda_a^2 \lambda_z = 1, \tag{4.60}$$

which is independent of the wall thickness ratio A/B. We observe that at least for the range of values of λ_z and λ_a considered, the equal pressure curves for the thicker tube $(A/B = 0.5)$ lie above those for the thinner one $(A/B = 0.85)$, indicating that to obtain the same deformation more pressure is required for the thicker tube, as should be expected.

4.5.2 Axisymmetric bifurcation

First, we consider axisymmetric modes of bifurcation, corresponding to $m = 0$ in (4.38). We set the longitudinal mode number n to be 1 and in Fig. 4.3 we plot axisymmetric bifurcation curves for $L/B = 2.5, 5, 10$ and 20 and $A/B = 0.85$. In this case, as well as curves for an external pressure, curves for an internal pressure are shown in order to compare with the results of [35]. With reference to the remarks on internal pressure following equation (4.14), we recall that the effect of internal pressure is captured by taking $P^* < 0$ here. It can then be seen that for a tube subjected to internal pressure our results coincide with those in [35] except for a factor 2, which means the curves in [35] for $L/B = 2x$ are the same for those here with $L/B = x$.[1]

When the tube is under external pressure $(P^* > 0)$, we note that the axisymmetric bifurcation curves all intersect the curve $P^* = 0$ in the region $0 < \lambda_z < 1$, which means that axisymmetric bifurcation cannot occur for tubes with $A/B = 0.85$ subjected to external pressure and axial extension (i.e. when $\lambda_z > 1$). In other words, under external pressure,

---

[1]Private communication with Dr. Haughton confirms that there is a factor of 2 missing in eq. (61) of [35].
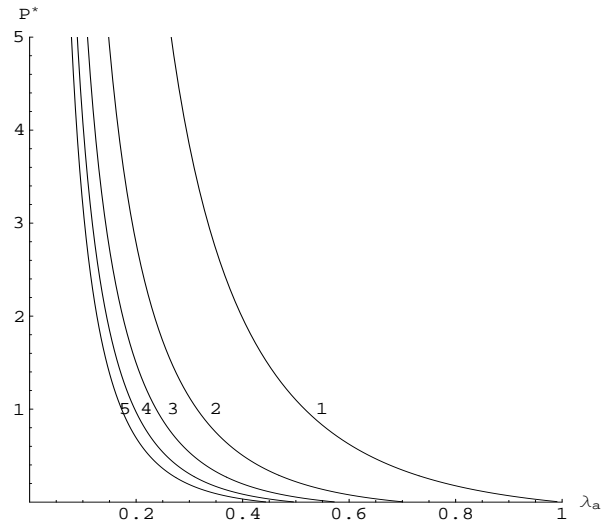
(a)
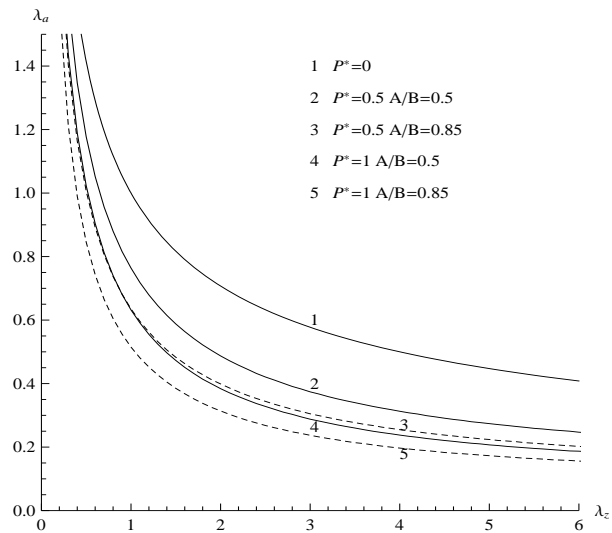
(b)

Figure 4.2: Plot of (a) the dimensionless pressure $P^* = P/\mu$ against λ_a for $A/B = 0.85$ and $\lambda_z = 1, 2, 3, 4, 5$, and (b) equal pressure curves in (λ_z, λ_a) space for $P^* = 0, 0.5, 1$, with $A/B = 0.85$ (dashed curves) and $A/B = 0.5$ (continuous curves).

axisymmetric bifurcation only occurs when a tube is axially compressed. This is not the case for tubes under internal pressure [35].

4.5.3 Asymmetric bifurcation

Since for tubes under external pressure, axisymmetric bifurcations do not occur when the tube is extended, we focus on asymmetric bifurcations henceforth.
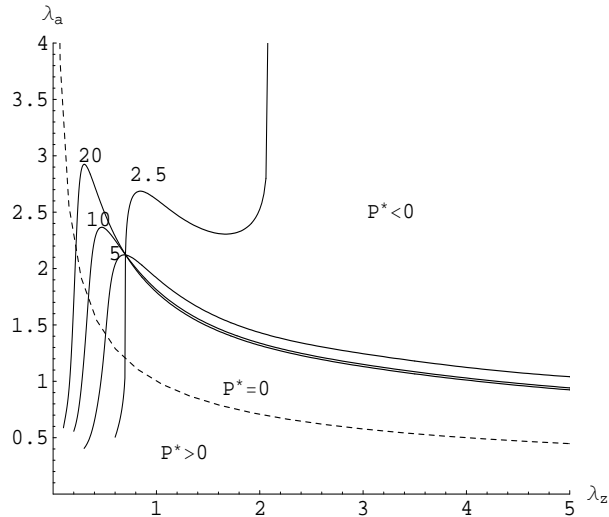
Figure 4.3: Plots of the axisymmetric bifurcation curves for mode $n = 1$ with aspect ratios $L/B = 2.5, 5, 10, 20$ and $A/B = 0.85$. The dashed curve corresponds to the zero pressure curve $P^* = 0$.

Thinner tube

In this section, all results are for the thinner tube $A/B = 0.85$. ¿From equation (4.43), we recall that either axial mode number n or length of the tube L can be varied to obtain equivalent results. We therefore set $n = 1$ and choose different values of the length L, and only azimuthal modes corresponding to $m = 1, 2, 3, 4$ are considered. Therefore, in the following, the mode number referred to is always the azimuthal mode number m. We restrict attention to $m \leqslant 4$ because higher mode number bifurcations are not usually observed in collapsible tube experiments. In any case, we have found that higher modes produce results very similar to those for $m = 4$. The asymmetric bifurcation curves are plotted using the bifurcation criterion (4.54) and the numerical method discussed in Section 5.

Figure 4.4 shows the mode 1 asymmetric bifurcation curves for $L/B = 1, 2.5, 5, 10$ and both internal and external pressure. For $P^* < 0$ (tubes under internal pressure), the results here are again in agreement with those of [35], with the factor 2 difference indicated earlier, and we do not discuss this case further. For $P^* > 0$ (tubes under external pressure), we see that as the axial stretch λ_z is increased towards 1, along the equal pressure curve $P^* = 0$ the value of λ_a at bifurcation decreases as the value of L/B increases from 2.5 to 10. This confirms the intuitive expectation that longer tubes buckle more easily than shorter ones.
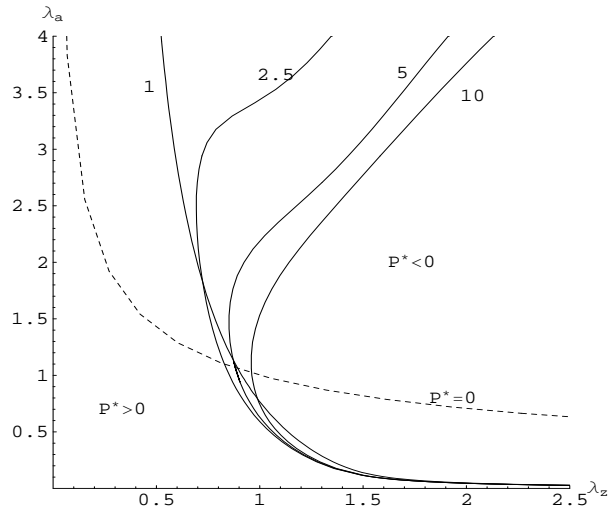
Figure 4.4: Mode $m = 1$ asymmetric bifurcation curves for $L/B = 1, 2.5, 5, 10$ and $A/B = 0.85$ in (λ_z, λ_a) space. The dashed curve is the equal pressure curve $P^* = 0$.
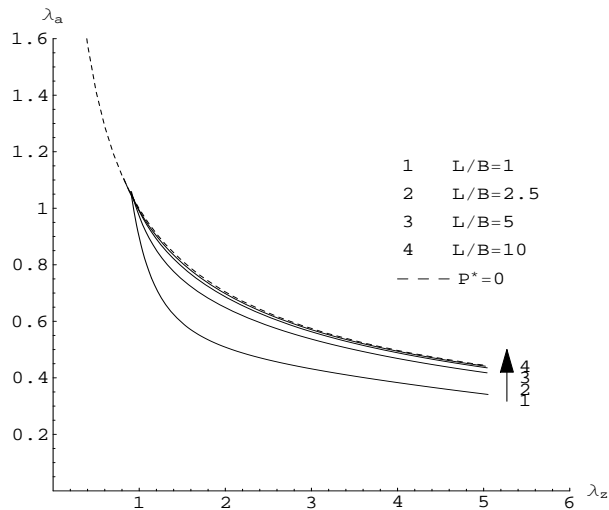
Figure 4.5: As in Fig. 4.4 but for azimuthal mode number $m = 2$.

In the region of axial extension, the tube with $L/B = 1$ bifurcates slightly more readily into mode 1 than the longer tubes. Figure 4.4 also shows that the tube can bifurcate into mode 1 for small axial compression (values of λ_z less than, but close to, 1). The value of λ_a at bifurcation seems to increase rapidly for λ_z below 1 (i.e. when the tube is axially compressed). However, under axial extension ($\lambda_z > 1$), bifurcation into mode 1 requires a relatively larger pressure than in axial compression and the corresponding value of λ_a becomes very small, as does the internal radius of the tube.

The mode 2 asymmetric bifurcation curves are shown in Fig. 4.5. It is interesting
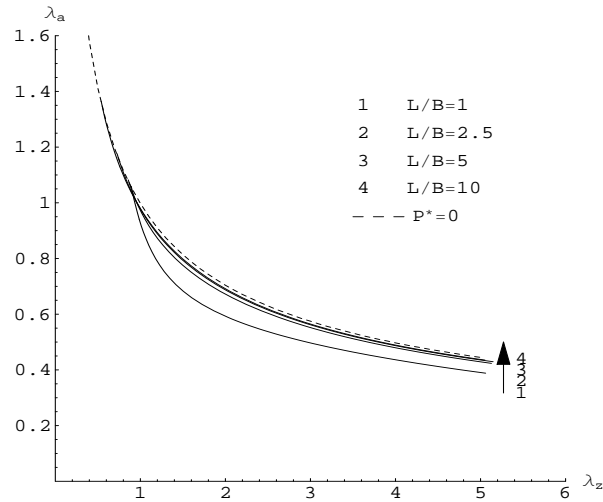
(a)
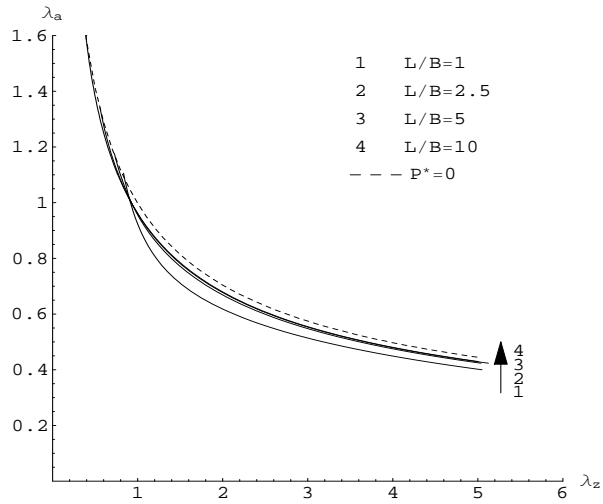
(b)

Figure 4.6: As in Fig. 4.4 but for (a) $m = 3$ and (b) $m = 4$.

to see that the bifurcation pressure for longer tubes ($L/B \geqslant 5$) approaches zero. Thus, although the bifurcation pressures required in the region of axial compression are similar for mode 1 and mode 2, much less pressure is required to achieve the mode 2 bifurcation in the region of axial extension. Figure 4.5 also shows that the mode 2 bifurcation does not depend significantly on the length of the tube unless the tube is very short (with L/B about 1).

Similar bifurcation behaviour is found for modes $m = 3$ and $m = 4$, as illustrated in Fig. 4.6. Compared with mode 2, the mode 3 and mode 4 curves are closer to (further from) the equal pressure line $P^* = 0$ for tubes with $L/B = 1$ ($L/B = 10$), and hence
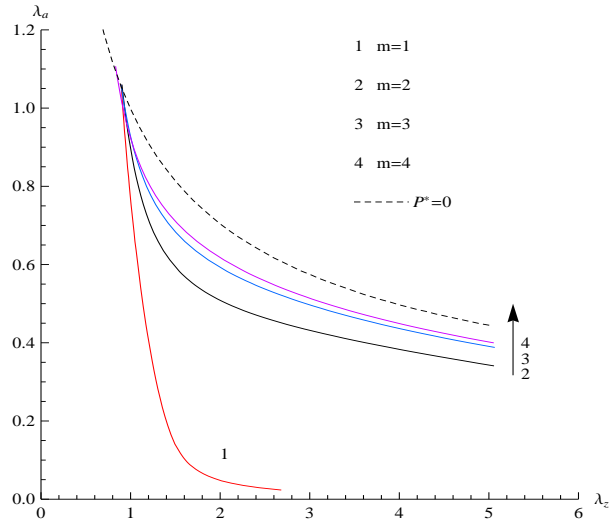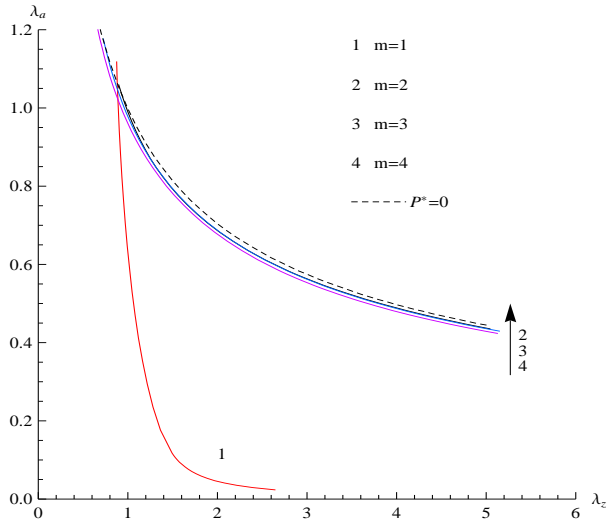
Figure 4.7: Asymmetric bifurcation curves for $m = 1, 2, 3, 4$ and $A/B = 0.85$ in (λ_z, λ_a) space: (a) $L/B = 1$; (b) $L/B = 5$.

the shorter tubes become more sensitive to a change in the external pressure for higher mode numbers, while for longer tubes, mode 2 become the most unstable mode. The differences in these modes can be seen more clearly in Fig. 4.7. Note that compared with higher modes, the mode 1 curve is much further from the $P^* = 0$ curve, especially as axial extension is increased. This means that unless the tube is slightly compressed, a much greater pressure is required for a tube to buckle into mode 1 than into higher modes. This trend is even stronger for the longer tubes.

Thicker tube

To illustrate the influence of different mode numbers on the behaviour of thicker tubes, we plot the bifurcation curves for $m = 1, 2, 3, 4$ in Fig. 4.8 for $A/B = 0.5$ separately for each value $L/B = 1$ and $L/B = 5$. In Fig. 4.8(a), for $L/B = 1$, it can be seen that the bifurcation behaviour for the thicker tube is similar to that for thinner tube, i.e. curves of modes $2, 3, 4$ are closer to each other than that for mode 1. Thus, under extension the tube may bifurcate into any of the modes $2, 3, 4$ but a relatively larger pressure is needed for mode 1 to be activated. Two major differences are observed between thinner and thicker tubes. One is that the mode $2, 3, 4$ curves are more separated for the thicker tube, the other is that for axial compression ($\lambda_z < 1$) the lower modes occur first, while for axial extension, mode 2 becomes the preferred mode for all values of λ_z. This is consistent with experimental observations and classical thin shell theory but is not so obvious for thinner tubes.

Figure 4.8(b) shows corresponding results for $L/B = 5$. The curves for modes $2, 3, 4$ do not intersect. Compared with the $L/B = 1$ tube, the separations of the curves for $m = 2, 3, 4$ are relatively large. The mode 1 curve has one point of intersection with each of the other higher mode curves. In the region of axial extension, as the external pressure increases, bifurcation occurs first in mode 2, followed by modes 3, 4 and 1 successively. For modes 3 and 4, the bifurcation values of λ_a (larger than 1) along the equal pressure curve $P^* = 0$ for $L/B = 5$ are larger than those for $L/B = 1$.

Bifurcation pressure

Since mode 2 is the most widely observed mode in tube collapse experiments (Bertram, 1987), we show the mode 2 bifurcation pressure against L/B in Fig. 4.9 for both $A/B = 0.5$ and $A/B = 0.85$ for comparison, with $\lambda_z = 1$ in each case. It can be seen that the curves tend to flatten when $L/B \geqslant 4$. This suggests that, for longer tubes, wall thickness rather than tube length is more important in determining the magnitude of the bifurcation pressure. As a result, the value of the bifurcation pressure P^* for $A/B = 0.85$ is much smaller than that for $A/B = 0.5$, and this will be discussed further later in this section. It should be noted that different vertical scales are used for the two plots.

To see the change of the bifurcation pressure with wall thickness and to compare our results with those in the literature (Bertram, 1987; Marzo et al, 2005; Weissman and Mockros, 1967) we use the reference wall thickness $H = B - A$ and the parameters D, Q
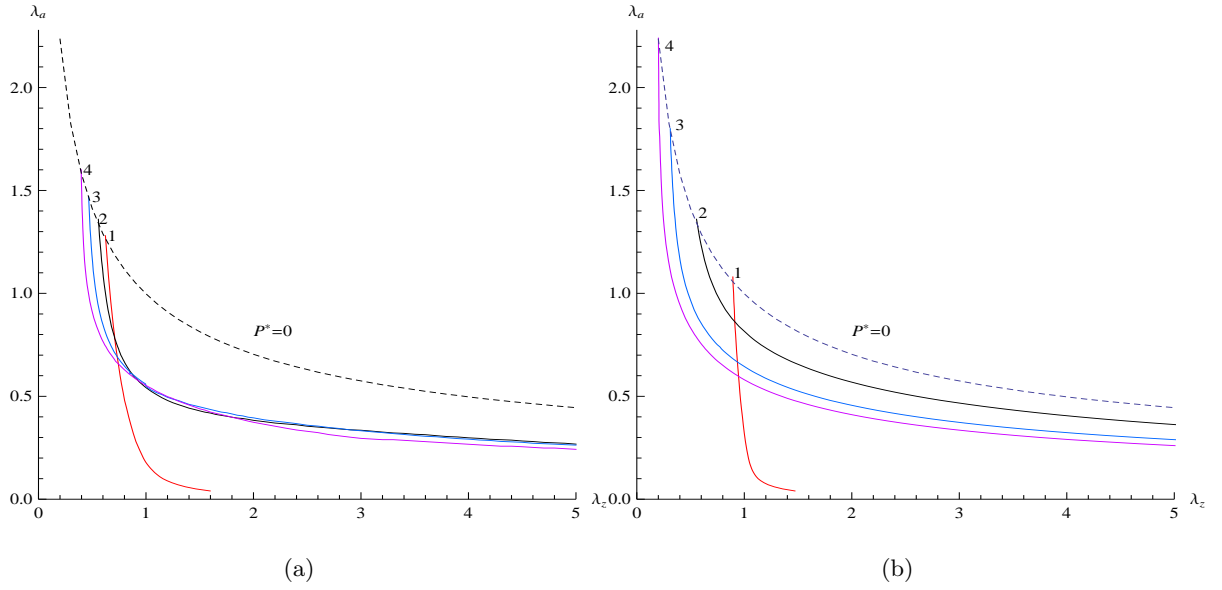
Figure 4.8: Asymmetric bifurcation curves for $m = 1, 2, 3, 4$ and $A/B = 0.5$ in (λ_z, λ_a) space: (a) $L/B = 1$; (b) $L/B = 5$.
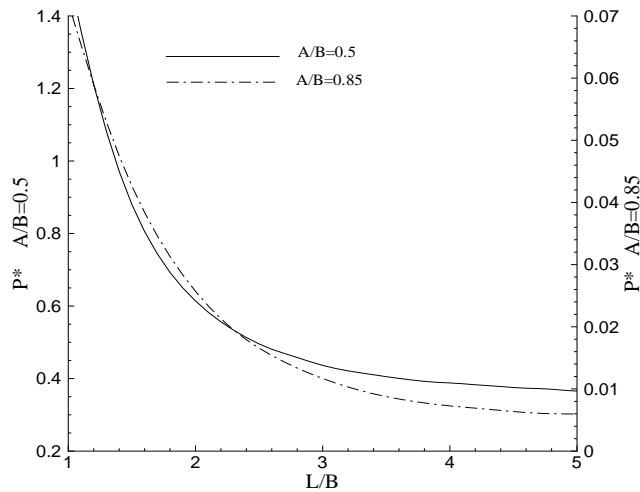
Figure 4.9: Plot of $P^* = P/\mu$ at bifurcation (mode $m = 2$) against L/B for $A/B = 0.5$ (continuous curve, left-hand scale) and $A/B = 0.85$ (dash-dot curve, right-hand scale) and $\lambda_z = 1$.

and P_k, defined by

$$D = \frac{2(B - A)}{\ln(B/A)}, \quad Q = \frac{EH^3}{12(1 - \nu^2)}, \tag{4.61}$$

and

$$P_k = \frac{Q}{(D/2)^3} = \frac{2E}{3(1 - \nu^2)} \left(\frac{H}{D} \right)^3, \tag{4.62}$$
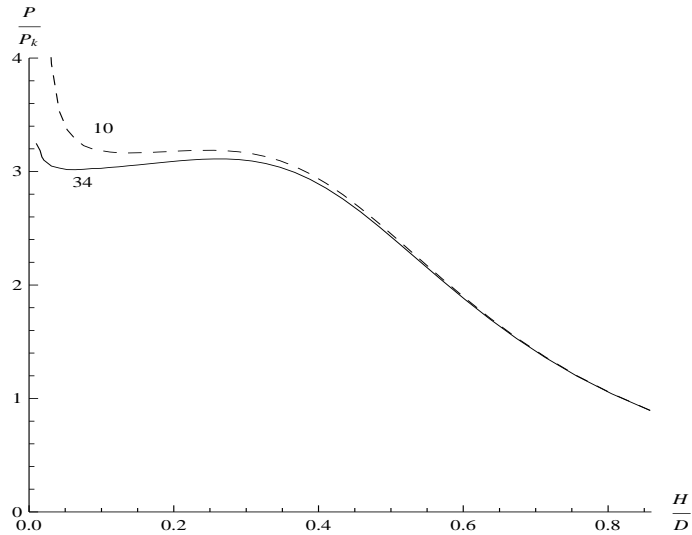
Figure 4.10: Mode 2 bifurcation pressure plotted in dimensionless form as P/P_k against H/D for $L/B = 10$ (dashed curve) and $L/B = 34$ (continuous curve) and $\lambda_z = 1.005$.

where, in the context of classical elasticity, E is Young's modulus and ν is Poisson's ratio. Here, D denotes the logarithmic mean diameter and Q is the flexural rigidity of the tube wall. The pressure P is non-dimensionalized by dividing by P_k.

Using the bifurcation criterion (4.54) combined with equations (4.14), $(4.61)_1$ and (4.62), we obtain the mode 2 bifurcation pressure shown in Fig. 4.10, plotted with P/P_k against H/D. We see that the thinner tube begins to bifurcate at a pressure close to the theoretical value $P/P_k = 3$ in the thickness range of $0.05 \sim 0.4$ in agreement with von Mises' prediction obtained from classical linear elasticity thin shell theory (von Mises, 1914). We emphasize again that our results are obtained from the incremental equations based on the full 3D theory of nonlinear elasticity, which provide the *exact* linearized bifurcation theory of elasticity, and our calculations are valid for underlying finite elastic deformations. To compare with Bertram's experimental results [10] and the numerical results of [52], the parameter $L/B = 34$ was used here. In fact, our results indicate that, for tubes with $L/B = 10$ and $L/B = 34$, when $0.05 < H/D < 0.4$ the values of P/P_k are in the range $2.9 \sim 3.2$. This explains why von Mises' prediction is confirmed by many different experiments and numerical simulations (Bertram, 1987; Marzo et al., 2005; Weissman and Mockros, 1967). In [10] and [52], only some limited values of P/P_k were presented for a set of given values of H/D. Likewise, in [74], results were only presented for $0 < H/D < 0.25$. Here, the bifurcation pressure is shown for a much wider range of H/D. It is interesting to note that the bifurcation pressure does not change significantly

for tubes with thickness ratio $0.05 < H/D < 0.4$.

However, our results show that towards the two ends of the H/D axis, the values of the bifurcation pressure for mode 2 differ from the classical prediction. For $H/D < 0.05$, the values of P/P_k are larger than 3. The shorter the tube, the greater the increase. For $L/B = 34$, $P/P_k = 3.24$ at $H/D = 0.01$ and for $L/B = 10$, it increases to 11.5 (see Fig. 4.10 and the $B/H = 50$ curve in Fig. 4.12). This discrepancy may be because in classical thin shell theory (Yamaki, 1984) the prebuckling state was assumed to be a membrane stress state. When $H/D < 0.05$ and $L/B < 34$, neglect of the curvature of the deflected surface caused by external pressure can lead to serious error (von Mises, 1914). However, von Mises' formula $P_{\mathrm{collapse}} = 3P_k$ is sufficiently accurate for shells with $L/B > 34$ (see page 73 in Yamaki, 1984). For $H/D > 0.4$, the curves for $L/B = 10$ and $L/B = 34$ almost coincide. The bifurcation pressure P/P_k drops below 3 as H/D increases, and decreases to 1 when $H/D = 0.8$. Caution is required with the physical interpretation of this result, since P_k is cubic H/D, which increases much faster than P as H/D is increased from 0.4. This trend can also be seen clearly in Fig. 4.13(a). In physical terms, a greater bifurcation pressure is still required to buckle the thicker tube, as expected, even though the ratio P/P_k is smaller.

Very short tubes

To illustrate further the dependence on tube length we now investigate briefly bifurcation of very short cylinders under axial compression and tension. Figure 4.11(a) presents bifurcation curves in (λ_z, λ_a) space for tubes with $L/B = 0.5$ and $A/B = 0.5$. Transition from low to high mode occurs in the range of axial compression at an intersection point where $\lambda_z \approx 0.62$. When $\lambda_z < 0.62$, modes $1, 2, 3$ occur first, while for $\lambda_z > 0.62$, the mode $m = 4$ becomes the most unstable one. Referring back to Fig. 4.8(b) for $L/B = 5$ we see that, by contrast, there is no intersection point among curves for $m = 2, 3, 4$ and the mode 2 curve is above the others in the whole range of λ_z except in the short interval $0.90 < \lambda_z < 0.95$ where the mode 2 curve is below that for mode 1. Axial extension does not affect the order of the bifurcation modes for either of the tubes with $L/B = 1$ and $L/B = 5$. The parameter L/B therefore plays a major role in the transition from high to low modes, which is also found for tubes with $A/B = 0.85$. The results represented in Fig. 4.11(a) are converted into the plots of P/P_k against λ_z in Fig. 4.11(b) by use of (4.61) and (4.62). Figure 4.11(b) shows that the P/P_k curve for mode 1 increases rapidly
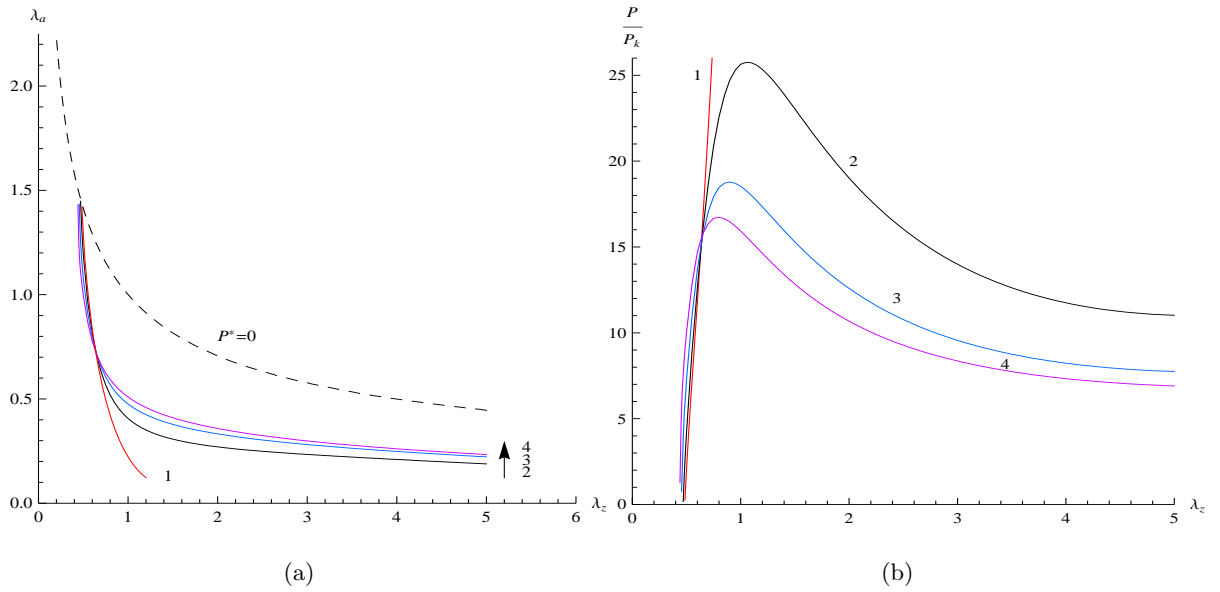
Figure 4.11: Asymmetric bifurcation curves for $m = 1, 2, 3, 4$, $L/B = 0.5$ and $A/B = 0.5$ (a): in (λ_z, λ_a) space; (b) in $(\lambda_z, P/P_k)$ space;

and monotonically, while for each mode $2, 3, 4$ there is a pressure maximum, occurring at $\lambda_z = 1.05, 0.90, 0.80$, respectively. Tubes subjected to sufficiently large axial compression or tension tend to bifurcate easily, while for $0.8 < \lambda_z < 1.05$ bifurcation requires a larger pressure. We can therefore conclude that either a large axial compression or axial tension reduces the axial stiffness of the cylinders.

The most unstable mode

To find the most unstable modes for different lengths and wall thicknesses, similarly to the predictions of classical thin shell theory (Yamaki, 1984), we plot the critical bifurcation curves in Fig. 4.12. It is seen that for a thin shell, $B/H = 50$, the results are in excellent quantitative agreement with those of Yamaki (1984, figure 2.12, for boundary condition S4). There exists only a small discrepancy due to the slightly different boundary conditions used here. In other words, if the wall is thin, then higher modes are more unstable for shorter tubes. However, as the wall thickness is increased, the critical higher modes become fewer, and mode 2 becomes more and more dominant. Eventually, for $B/H < 2$ and $L/B > 1.2$ it remains the only bifurcation mode. For instance, in the range of $4 < L/B < 10$, a thin tube with $B/H = 50$, bifurcates into the $m = 2$ mode, whereas thick-walled tube with $B/H = 6.67$, bifurcates into the $m = 3$ mode. In the context of axial compression of steel cylinders undergoing plastic deformation a very similar distribution
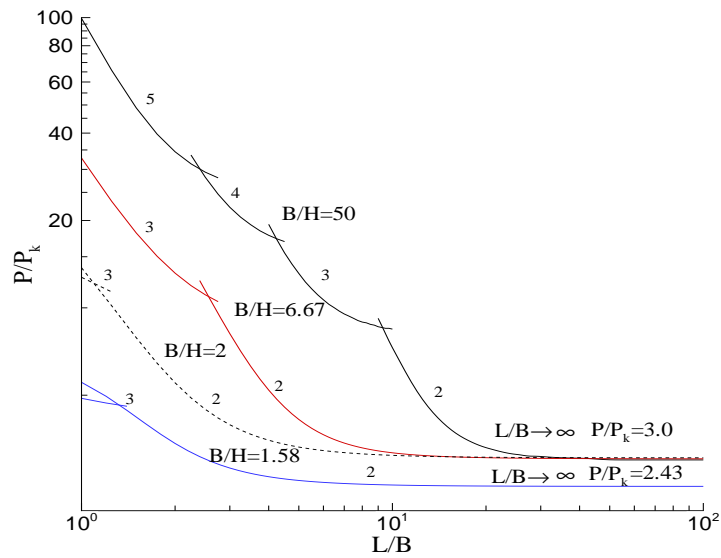
Figure 4.12: Bifurcation pressure plotted in dimensionless form as P/P_k against L/B for $B/H = 50$ (black curves), $B/H = 6.67$ (red curves), $B/H = 2$ (dashed curves), $B/H = 1.58$ (blue curves) with different mode numbers and $\lambda_z = 1$.

of bifurcation modes was found by [5] experimentally and [6] analytically. Apart from the type of material behaviour, this differs from the present analysis since we are considering external pressure rather than axial compression and we have fixed $\lambda_z = 1$ in Fig. 4.12. Figure 4.7(a) shows that for tubes with $A/B = 0.85$ (equivalent to $B/H = 6.67$) under external pressure and axial extension, the higher modes are more unstable. Another interesting phenomenon is that the thicker the tube the smaller the value of L/B at which the curve flattens. The curves for tubes with $B/H = 50, 6.67, 2$ show that as $L/B \rightarrow \infty$, P/P_k approaches 3.0, which is in agreement with the thin shell theory prediction. But for the very thick tube with $B/H = 1.58$, P/P_k approaches 2.43. The bifurcation pressure for thick tubes with $H/D > 0.4$ drops below 3.0 (see also Fig. 4.10).

4.5.4   Discussion

In this chapter, we have investigated the nonlinear buckling behaviour of thick-walled circular cylinder tubes under external pressure combined with axial loading. Our study is particularly useful in determining the buckling of thick-walled tubes, which is beyond the limit of validity of thin shell theory. This work has been conducted with a background in mind of the bifurcation behaviour of collapsible tubes conveying internal flow. Although

we note that the essential difference between this study and studies by the collapsible tube flow community [36, 39] [13] is that no fluid-structure interactions are considered. Here, the (external) pressure is acting as a (prescribed) static load, which contrasts with the strong viscous pressure when an internal flow is present. However, in the context of critical buckling, it has been found that these different mechanisms (static pressure load or flow-induced pressure load) lead to similar results except that a substantially higher pressure drop is required to achieve the same level of collapse for the static load case [39].

The most interesting finding is that for wall thickness ratios A/B greater than about 0.5, mode 2 seems to be the dominant critical buckling mode unless the tubes are extremely short (e.g., $L/B \lesssim 1.2$). This is different from the predictions of classical thin shell theory [77], but agrees with the fact that in many thick-walled tube experiments, in particular those of [10, 11] and [13], only mode 2 buckling has been observed regardless of the tube length used. The fact that in experiments the prevailing mode is mode 2 cannot be fully explained by thin shell theory. This is because when fluid-structure interaction is involved, the effect of the fluid flow is to increase the viscous pressure drop, which induces an additional compressive load at the downstream end of the tube. As a result, only the compressed downstream part of the tube actually participates in the buckling, which is then similar to the buckling of a short tube [39]. If the thin shell theory were to be valid, this would induce the buckling to occur in a higher mode. The reason why this didn't happen in the experiments is that, for thicker tubes, mode changes no longer happen, and long thick tubes were used in experiments [11, 13]. As illustrated in Fig. 4.12, for long thick tubes, only mode 2 occurs. As indicated above, our study shows that if A/B is greater than about 0.5, then the critical buckling mode will remain as mode 2 except for very short tubes.

Although the von Mises formula is derived for thin-walled tubes, experimental measurements have shown that it also predicts the bifurcation pressure for thick-walled tubes reasonably well [74]. Our results show that this is because the bifurcation pressure P/P_k is insensitive to the change of wall thickness H/D for the range of $0.05 < H/D < 0.4$. If the tube is sufficiently thin or sufficiently thick, then the von Mises formula is no longer accurate, and P/P_k actually increases in the thin wall extreme, and decreases in the thicker wall region.

In order to have a more direct comparison with the Weissman and Mockros experiments, we plot the bifurcation pressure in terms of P against H/D in Fig. 4.13. This

is obtained using the bifurcation criterion (4.54) combined with equation (4.14) and the equation

$$\mu = \frac{E}{2(1+\nu)}, \tag{4.63}$$

where (for an incompressible material) $\nu = 0.5$. The value $E = 300\,\text{psi}$ ($= 2.07\,\text{MPa}$) adopted by [74] then gives $\mu = 0.69\,\text{MPa}$, which is used to calculate the bifurcation pressure.

It can be seen that for a very thin tube ($0 < H/D < 0.1$), bifurcation occurs at a small external pressure. For tubes with larger wall thickness, when $H/D > 0.1$, the bifurcation pressure increases rapidly. For $0 < H/D < 0.4$, our results are in accord with the experimental results of [74] and von Mises' formula. When $H/D > 0.4$, the latter curve increases more rapidly than our results.

Although we have considered a tube of finite length, a limitation of the present study is that we have initiated the bifurcation analysis from a deformed circular cylindrical configuration and adopted rather special incremental boundary conditions on the ends of the tube. These might prevent realistic post-buckling behaviour for which large deformations can occur in either the axial or azimuthal direction near the ends. Thus, our results only apply for the initial bifurcation behaviour. Many interesting phenomena, such as self-exited oscillations in collapsible tubes conveying fluid, occur in the post-buckling phase, where the cross-sectional area typically takes on an elliptical or dumbbell shape. These are excluded in the present analysis.

4.6   Conclusion

Axisymmetric and asymmetric bifurcations of circular cylinders under external pressure combined with axial loading have been analyzed in detail using a particular model strain-energy function appropriate for nonlinear elastic deformations of rubberlike materials. Unlike the models used by [72] and [77], which are applicable only for thin-walled tubes, this study presents results for a wide range of tube wall thickness on the basis of the exact 3D theory of finite elasticity. A more general description of the bifurcation behaviour of thick-walled tubes subject to external pressure combined with axial loading, including axial compression and extension, has been presented. Good agreement with previous studies has been found, and extensive comparisons with results for thin-shell theory are made. Our results show that the critical bifurcation pressure deviates from the thin shell prediction
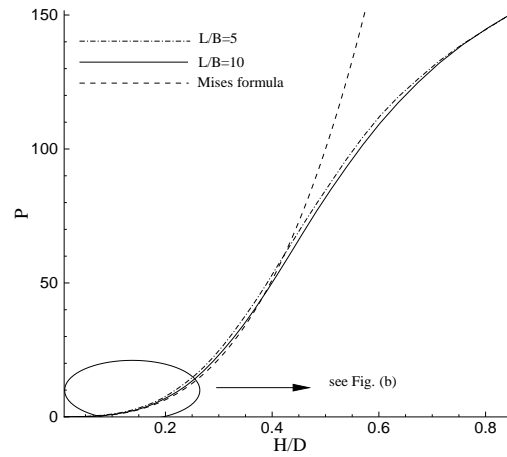
(a)
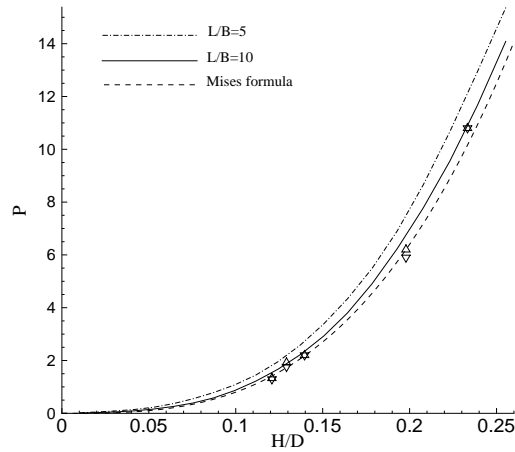
(b)

Figure 4.13: (a) Mode $m = 2$ bifurcation pressures P vs. H/D for silicone rubber tubes for $\lambda_z = 1.005$; the continuous curve is for $L/B = 10$, and dash-dot curve is for $L/B = 5$. The dashed curve corresponds to von Mises' theoretical result. (b) the enlarged area indicated in (a). The symbols are from the Weissman and Mockros experimental results: ∇ represents bifurcation points at 50% volume collapse and $\triangle$ at 70%.

in both the very thin and thick-walled regimes. For very short and sufficiently thick tubes, transition from lower to higher modes occurs in the range of axial compression. We have also shown that, contrary to thin-shell theory, for sufficiently thick tubes, transition from lower to higher modes does not occur for sufficiently short tubes. Instead, mode 2 bifurcation becomes the sole dominant mode.

Chapter 5

Nonlinear axisymmetric deformations

In this chapter, we restrict our attention to the nonlinear axisymmetric deformations of elastic tubes under external pressure.

5.1 Basic equations

We consider an initially stress-free thick-walled circular cylindrical tube. In this reference configuration the geometry of the tube is described in terms of cylindrical polar coordinates R, Θ, Z by

$$A \leq R \leq B, \quad 0 \leq \Theta \leq 2\pi, \quad 0 \leq Z \leq L, \tag{5.1}$$

where A and B, respectively, are the inner and outer radii and L is the length of the tube. Let $\mathbf{E}_R, \mathbf{E}_\Theta, \mathbf{E}_Z$ denote the associated unit basis vectors. The deformed geometry is described in terms of cylindrical polar coordinates r, θ, z with corresponding unit basis vectors $\mathbf{e}_r, \mathbf{e}_\theta, \mathbf{e}_z$. In what follows we shall consider axisymmetric deformations of the tube.

5.1.1 Deformation

Let $\mathbf{u}$ denote the displacement vector, which, for axisymmetric deformations, may be expressed in the form

$$\mathbf{u} = u(R, Z)\mathbf{e}_r + w(R, Z)\mathbf{e}_z. \tag{5.2}$$

The deformation gradient tensor $\mathbf{F}$ is given by

$$\mathbf{F} = (1 + u_R)\mathbf{e}_r \otimes \mathbf{E}_R + u_Z\mathbf{e}_r \otimes \mathbf{E}_Z + (1 + \frac{u}{R})\mathbf{e}_\theta \otimes \mathbf{E}_\Theta$$

$$+ w_R\mathbf{e}_z \otimes \mathbf{E}_R + (1 + w_Z)\mathbf{e}_z \otimes \mathbf{E}_Z, \tag{5.3}$$

where the subscripts R and Z on u and w indicate the partial derivatives $\partial/\partial R$ and $\partial/\partial Z$, respectively. The matrix representation of (5.3) with respect to both sets of cylindrical polar coordinates is

$$\mathsf{F} = \begin{pmatrix} 1 + u_R & 0 & u_Z \\ 0 & 1 + u/R & 0 \\ w_R & 0 & 1 + w_Z \end{pmatrix}.$$

Using (5.3), we may calculate the right Cauchy-Green deformation tensor, defined by $\mathbf{C} = \mathbf{F}^\mathrm{T}\mathbf{F}$, where $^\mathrm{T}$ denotes the transpose. This yields

$$\mathbf{C} = [(1 + u_R)^2 + w_R^2]\mathbf{E}_R \otimes \mathbf{E}_R + (1 + u/R)^2\mathbf{E}_\Theta \otimes \mathbf{E}_\Theta + [u_Z^2 + (1 + w_Z)^2]\mathbf{E}_Z \otimes \mathbf{E}_Z$$

$$+ [u_Z(1 + u_R) + (1 + w_Z)w_R](\mathbf{E}_R \otimes \mathbf{E}_Z + \mathbf{E}_Z \otimes \mathbf{E}_R). \tag{5.4}$$

We also note the polar decomposition (2.6) discussed in Chapter 1, where $\mathbf{R}$ is a proper orthogonal tensor and $\mathbf{U}$ is the right stretch tensor, which is positive definite and symmetric. Thus, $\mathbf{C} = \mathbf{U}^2$. The eigenvalues of $\mathbf{U}$ are the principal stretches of the deformation, denoted λ_i, $i = 1, 2, 3$. The principal axes of $\mathbf{C}$ and $\mathbf{U}$ coincide and we can see immediately from (5.4) that $\mathbf{E}_\Theta$ is a (Lagrangian) principal axis, which corresponds to the principal stretch $\lambda_2 = 1 + u/R$. The other two principal axes lie parallel to the (R, Z) plane and can be defined in terms of an angle ψ via

$$\mathbf{E}'_R = \cos\psi\mathbf{E}_R + \sin\psi\mathbf{E}_Z, \quad \mathbf{E}'_Z = -\sin\psi\mathbf{E}_R + \cos\psi\mathbf{E}_Z. \tag{5.5}$$

The connection between principal and reference axes can be seen clearly in Fig. 5.1.

The corresponding principal stretches are taken as λ_1 and λ_3, respectively. Then, we have

$$\mathbf{C} = \lambda_1^2\mathbf{E}'_R \otimes \mathbf{E}'_R + \lambda_2^2\mathbf{E}_\Theta \otimes \mathbf{E}_\Theta + \lambda_3^2\mathbf{E}'_Z \otimes \mathbf{E}'_Z. \tag{5.6}$$

5.1.2 Material properties and equilibrium

The material of the tube is considered to be incompressible, so that the constraint

$$J = \det\mathbf{F} = \det\mathbf{U} = \lambda_1\lambda_2\lambda_3 \equiv 1 \tag{5.7}$$
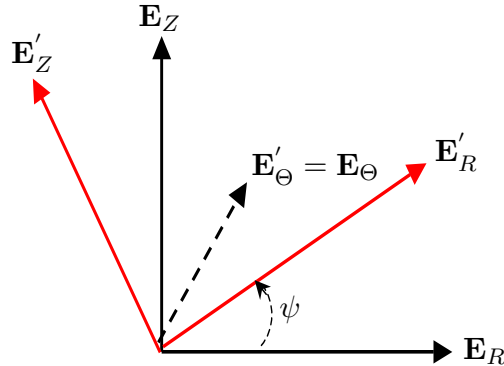
Figure 5.1: The connection between principal and reference axes.

must be satisfied for every material point $\mathbf{X}$. Subject to this constraint, the elastic proper-
ties of the material can be described in terms of a strain-energy function $W(\mathbf{F})$, defined per
unit volume. By objectivity $W(\mathbf{F}) = W(\mathbf{U})$. The associated Biot stress tensor, denoted
here by $\mathbf{T}$, is then given by

$$\mathbf{T} = \frac{\partial W}{\partial \mathbf{U}} - p\mathbf{U}^{-1}, \tag{5.8}$$

where p is a Lagrange multiplier associated with the constraint (5.7). For details of the
Biot stress tensor we refer to [60]. For the considered deformation p is a function only of
R and Z.

Now, for an isotropic material W is a function only of the principal stretches $\lambda_1, \lambda_2, \lambda_3$,
again subject to (5.7), and $\mathbf{T}$ has the same principal axes as $\mathbf{U}$. The principal Biot stresses
are then simply

$$t_i = \frac{\partial W}{\partial \lambda_i} - p\lambda_i^{-1}, \quad i = 1, 2, 3. \tag{5.9}$$

Let $\mathbf{S}$ denote the nominal stress tensor. Then, since the material is isotropic, we have

$$\mathbf{S} = \mathbf{T}\mathbf{R}^{\mathrm{T}}, \tag{5.10}$$

where $\mathbf{R}$ is obtained from the polar decomposition as $\mathbf{R} = \mathbf{F}\mathbf{U}^{-1}$. As mentioned in
Chapter 1, in the absence of body forces the equilibrium equation is expressed in terms of
the nominal stress as

$$\mathrm{Div}\,\mathbf{S} = \mathbf{0}, \tag{5.11}$$

where Div is the divergence operator with respect to $\mathbf{X}$. Alternatively, in terms of the Cauchy stress tensor, denoted $\boldsymbol{\sigma}$ and given by $\boldsymbol{\sigma} = J^{-1}\mathbf{FS}$, the equilibrium equation may be written equivalently as

$$\operatorname{div}\boldsymbol{\sigma} = \mathbf{0}. \tag{5.12}$$

The principal Cauchy stresses are given by

$$\sigma_i = \lambda_i \frac{\partial W}{\partial \lambda_i} - p, \quad i = 1, 2, 3. \tag{5.13}$$

On the external lateral surface of the tube a pressure P, per unit deformed area, is applied, while the inner surface is kept free of traction. The boundary conditions on these surfaces may then be given as

$$\mathbf{S}^{\mathrm{T}}\mathbf{N} = \begin{cases} -P\mathbf{F}^{-\mathrm{T}}\mathbf{N} & \text{on } R = B \\ \mathbf{0} & \text{on } R = A, \end{cases} \tag{5.14}$$

where $\mathbf{N}$ is the unit outward normal to the lateral surface of the tube in the reference configuration, i.e. $\mathbf{N} = \mathbf{E}_R$ on $R = B$ and $\mathbf{N} = -\mathbf{E}_R$ on $R = A$.

On the ends of the tube the displacement is taken to vanish except for the special case in which we consider the deformation to maintain circular symmetry. Thus,

$$u = w = 0 \quad \text{on } Z = 0, L. \tag{5.15}$$

For the linear and nonlinear cases, the boundary conditions are illustrated in Fig. 5.2.

For the specific calculations we make use of the neo-Hookean strain-energy function, which is given by (2.54).

5.2 Linear and nonlinear equations

We consider the nonlinear formulation with the boundary conditions specified above together with two special cases: the first is nonlinear but assumes that the deformation is radially symmetric, for which an analytical solution is obtained, while the second is based on the linear theory of elasticity. These special cases serve to verify our C++ code and to highlight, in particular, the differences between the linear and nonlinear results.

5.2.1 Radially symmetric case

If the deformation is radially symmetric then the deformed geometry has the form

$$a \leq r \leq b, \quad 0 \leq \theta \leq 2\pi, \quad 0 \leq z \leq l, \tag{5.16}$$
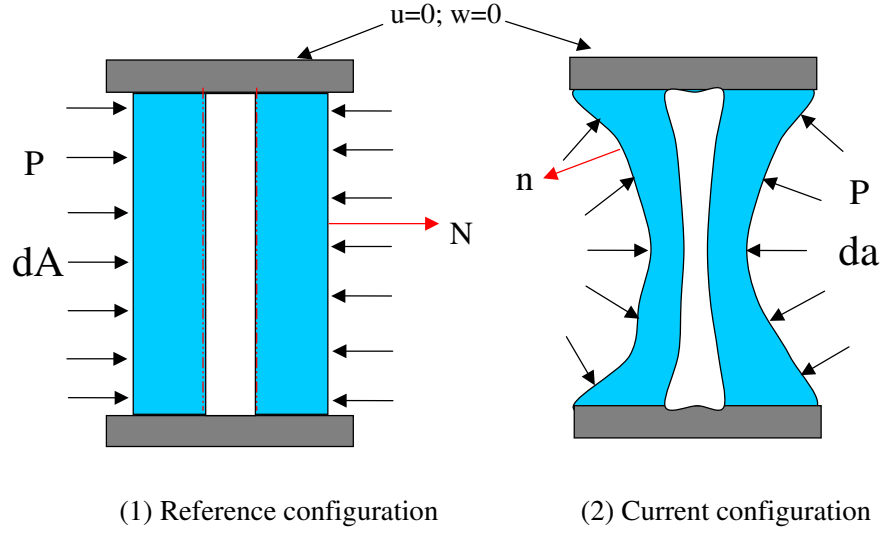
Figure 5.2: Boundary conditions for linear and nonlinear cases (a) in Reference configuration (b) in current configuration.

where a and b, respectively, are the deformed inner and outer radii of the tube and l is its length.

For this special case, we assume that the displacement is given by $\mathbf{u} = u(R)\mathbf{e}_r$, so that there is no dependence on Z and w is identically zero. Then the deformation gradient tensor $\mathbf{F}$ in (5.3) specializes accordingly, and the right Cauchy-Green deformation tensor in (5.4) reduces to

$$\mathbf{C} = (1 + u_R)^2 \mathbf{E}_R \otimes \mathbf{E}_R + (1 + u/R)^2 \mathbf{E}_\Theta \otimes \mathbf{E}_\Theta + \mathbf{E}_Z \otimes \mathbf{E}_Z. \tag{5.17}$$

It follows that the Lagrangian principal axes coincide with the basis vectors $\mathbf{E}_R, \mathbf{E}_\Theta, \mathbf{E}_Z$ and the principal stretches are

$$\lambda_1 = 1 + u_R, \quad \lambda_2 = 1 + \frac{u}{R}, \quad \lambda_3 = 1. \tag{5.18}$$

Furthermore, $\mathbf{S} = \mathbf{T}$ and hence

$$\mathbf{S} = t_1 \mathbf{E}_R \otimes \mathbf{E}_R + t_2 \mathbf{E}_\Theta \otimes \mathbf{E}_\Theta + t_3 \mathbf{E}_Z \otimes \mathbf{E}_Z. \tag{5.19}$$

The equilibrium equation (5.11) specializes to the single component

$$S_{Rr,R} + \frac{1}{R}(S_{Rr} - S_{\Theta\theta}) = 0, \tag{5.20}$$

where $S_{Rr} = t_1$, $S_{\Theta\theta} = t_2$ and $,_R \equiv \mathrm{d}/\mathrm{d}R$. For the neo-Hookean material (2.54) we then obtain, on use of (5.18),

$$t_1 = \mu\lambda_1 - p\lambda_2, \quad t_2 = \mu\lambda_2 - p\lambda_1, \quad t_3 = \mu - p, \tag{5.21}$$

where the incompressibility condition $\lambda_1\lambda_2 = 1$, or equivalently

$$u + (R + u)u_R = 0, \tag{5.22}$$

has been used. The latter can be integrated to give $r = R + u$ in the form

$$r^2 = R^2 + a^2 - A^2. \tag{5.23}$$

The component form of the boundary condition (5.14) may now be written

$$S_{Rr} \equiv t_1 = \begin{cases} -P\lambda_2 & \text{on } R = B \\ 0 & \text{on } R = A. \end{cases} \tag{5.24}$$

Using (5.21) and noting that $R\lambda_{2,R} = \lambda_1 - \lambda_2$ we may integrate (5.20) and use the boundary conditions (5.24) to obtain

$$P = \mu \ln\left(\frac{Ab}{Ba}\right) + \frac{1}{2}\mu\left(\frac{A^2}{a^2} - \frac{B^2}{b^2}\right). \tag{5.25}$$

5.2.2 The linear case

In the linear theory of incompressible isotropic elasticity the (Cauchy) stress tensor is given by

$$\boldsymbol{\sigma} = -p\mathbf{I} + \mu[\mathrm{grad}\,\mathbf{u} + (\mathrm{grad}\,\mathbf{u})^{\mathrm{T}}], \tag{5.26}$$

where $\mathbf{I}$ is the identity tensor.

Then, for the axisymmetric situation, the equilibrium equation (5.12) has two components that are not satisfied trivially, namely

$$\sigma_{rr,r} + \sigma_{zr,z} + \frac{1}{r}(\sigma_{rr} - \sigma_{\theta\theta}) = 0, \tag{5.27}$$

$$\sigma_{rz,r} + \sigma_{zz,z} + \frac{1}{r}\sigma_{rz} = 0, \tag{5.28}$$

and the incompressibility constraint is

$$u_r + \frac{u}{r} + w_z = 0. \tag{5.29}$$

The boundary conditions (5.15) are unchanged, but (5.14) may be reduced to

$$\boldsymbol{\sigma}\mathbf{n} = \begin{cases} -P\mathbf{n} & \text{on } R = B \\ \mathbf{0} & \text{on } R = A, \end{cases} \tag{5.30}$$

there being no distinction between the deformed and reference configurations.

5.2.3 The nonlinear case

Comparing (5.4) and (5.6) and using (5.5), we obtain

$$\lambda_1^2 \cos \psi^2 + \lambda_3^2 \sin \psi^2 = (1 + u_R)^2 + w_R^2, \tag{5.31}$$

$$\lambda_1^2 \sin \psi^2 + \lambda_3^2 \cos \psi^2 = u_Z^2 + (1 + w_Z)^2, \tag{5.32}$$

$$(\lambda_1^2 - \lambda_3^2) \sin \psi \cos \psi = u_Z(1 + u_R) + w_R(1 + w_Z), \tag{5.33}$$

and $\lambda_2 = 1 + u/R$. From (5.31)–(5.33), it follows that

$$(\lambda_1^2 - \lambda_3^2) \cos 2\psi = w_R^2 - u_Z^2 + (1 + u_R)^2 - (1 + w_Z)^2, \tag{5.34}$$

$$(\lambda_1^2 - \lambda_3^2) \sin 2\psi = 2[u_Z(1 + u_R) + w_R(1 + w_Z)]. \tag{5.35}$$

It turns out that we must take $\lambda_1 > \lambda_3$, and hence we obtain

$$2\lambda_1 = \sqrt{(u_Z - w_R)^2 + (u_R + w_Z + 2)^2} + \sqrt{(u_Z + w_R)^2 + (u_R - w_Z)^2}, \tag{5.36}$$

$$2\lambda_3 = \sqrt{(u_Z - w_R)^2 + (u_R + w_Z + 2)^2} - \sqrt{(u_Z + w_R)^2 + (u_R - w_Z)^2}. \tag{5.37}$$

Recalling that the Biot stress tensor has the same principal axes as $\mathbf{U}$ we may write

$$\mathbf{T} = t_1 \mathbf{E}'_R \otimes \mathbf{E}'_R + t_2 \mathbf{E}_\Theta \otimes \mathbf{E}_\Theta + t_3 \mathbf{E}'_Z \otimes \mathbf{E}'_Z, \tag{5.38}$$

and hence from (5.10) with $\mathbf{R} = \mathbf{F}\mathbf{U}^{-1}$, we obtain the components of the nominal stress tensor in the form

$$\begin{aligned}
S_{Rr} &= (\lambda_1^{-1}t_1 - \lambda_3^{-1}t_3)u_Z \sin \psi \cos \psi + (1 + u_R)(\lambda_1^{-1}t_1 \cos^2 \psi + \lambda_3^{-1}t_3 \sin^2 \psi), \\
S_{Rz} &= (\lambda_1^{-1}t_1 - \lambda_3^{-1}t_3)(1 + w_Z) \sin \psi \cos \psi + w_R(\lambda_1^{-1}t_1 \cos^2 \psi + \lambda_3^{-1}t_3 \sin^2 \psi), \\
S_{Zr} &= (\lambda_1^{-1}t_1 - \lambda_3^{-1}t_3)(1 + u_R) \sin \psi \cos \psi + u_Z(\lambda_1^{-1}t_1 \sin^2 \psi + \lambda_3^{-1}t_3 \cos^2 \psi), \\
S_{Zz} &= (\lambda_1^{-1}t_1 - \lambda_3^{-1}t_3)w_R \sin \psi \cos \psi + (1 + w_Z)(\lambda_1^{-1}t_1 \sin^2 \psi + \lambda_3^{-1}t_3 \cos^2 \psi), \tag{5.39}
\end{aligned}$$

together with $S_{\Theta\theta} = t_2$.

The appropriate specialization of the equilibrium equation (5.11) then yields the two equations

$$S_{Rr,R} + S_{Zr,Z} + \frac{1}{R}(S_{Rr} - S_{\Theta\theta}) = 0, \tag{5.40}$$

$$S_{Rz,R} + S_{Zz,Z} + \frac{1}{R}S_{Rz} = 0, \tag{5.41}$$

the incompressible condition is

$$(1 + u/R)[(1 + u_R)(1 + w_Z) - u_Z w_R] = 1, \tag{5.42}$$

and the boundary condition (5.14) specializes to

$$S_{Rr} = \begin{cases} -P(1 + u/R)(1 + w_Z) & \text{on } R = B \\ 0 & \text{on } R = A, \end{cases} \tag{5.43}$$

with

$$S_{Rz} = \begin{cases} P(1 + u/R)u_Z & \text{on } R = B \\ 0 & \text{on } R = A. \end{cases} \tag{5.44}$$

5.3 Finite element algorithm

To solve the nonlinear partial differential equations, the object-oriented package Libmesh [44] is used, which is a framework for solving and analyzing systems of nonlinear equations using the finite element method. It is also an interface to the high quality software PETSc, which is used to solve linear systems on both serial and parallel platforms.

5.3.1 Discretization

We discretize the governing PDEs (5.11) with the constraint (5.7) using the weighted residual-Galerkin method. The elastic domain is divided into a set of sub-domains. Libmesh offers the options of quadratic elements of 9-node quadrilateral and 6-node triangle type. Using a mixed interpolation approach, the displacement components u, w and the radial coordinate R are interpolated by quadratic shape functions N_i, while the Lagrange multiplier p is interpolated by linear shape functions L_i, i.e.

$$u = \sum_{k=1}^{n_1} N_k(\xi, \eta)u_k, \quad w = \sum_{k=1}^{n_1} N_k(\xi, \eta)w_k,$$

$$R = \sum_{k=1}^{n_1} N_k(\xi, \eta)R_k, \quad p = \sum_{k=1}^{n_2} L_k(\xi, \eta)p_k,$$

where n_1, n_2 are the element node numbers, which are dependent on the element type chosen, and ξ and η are natural coordinate variables, corresponding to isoparametric finite elements.

This allows us to write the discretized nonlinear governing equations as

$$\Re = \mathbf{K}(\mathbf{U})\mathbf{U} - \mathbf{F}(\mathbf{U}) = \mathbf{0}, \tag{5.45}$$

where $\mathbf{U}$ is the global vector of unknowns, $\mathbf{K}(\mathbf{U})$ is the global stiffness matrix, $\mathbf{F}(\mathbf{U})$ denotes the force vector, which is also dependent on $\mathbf{U}$, and $\Re$ is the global residual

vector, which should be $\mathbf{0}$ for an exact solution. Note that $\mathbf{U}$ was used earlier for the right stretch tensor, which does not appear hereon so there is no conflict of notation. Numerical simulations show that the 6-node triangle is more efficient than the 9-node quadrilateral element for large distortions. The formulation of the finite element matrices is problem dependent, as shown in Section 4.3 below.

5.3.2 Newton's method

To solve systems of nonlinear equations such as (5.45), the SNES library of PETSc [4] is called by Libmesh. The SNES library provides a powerful suite of numerical routines, and Newton-Krylov methods provide the core of the package, including line search and trust region techniques. Newton's iteration may be implemented by

$$\mathbf{U}_{r+1} = \mathbf{U}_r - \mathbf{J}^{-1}(\mathbf{U}_r)\Re(\mathbf{U}_r), \tag{5.46}$$

where r is the iteration number and $\mathbf{J}$ is the Jacobian matrix, which, by using (5.45), is defined by

$$\mathbf{J}(\mathbf{U}_r) = \frac{\partial \Re(\mathbf{U}_r)}{\partial \mathbf{U}} = \mathbf{K}(\mathbf{U}_r) + \frac{\partial \mathbf{K}(\mathbf{U}_r)}{\partial \mathbf{U}}\mathbf{U}_r - \frac{\partial \mathbf{F}(\mathbf{U}_r)}{\partial \mathbf{U}}. \tag{5.47}$$

Convergence is achieved when the relative residual tolerance $||\Re(\mathbf{U}_r)||/||\Re(\mathbf{U}_0)||$ (in the l_2 norm) is less than 10^{-8} or the absolute tolerance $||\Re(\mathbf{U}_r)||$ is less than 10^{-12}, where $\Re(\mathbf{U}_0)$ is the initial residual.

5.3.3 Detailed discretizing integrations

Radially symmetric case

Applying Galerkin's method to equation (5.20), we obtain

$$\int_\Omega N_i S_{Rr,R}\mathrm{d}\Omega + \int_\Omega N_i \frac{1}{R}(S_{Rr} - S_{\Theta\theta})\mathrm{d}\Omega = 0, \tag{5.48}$$

where Ω is the integration domain. The domain of integration Ω is the physical domain in the reference configuration corresponding to the (R, Z) tube section. For each element, (5.48) can be integrated by parts to give

$$-\sum_{j=1}^{n_1}\int_R\int_Z(\frac{1}{R}N_iN_j + RN_{i,R}N_{j,R})\mathrm{d}R\mathrm{d}Zu_j$$

$$+\sum_{j=1}^{n_2}\int_R\int_Z L_j[(1 + \sum_{k=1}^{n_1}N_{k,R}u_k)N_i + (R + \sum_{k=1}^{n_1}N_ku_k)N_{i,R}]\mathrm{d}R\mathrm{d}Zp_j$$

$$= -\int_Z(RN_iS_{Rr})|_{R_1}^{R_2}\mathrm{d}Z + \int_R\int_Z(N_i + RN_{i,R})\mathrm{d}R\mathrm{d}Z. \tag{5.49}$$

Equation (5.22) may be discretized similarly to give

$$\sum_{j=1}^{n_1} \int_R \int_Z RL_i[N_j + (R + \sum_{k=1}^{n_1} N_k u_k)N_{j,R}]\mathrm{d}R\mathrm{d}Z u_j = 0. \tag{5.50}$$

Here we have adopted 9-node quadrilateral elements in order to achieve better accuracy, so that $n_1 = 9, n_2 = 4$. Note that when assembled globally the boundary integrals in (5.49) cancel out except at the boundaries of the tube.

The linear case

The discretized equations for the linear case can be obtained by using a similar procedure to that used for the radially symmetric case. This yields

$$\sum_{j=1}^{n_1} \int_r \int_z \mu r(2N_{i,r}N_{j,r} + N_{i,z}N_{j,z}) + 2\frac{\mu}{r}N_i N_j \mathrm{d}r\mathrm{d}z u_j + \sum_{j=1}^{n_1} \int_r \int_z \mu r N_{i,z}N_{j,r}\mathrm{d}r\mathrm{d}z w_j$$

$$-\sum_{j=1}^{n_2} \int_r \int_z (rN_{i,r} + N_i)L_j\mathrm{d}r\mathrm{d}z p_j = \int_z (rN_i\sigma_{rr})|_{r_1}^{r_2}\mathrm{d}z + \int_r r(N_i\sigma_{zr})|_{z_1}^{z_2}\mathrm{d}r \tag{5.51}$$

$$\sum_{j=1}^{n_1} \int_r \int_z \mu r N_{i,r}N_{j,z}\mathrm{d}r\mathrm{d}z u_j + \sum_{j=1}^{n_1} \int_r \int_z \mu r(N_{i,r}N_{j,r} + 2N_{i,z}N_{j,z})\mathrm{d}r\mathrm{d}z w_j$$

$$-\sum_{j=1}^{n_2} \int_r \int_z rN_{i,z}L_j\mathrm{d}r\mathrm{d}z p_j = \int_z (rN_i\sigma_{rz})|_{r_1}^{r_2}\mathrm{d}z + \int_r r(N_i\sigma_{zz})|_{z_1}^{z_2}\mathrm{d}r, \tag{5.52}$$

$$\sum_{j=1}^{n_1} \int_r \int_z rL_i(N_{j,r} + \frac{1}{r}N_j)\mathrm{d}r\mathrm{d}z u_j + \sum_{j=1}^{n_1} \int_r \int_z rL_i N_{j,z}\mathrm{d}r\mathrm{d}z w_j = 0. \tag{5.53}$$

For the linear case, the 6-node triangle is used, so that $n_1 = 6, n_2 = 3$. This is also used for the following nonlinear case since for large distortions the triangular element shows its superiority over the rectangular element.

The nonlinear case

On applying Galerkin's method to equations (5.40)–(5.42) and integrating by parts, we obtain the stiffness matrix, which can be written in many different ways since the dependent variables are nonlinearly coupled in each of the terms of the stiffness matrix. In general, in the nonlinear case we obtain the discretization by separating off the terms that also appear in the radially-symmetric and linear cases so that the final equations in the nonlinear case can be taken as the corresponding linear ones multiplied by some complicated

higher order coefficients. The final forms of the discretized equilibrium equations and the incompressibility condition are

$$
\begin{aligned}
&\sum_{j=1}^{n_1} \int_R \int_Z \frac{\mu}{R} N_i N_j + R N_{i,R} \left\{ \left[\frac{(1+\cos 2\psi)t_1}{2\lambda_1} + \frac{(1-\cos 2\psi)t_3}{2\lambda_3} \right] N_{j,R} + \frac{1}{2} \sin 2\psi (\frac{t_1}{\lambda_1} - \frac{t_3}{\lambda_3}) N_{j,Z} \right\} \\
&+ R N_{i,Z} \left\{ \frac{1}{2} \sin 2\psi (\frac{t_1}{\lambda_1} - \frac{t_3}{\lambda_3}) N_{j,R} + \left[\frac{(1-\cos 2\psi)t_1}{2\lambda_1} + \frac{(1+\cos 2\psi)t_3}{2\lambda_3} \right] N_{j,Z} \right\} \mathrm{d}R\mathrm{d}Z u_j \\
&- \sum_{j=1}^{n_2} \int_R \int_Z R \left[\frac{1}{R+u} N_i + \frac{1+\cos 2\psi}{2} \lambda_1^{-2} N_{i,R} \right] L_j \mathrm{d}R\mathrm{d}Z p_j = - \int_R \int_Z \mu N_i \mathrm{d}R\mathrm{d}Z \qquad (5.54) \\
&- \int_R \int_Z R N_{i,R} \left[\mu \frac{1+\cos 2\psi}{2} + \frac{(1-\cos 2\psi)t_3}{2\lambda_3} \right] \mathrm{d}R\mathrm{d}Z - \int_R \int_Z \frac{1}{2} R N_{i,Z} \sin 2\psi (\frac{t_1}{\lambda_1} - \frac{t_3}{\lambda_3}) \mathrm{d}R\mathrm{d}Z \\
&+ \int_Z (R N_i S_{Rr})|_{R_1}^{R_2} \mathrm{d}Z + \int_R R (N_i S_{Zr})|_{Z_1}^{Z_2} \mathrm{d}R,
\end{aligned}
$$

$$
\begin{aligned}
&\sum_{j=1}^{n_1} \int_R \int_Z R N_{i,R} \left\{ \left[\frac{(1+\cos 2\psi)t_1}{2\lambda_1} + \frac{(1-\cos 2\psi)t_3}{2\lambda_3} \right] N_{j,R} + \frac{1}{2} \sin 2\psi (\frac{t_1}{\lambda_1} - \frac{t_3}{\lambda_3}) N_{j,Z} \right\} \\
&+ R N_{i,Z} \left\{ \frac{1}{2} \sin 2\psi (\frac{t_1}{\lambda_1} - \frac{t_3}{\lambda_3}) N_{j,R} + \left[\frac{(1-\cos 2\psi)t_1}{2\lambda_1} + \frac{(1+\cos 2\psi)t_3}{2\lambda_3} \right] N_{j,Z} \right\} \mathrm{d}R\mathrm{d}Z w_j \\
&- \sum_{j=1}^{n_2} \int_R \int_Z R \frac{1+\cos 2\psi}{2} \lambda_3^{-2} N_{i,Z} L_j \mathrm{d}R\mathrm{d}Z p_j = - \int_R \int_Z R N_{i,R} \frac{1}{2} \sin 2\psi (\frac{t_1}{\lambda_1} - \frac{t_3}{\lambda_3}) \mathrm{d}R\mathrm{d}Z \qquad (5.55) \\
&- \int_R \int_Z R N_{i,Z} \left[\frac{(1-\cos 2\psi)t_1}{2\lambda_1} + \mu \frac{1+\cos 2\psi}{2} \right] \mathrm{d}R\mathrm{d}Z + \int_Z (R N_i S_{Rz})|_{R_1}^{R_2} \mathrm{d}Z + \int_R R (N_i S_{Zz})|_{Z_1}^{Z_2} \mathrm{d}R,
\end{aligned}
$$

$$
\begin{aligned}
&\sum_{j=1}^{n_1} \int_R \int_Z R L_i \left(\frac{1}{R+u} N_j + N_{j,R} \right) \mathrm{d}R\mathrm{d}Z u_j \\
&+ \sum_{j=1}^{n_1} \int_R \int_Z R L_i \left[(1+u_R) N_{j,Z} - u_Z N_{j,R} \right] \mathrm{d}R\mathrm{d}Z w_j = 0. \qquad (5.56)
\end{aligned}
$$

Using equations (5.54)–(5.56), we obtain the stiffness matrix $\mathbf{K}$. It is worth mentioning that in order to achieve convergence of the solutions $\mathbf{J}$ needs to be computed analytically from (5.47). Although a much simpler approach to estimating the true Jacobian matrix $\mathbf{J}$ is commonly used by using the stiffness matrix $\mathbf{K}$ this does not work for our nonlinear model. This indicates that the second and third terms in the expression (5.47) are important and cannot be neglected.

5.4 Numerical algorithms

The work for the numerical processes are summarized as follows:

1. write the file `mesh.xda` for symmetric mesh generation.

2. write the main programme to call the linear/nonlinear solvers to solve the equation systems by applying the external pressure as a sequence of increments.

3. write the subfunction `void compute_jacobian` to evaluate the true global Jacobian matrix **J**.

4. write the subfunction `void compute_residual` to evaluate the global residual vector $\Re$.

5. write the subfunction `struct stress_vector cauchy_stress` to evaluate the stresses and principal stresses.

6. write the subfunction `std::vector<Real>& stretch` to evaluate the principal stretches.

The algorithms for nonlinear case including the main programme and a sub-programme for constructing the global Jacobian matrix **J** are presented by the flowcharts as follows. The algorithms for the main programme are illustrated in Figs. 5.3–5.5 and the algorithms for constructing the global Jacobian matrix are shown in Figs. 5.6–5.10. We don't provide the algorithms for the radially symmetric and linear case since they are similar and simpler than those for the nonlinear case.

5.5 Numerical results

To demonstrate the differences between the nonlinear and linear cases, three options will be considered for the tube geometry: thick-walled short tubes with $A/B = 0.5$ and $L/B = 1$, thick-walled longer tubes with $A/B = 0.5$ and $L/B = 5$, and thin-walled longer tubes with $A/B = 0.8$ and $L/B = 5$.

Henceforth, all the variables are used in dimensionless form, but without change of notation. The radial coordinates R and r and the displacement components u and w are non-dimensionalized with B; the axial coordinates Z and z with L; the pressure P and the stress components σ_{ij} with the shear modulus μ.

5.5.1 Thick-walled short tubes: $A/B = 0.5$ and $L/B = 1$

Displacements and stretches

As both the linear and nonlinear models should agree when deformation is small, to validate the numerical approach, a comparison of the nonlinear and linear models for
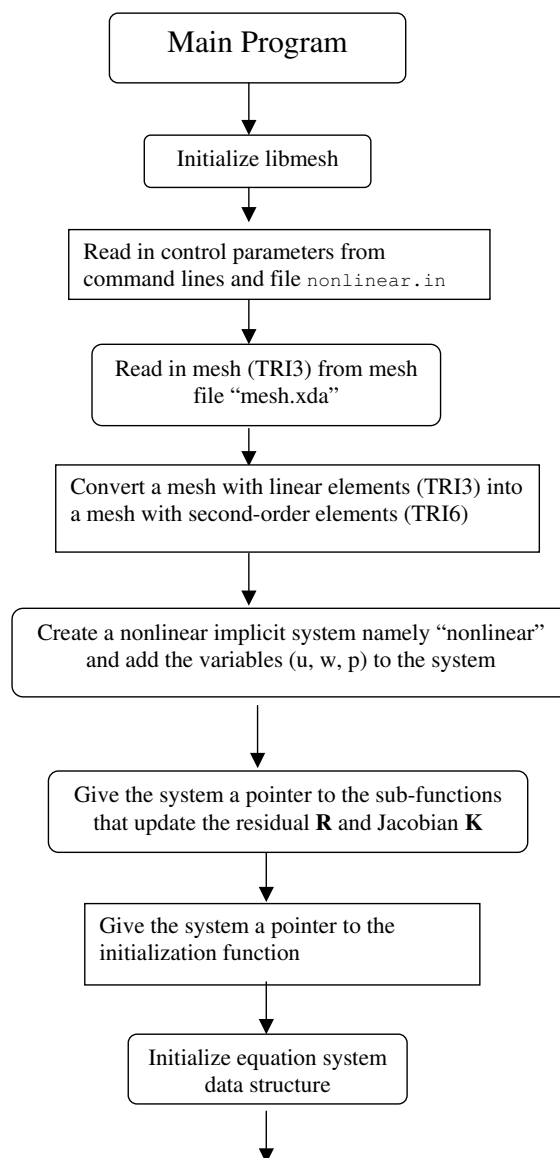
Figure 5.3: Flowchart for for nonlinear case, part 1.
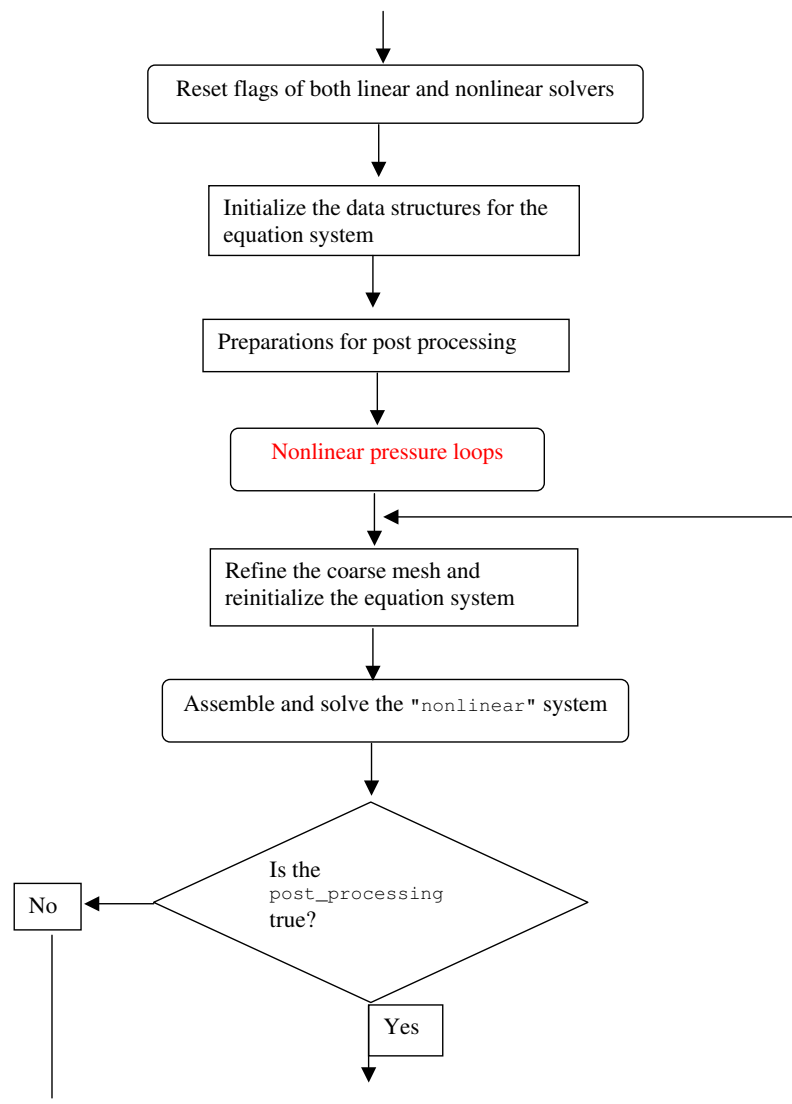
Figure 5.4: Flowchart for for nonlinear case, part 2.
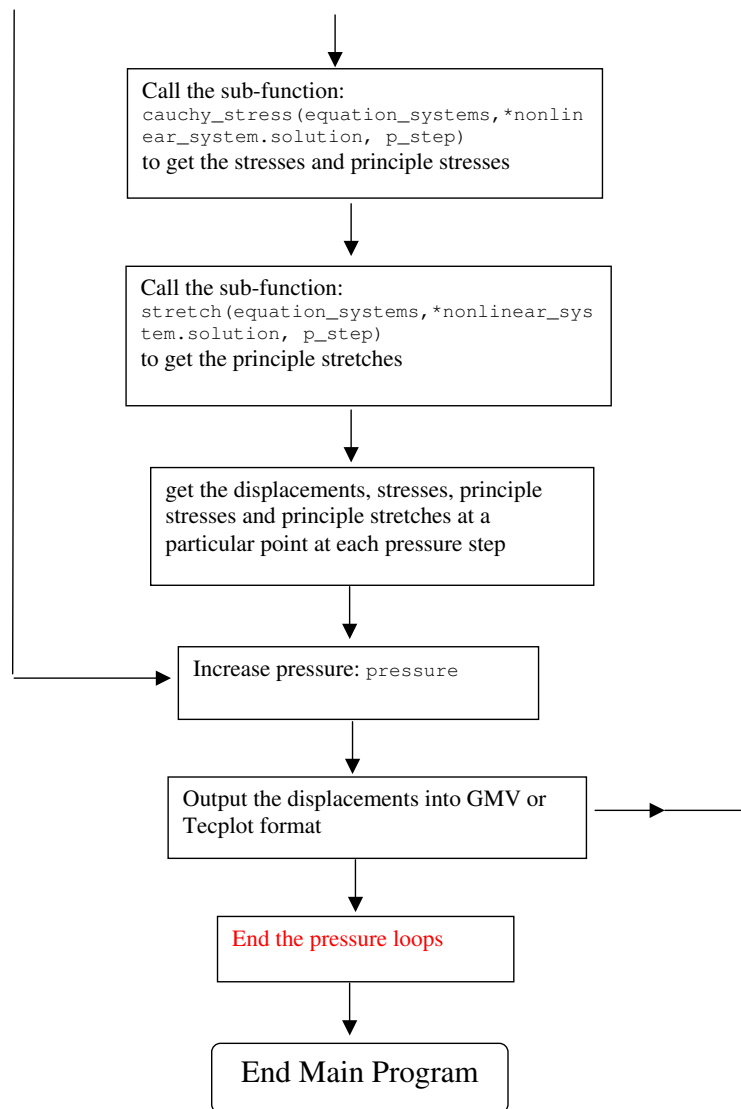
Figure 5.5: Flowchart for for nonlinear case, part 3.
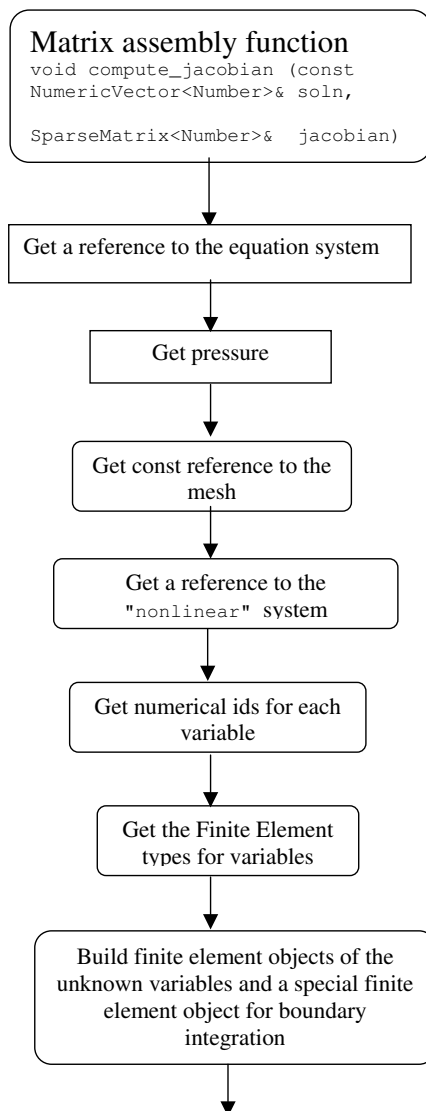
Figure 5.6: Flowchart for the Global stiffness matrix, part 1.

Define the Gauss quadrature rule

Define Jacobian*quadrature weight :`JxW`, element shape functions and shape function gradients.

Define the data structures to contain element matrices

Define vectors to contain the DOF for the element and variables

Loop over all the elements in the mesh.
(This involves compute element matrix and right-hand-side contribution.)

Fill the DOF vectors with global degree of freedom indices for the element.

Figure 5.7: Flowchart for the Global stiffness matrix, part 2.
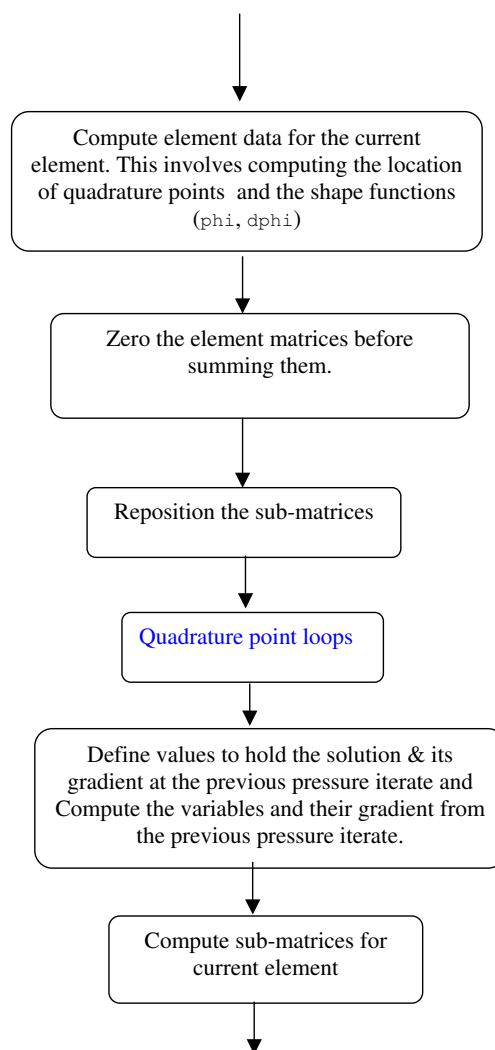
Figure 5.8: Flowchart for the Global stiffness matrix, part 3.
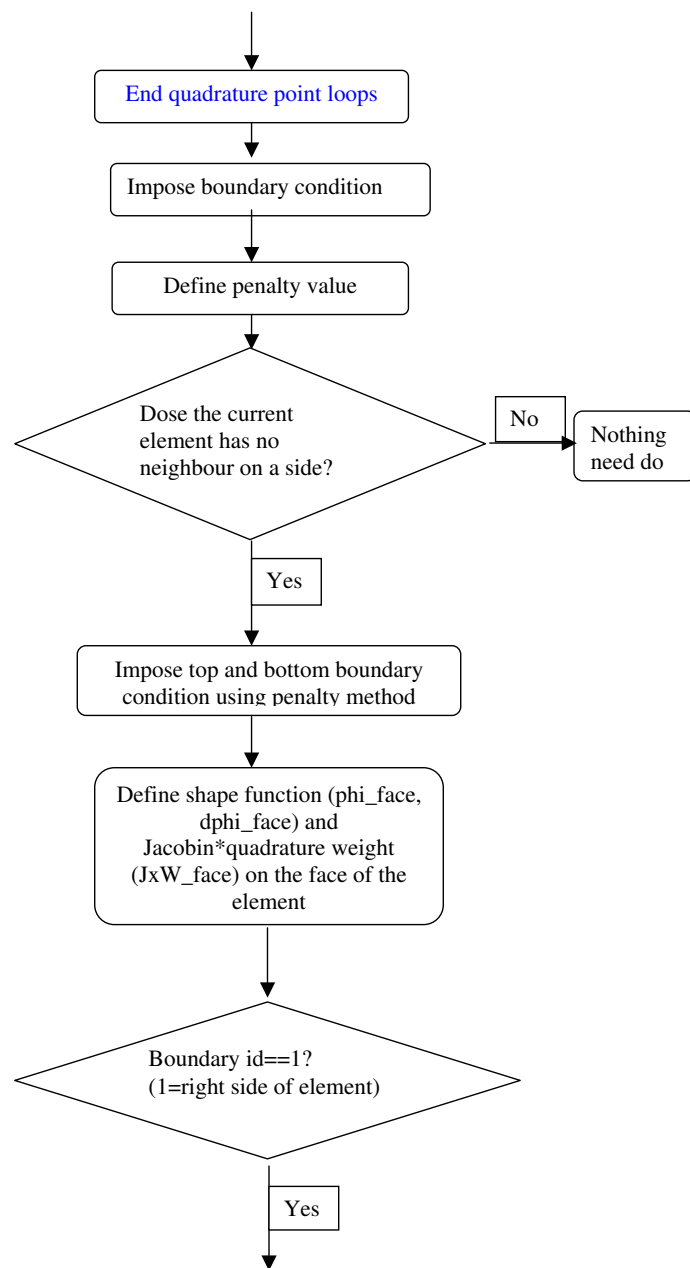
Figure 5.9: Flowchart for the Global stiffness matrix, part 4.
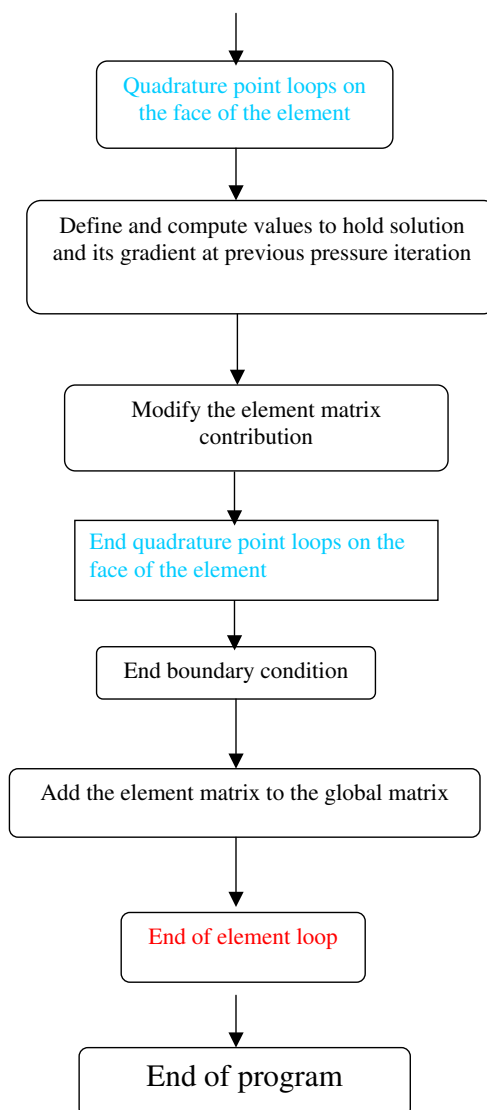
Figure 5.10: Flowchart for the Global stiffness matrix, part 5.

small pressure ($P = 0.05$) has been made, as shown in Fig. 5.11, in which contour plots of the values of u and w for each case are illustrated, superimposed on the deformed (r, z) section [1] of the tube. As expected, the distributions of the displacement components u and w for these two cases are virtually indistinguishable. However, the difference between the nonlinear and linear models increases as the pressure increases. This is highlighted in Fig. 5.12(a), where the displacement u in the radial direction versus the external loading P at point $(R, Z) = (0.5, 0.5)$ is shown.

Figure 5.12(a) shows that the linear theory overestimates the displacement u, especially for large external pressure ($P \gtrsim 1.5$). For example, for $P = 2$, the predictions of u for the linear and nonlinear cases are 0.416 and 0.291, respectively, an overestimate of 43%. Further validation of our numerical code can be made by comparing the analytical and numerical solutions for the radially-symmetric case shown in Fig. 5.12(a). The curves are indistinguishable in this figure. Note that the radially-symmetric and nonlinear curves intersect at $P \approx 1.15$. For $P \gtrsim 1.15$, u increases with P more slowly for the radially-symmetric case than for the nonlinear one, thus significantly underestimating the displacement in the radial direction. The linear theory predicts a smaller axial displacement w than the nonlinear theory, while for the radially-symmetric case $w = 0$; see Fig. 5.12(b). The differences in the results for the considered point are representative of those seen at other points, details for which are not shown here.

The deformation, as distinct from the displacement, can be characterized in terms of the stretches, and this is illustrated in Fig. 5.13, which shows how the principal stretches at the point $R = 0.5, Z = 0.5$ vary with the pressure P. It can be seen that at this point $\lambda_1 > \lambda_3 > 1$ and $\lambda_2 < 1$. Again, for smaller pressure ($P \lesssim 0.4$), the principal stretches are almost the same for the linear and nonlinear cases. It is clear, and of course not surprising, that the linear theory provides an accurate prediction only for small deformations, corresponding to the maximum principal stretch λ_1 less than about 1.1. However, as we shall see in the next section, the linear–nonlinear correspondence reduces to λ_1 less that about 1.05, i.e. to a strain of about 5%, when the stress components are considered. As the pressure increases the nonlinear theory predicts larger values of λ_1, λ_2 and λ_3 than the linear theory. It should be remarked that the incompressibility condition $\lambda_1\lambda_2\lambda_3 = 1$ is violated for the principal stretches calculated for the linear theory except for very small values of P. This just emphasizes that the linear theory cannot be expected to be valid except for small

---

[1]Note that the displacements u and w are too small to be seen in Fig. 5.11.

(a)

(b)
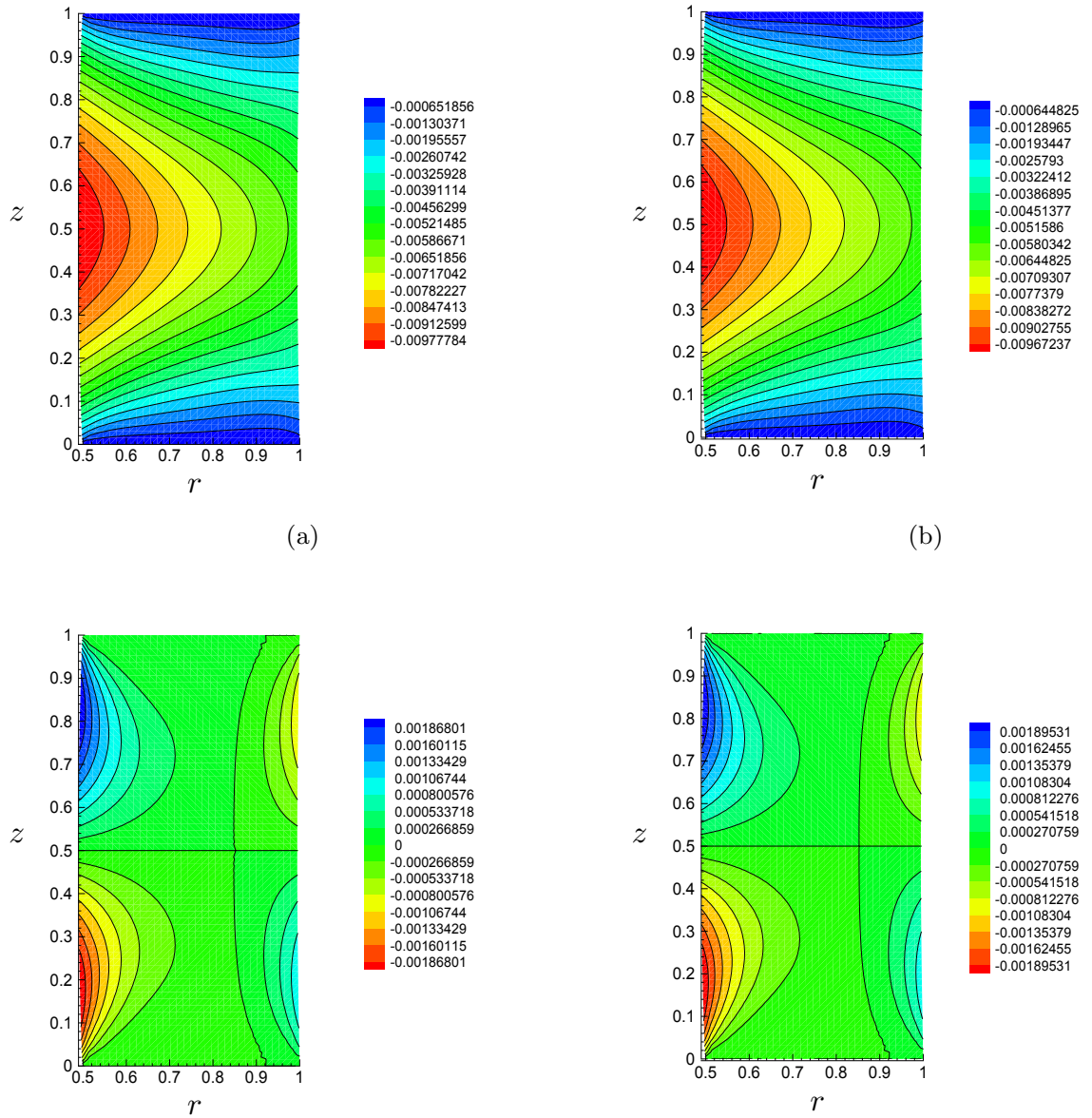
Figure 5.11: Deformed profiles of the tube section in (r, z) space for a tube with $A/B = 0.5, L/B = 1$ subject to external pressure $P = 0.05$ with the displacement distributions u and w superimposed: (a) linear u; (b) nonlinear u; (c) linear w; (d) nonlinear w. The plots correspond to $R \in [0.5, 1], Z \in [0, 1]$.

pressures and the accompanying small deformations.

To better understand the effect of the nonlinear contributions in equations (5.40)–(5.42), the displacement distributions are plotted for a relatively large value 2.3 of the pressure P in Fig. 5.14. For the purpose of comparison, the corresponding linear results are also shown. Some significant differences between the linear and nonlinear models can be observed in Fig. 5.14. The displacement in the radial direction is so large in the linear
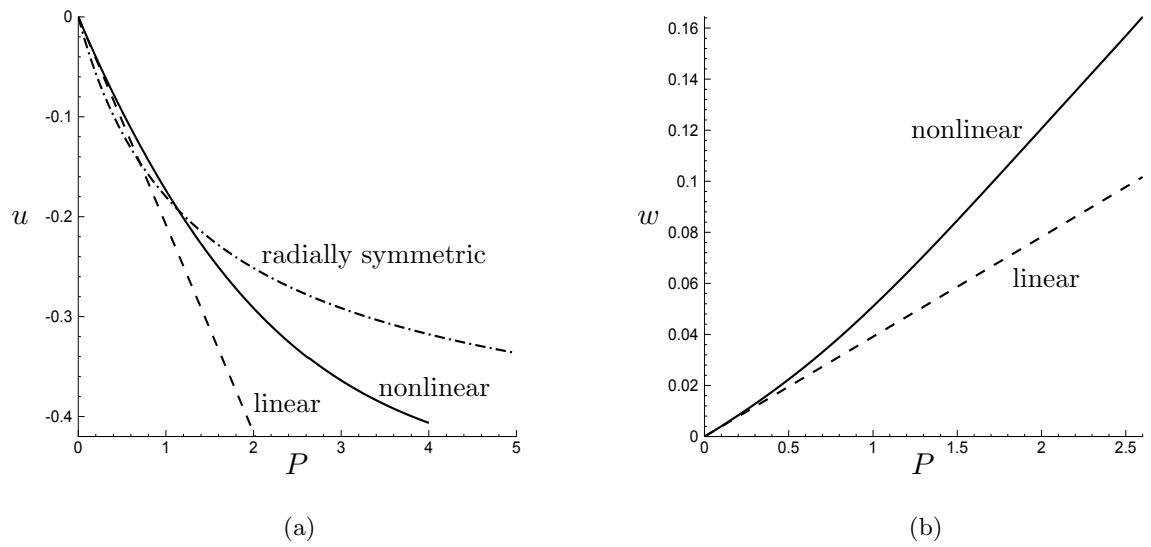
Figure 5.12: Plots of displacement against pressure for a tube with $A/B = 0.5, L/B = 1$ at specific points: (a) u versus P at point $(R, Z) = (0.5, 0.5)$; radially symmetric (dash-dotted curve); linear (dashed line); nonlinear (solid curve): (b) w versus P at point $(R, Z) = (0.5, 0.75)$; linear (dashed line); nonlinear (solid curve).
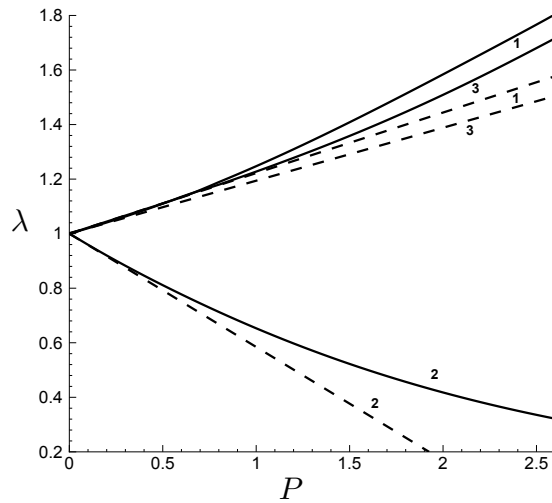
Figure 5.13: Plots of λ_1, λ_2 and λ_3 (labelled $1, 2, 3$, respectively) versus P calculated at the point $(R, Z) = (0.5, 0.5)$ for a tube with $A/B = 0.5, L/B = 1$: linear (dashed lines); nonlinear (solid curves).

case that the middle section of the tube almost comes into self contact on the axis $R = 0$. For the nonlinear case, the most striking feature is the bulging out at the corners, which is barely visible in the linear case. This causes the displacement pattern and magnitude to change. The radial displacement u changes between -0.47 and 0 in the linear case, and between -0.31 and 0.0145 in nonlinear case. The axial displacement w has the range -0.095 to 0.095 (linear case) and -0.15 to 0.15 (nonlinear case). This is consistent with the corner bulging at $R = 0.5$ on the ends of the tube, which stretches the tube section in two opposite axial directions.
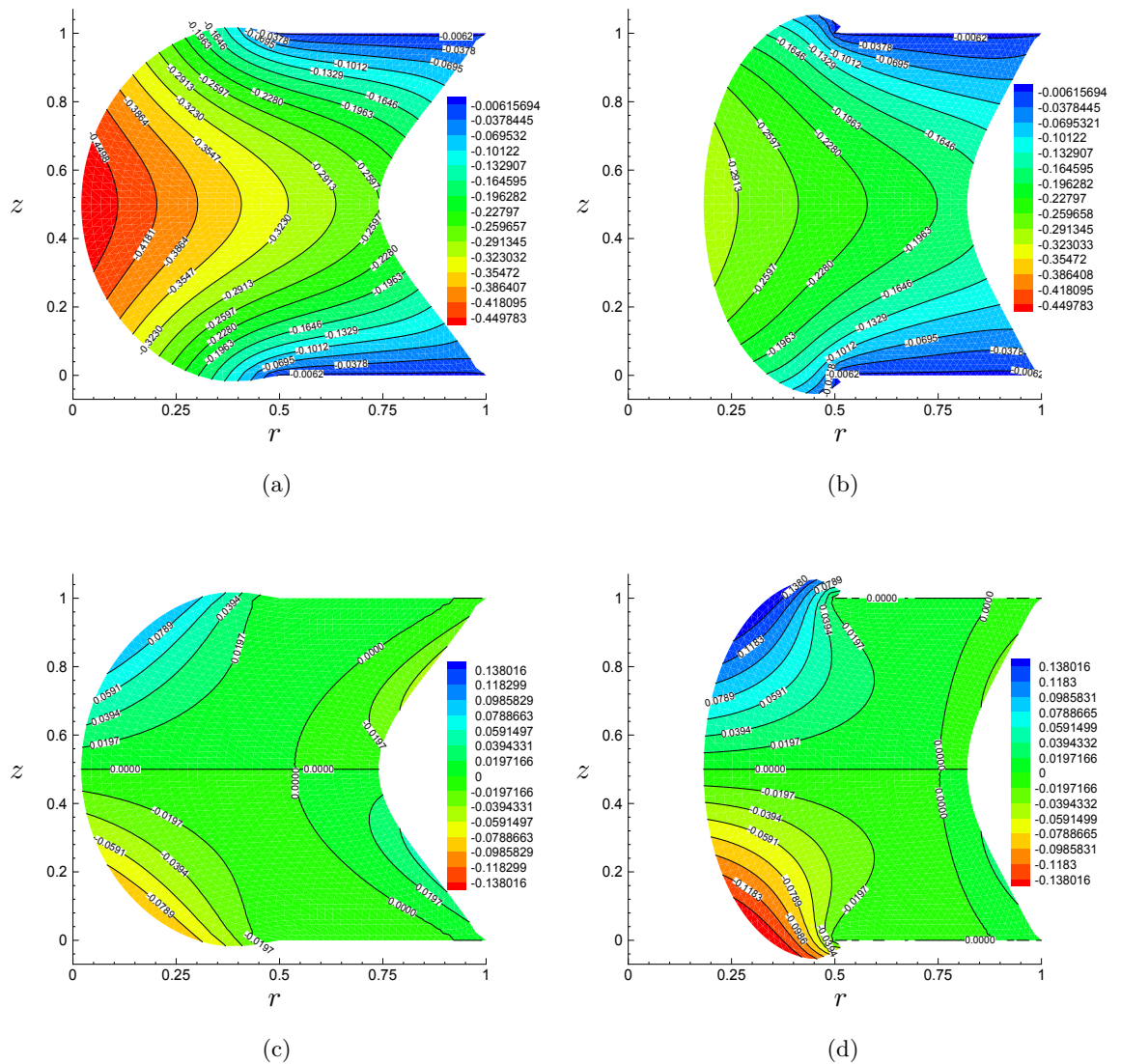
Figure 5.14: Deformed profiles of the tube section in (r, z) space for a tube with $A/B = 0.5, L/B = 1$ subject to external pressure $P = 2.3$, with distributions of the displacement components superimposed: (a) linear u; (b) nonlinear u; (c) linear w; (d) nonlinear w.

Cauchy stresses

The stress distributions for the linear and nonlinear cases are again almost the same for very small external pressure, but as expected they depart significantly for large pressures. Figures 5.15 and 5.16 show the distributions of components of Cauchy stress for $P = 2.3$ for the linear and nonlinear cases, respectively. Negative values of the stresses are shown with dashed curves. In all cases, the normal stress distributions in the upper half section have mirror symmetry with the lower half, while the distribution of shear stress is anti-symmetric.
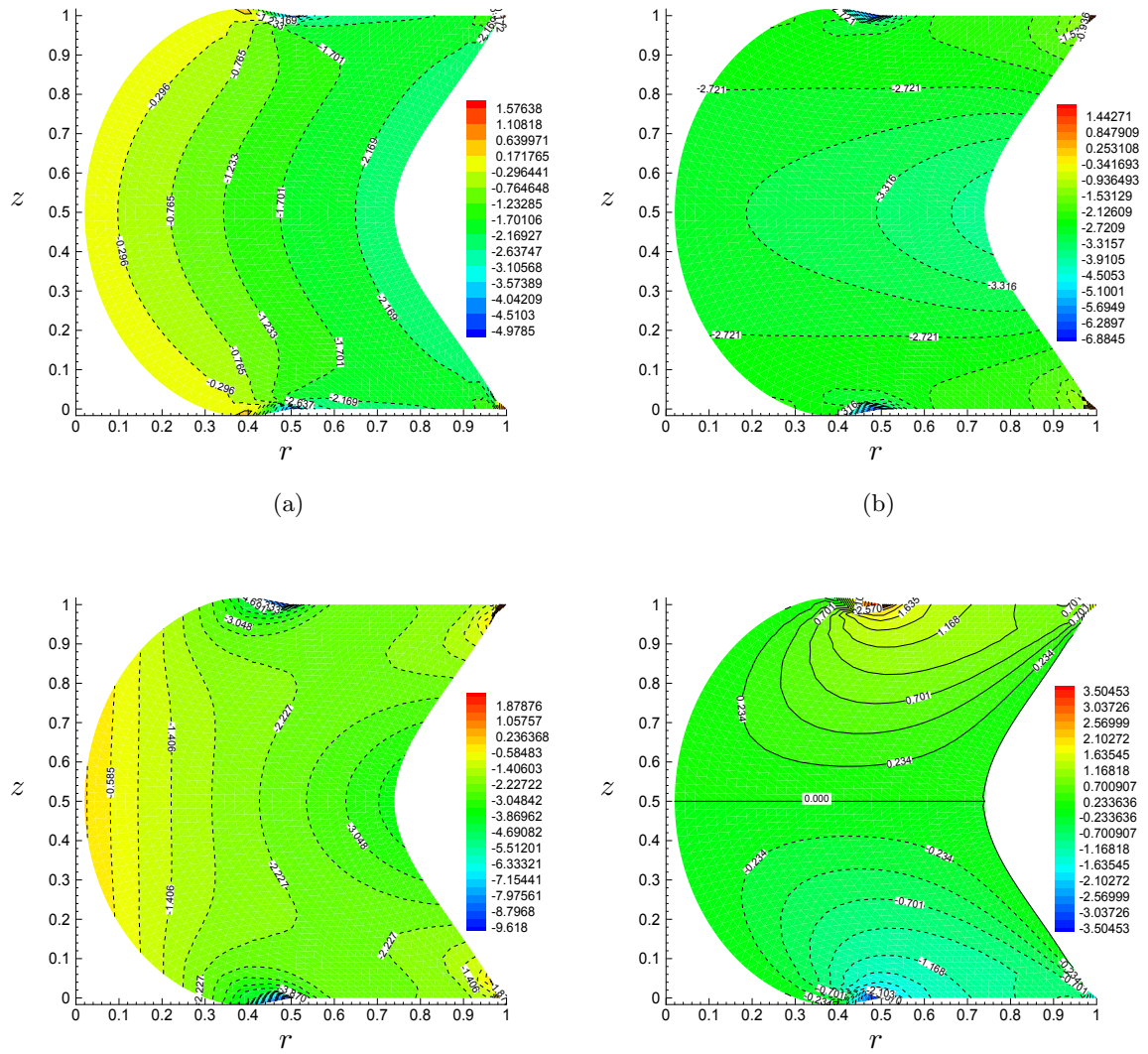
Figure 5.15: Deformed profiles of the tube section in (r, z) space for a tube with $A/B = 0.5, L/B = 1$ subject to external pressure $P = 2.3$, with distributions of the Cauchy stress components superimposed. Linear case with positive contours (solid), negative contours (dashed): (a) σ_{11}, (b) σ_{22}, (c) σ_{33}, (d) σ_{13}.

(a)

(b)

(c)

(d)
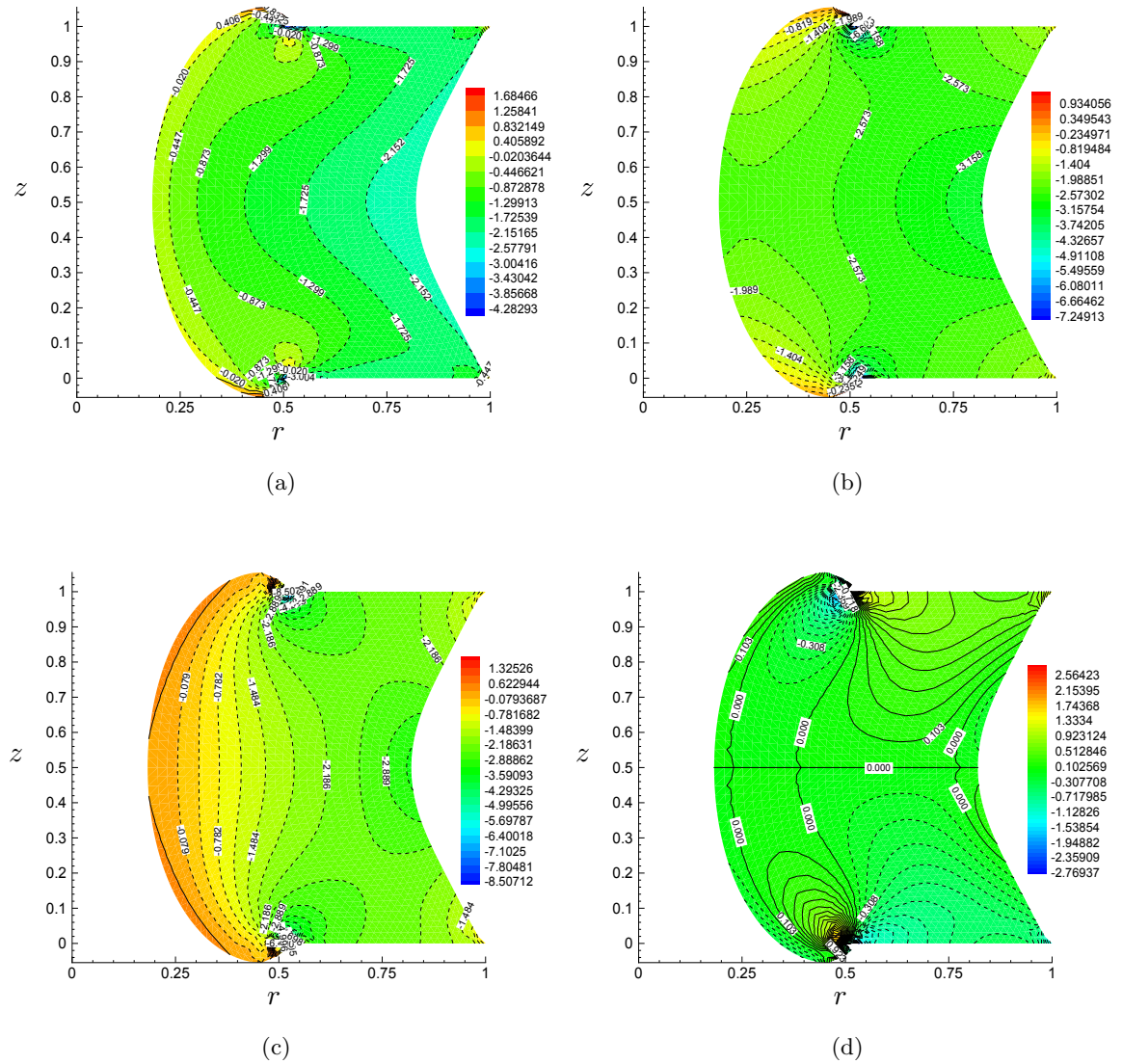
Figure 5.16: Deformed profiles of the tube section in (r, z) space for a tube with $A/B = 0.5, L/B = 1$ subject to external pressure $P = 2.3$, with distributions of the Cauchy stress components superimposed. Nonlinear case with positive contours (solid), negative contours (dashed): (a) σ_{11}, (b) σ_{22}, (c) σ_{33}, (d) σ_{13}.

It can be seen from Fig. 5.15 and Fig. 5.16 that in both the linear and nonlinear cases, the areas of stress concentration are located at the four corners. However, for the linear case, the normal stresses $\sigma_{11}, \sigma_{22}, \sigma_{33}$ are mostly negative, with the peak negative stresses occurring at the two inner corners. The peak positive stresses are at the two outer corners, and in the radial direction (i.e. for σ_{11}). On the inner surface the stress σ_{11} is positive only near the ends. This shows that most of the section is under compression when subject to an external pressure. For the nonlinear case, on the other hand, all the peak stresses

(positive and negative) occur at the inner corners. This is directly due to the fact that the inner corners are significantly squeezed out, which causes both significant compression and tension there. The shear stress distribution σ_{13} is most interesting; for the linear case, σ_{13} is entirely positive in the upper half and entirely negative in the lower half, with the zero stress line at $Z = 0.5$. However, in the nonlinear case, because of the corner bulging, each half section is divided into four zones between which the shear stress changes sign. In the upper half, the innermost section is sheared upwards, while different parts of the outermost section are subject to either positive or negative shear stress. The opposite is true in the lower half. The general trend for short tubes is that the magnitudes of the stresses in the nonlinear case are smaller than the corresponding linear magnitudes, with σ_{11} between -4.7 and 2.11, σ_{22} between -7.54 and 1.52, σ_{33} between -8.86 and 2.02, and σ_{13} between -2.87 and 2.87. These are to be compared with the linear case: σ_{11} from -5.44 to 2.04, σ_{22} from -7.18 to 2.03, σ_{33} from -10 to 2.69, and σ_{13} from -3.74 to 3.74.

To show how the stresses change with the external pressure at a particular location, we plot the variation of the stress components σ_{ij} with the pressure at point ($R = 0.75, Z = 0.75$) in Fig. 5.17. Again, the differences between the results for the linear and nonlinear models are small if P is small enough, in this case $P \lesssim 0.5$ for the normal stress components and $P \lesssim 0.3$ for σ_{13}. However, significant differences are found between the linear and nonlinear predictions as P increases, especially in the stress components σ_{11} and σ_{13}. The nonlinear model exhibits much smaller stress magnitudes for the same applied pressure. It is interesting that σ_{13} first increases rapidly with P, but reaches a maximum around $P = 1.8$ and then decreases with further increase in P, as shown in Fig. 5.17(b). This is because as the pressure increases beyond a certain level, the corners bulge out more and more and the second left (negative) shear zone in Fig. 5.16(d) increases in size, while the third (positive) shear zone (where the point is located) shrinks. As a result, the positive shear stress at this point decreases for $P \gtrsim 1.8$.

To illustrate the response of the material locally to the external forces, plots of principal stress versus principal stretch are shown in Fig. 5.18 for the point ($R = 0.75, Z = 0.75$). We note that $\lambda_1 > 1$, $\lambda_2 < 1$ and $\lambda_3 < 1$ at the point in question. Compared with the linear results, the nonlinear model predicts larger magnitudes of the principal stresses for the same principal stretches. This means the stiffness of the material at this special point becomes larger. Note that as P increases the relationship between the principal stress σ_3 and the stretch λ_3 loses monotonicity. It is also noted that at the point ($R = 0.75, Z =$
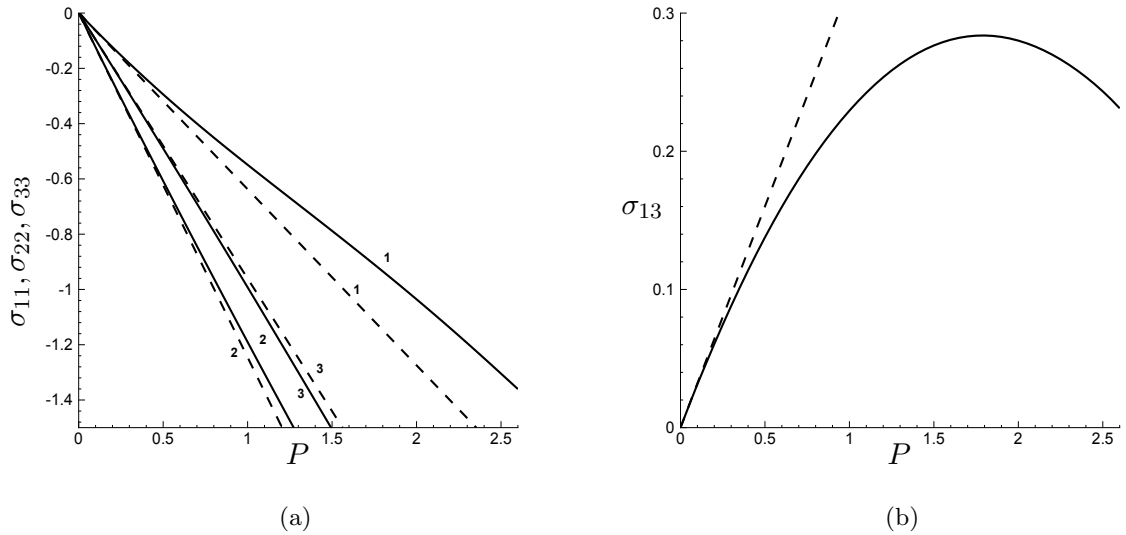
Figure 5.17: (a) Plots of $\sigma_{11}, \sigma_{22}, \sigma_{33}$ (labelled as $1, 2, 3$, respectively) versus P for a tube with $A/B = 0.5, L/B = 1$ at point $(R, Z) = (0.75, 0.75)$. (b) Plots of σ_{13} versus P. Linear (dashed lines); nonlinear (solid curves).

0.75), the angle ψ which defines the principal directions has the constant value $31.6°$ for the linear case, while it varies in the range $29.8° < \psi < 32.6°$ for the nonlinear case.
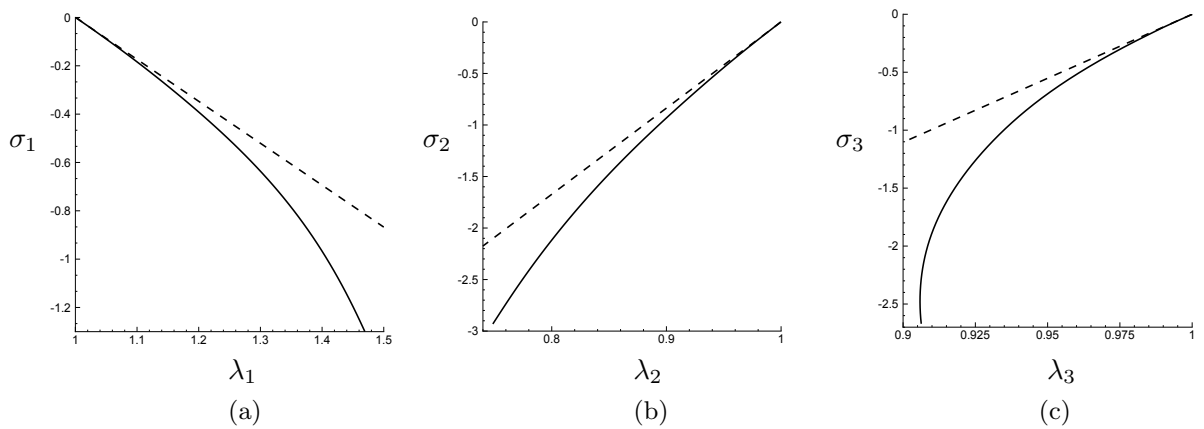
Figure 5.18: Plots of the principal stresses versus the corresponding principal stretches for a tube with $A/B = 0.5, L/B = 1$ at the point $(R, Z) = (0.75, 0.75)$: (a) σ_1 vs λ_1; (b) σ_2 vs λ_2; (c) σ_3 vs λ_3. Linear results (dashed lines); nonlinear results (solid curves).

5.5.2 Thick-walled longer tubes: $A/B = 0.5$ and $L/B = 5$

Next, we consider a tube with the same thickness but five times longer. In this case we find that the u and w versus P curves are similar to those for the shorter tube observed

above. The only difference is that for both the linear and nonlinear cases the deformations of longer tubes tend to have two humps instead of one, as suggested in Fig. 5.19, i.e. the longer tube favours mode-2 deformations for the range of the pressure applied, while mode-1 is preferred for the shorter tubes. Figure 5.20 shows that the differences in the stress–pressure plots between the linear and nonlinear cases are smaller than for shorter tubes. However, the change in σ_{13} for the nonlinear case is interesting. As in Fig. 5.17(b), it follows the linear curve for small P but the range of values of P for which σ_{13} is positive is much smaller in this case, and it bends downwards sharply as soon as P exceeds about 0.1.
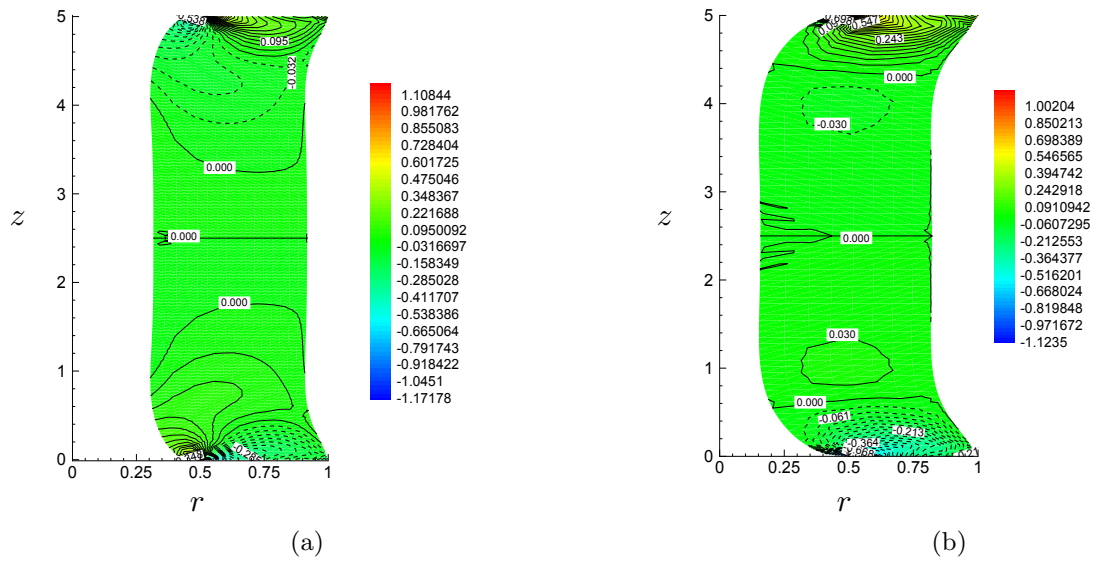
Figure 5.19: Distributions of the shear stress σ_{13} for a tube with $A/B = 0.5, L/B = 5$ at pressure $P = 1.01$, superimposed on the deformed profile of tube section in (r, z) space: positive values are indicated by solid contours and negative values by dashed contours. (a) nonlinear (b) linear.

The corresponding principal stress–stretch plots are shown in Fig. 5.21. The features of Fig. 5.21(a, b) are similar to those for the shorter tube. However, an interesting change in the σ_3–λ_3 plot is shown in Fig. 5.21(c), where an S-shaped curve is observed. This is associated with the complicated pattern of change in the shear zones shown in Fig. 5.19(a). The nonlinear tube tends to bulge at the two inner corners, which, when combined with the mode-2 humps, creates a much larger negative shear zone in the upper half of the cylinder. The smaller bulge at the corners also causes the shear stress to be split into negative and positive regions within each half cylinder, and the negative regions emerge
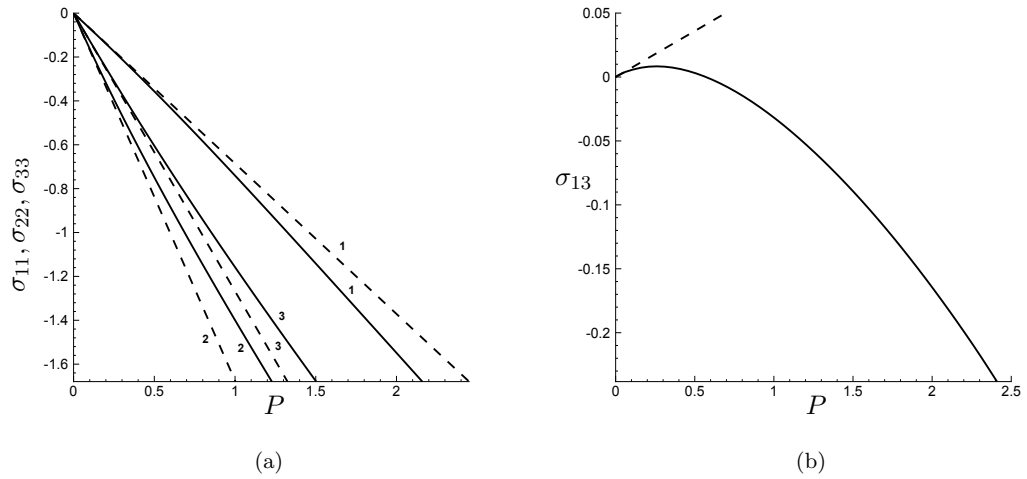
Figure 5.20: (a) Plots of $\sigma_{11}, \sigma_{22}, \sigma_{33}$ (labelled $1, 2, 3$, respectively) versus P for a tube with $A/B = 0.5, L/B = 5$ at point $(R, Z) = (0.75, 4.5)$. (b) Plots of σ_{13} versus P. Linear (dashed lines); nonlinear (solid curves).
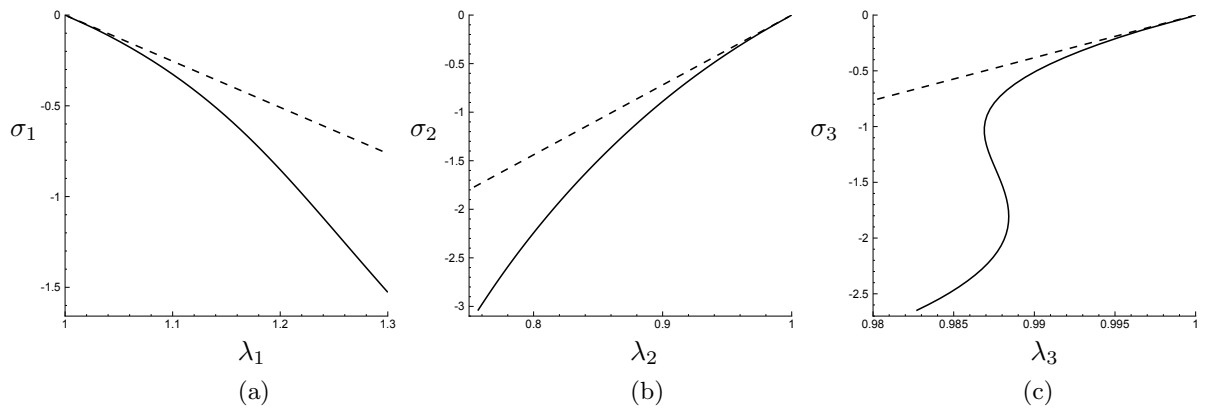
Figure 5.21: Plots of the principal stresses versus the corresponding principal stretches for a tube with $A/B = 0.5, L/B = 5$, at the point $(R, Z) = (0.75, 4.5)$: nonlinear case. (a) σ_1 vs λ_1, (b) σ_2 vs λ_2, (c) σ_3 vs λ_3.

and expand as the external pressure increases. The linear case shown in Fig. 5.19(b) fails to predict the bulging at the corners at all for this case, as a result of which there is no shear splitting zone towards the ends, although the shear zone adjacent to the boundary region changes its sign, presumably due to the mode-2 deformation.

5.5.3 Thinner and longer tubes: $A/B = 0.8$ and $L/B = 5$

For longer and thinner tubes with $A/B = 0.8$ and $L/B = 5$, the most interesting feature is the occurrence of higher modes (multiple humps in the deformation) in the nonlinear case. Four modes from mode-1 to mode-4 are observed as the external pressure P increases from 0 to about 0.66, as shown in Fig. 5.22. Mode-1 occurs for $0 < P \lesssim 0.01$, transitions to mode-2 for $0.01 \lesssim P \lesssim 0.16$, to mode-3 for $0.16 \lesssim P \lesssim 0.41$ and mode-4 for $0.41 \lesssim P \lesssim 0.66$. For larger P modes 5, 6 and 7 were obtained, although the solution for large P that gives rise to the higher modes is more demanding on the mesh qualities. No higher modes except mode-2 were found for the linear model.

(a)	(b)	(c)	(d)
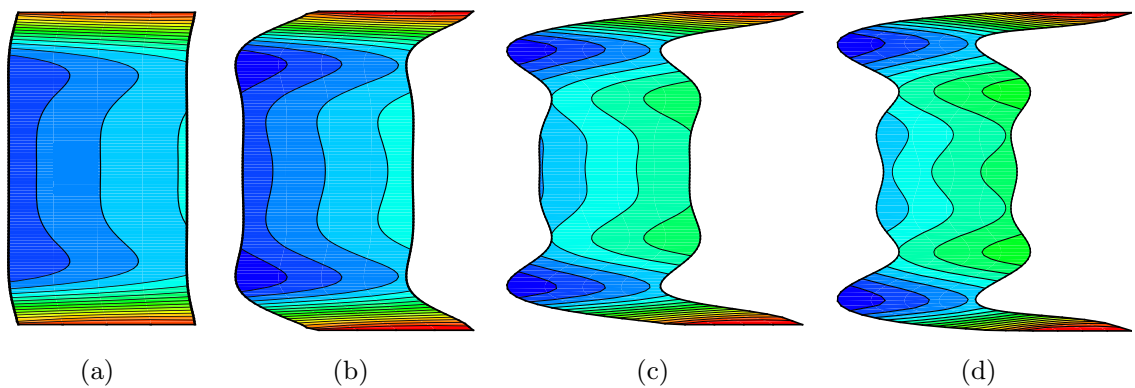
Figure 5.22: (Not to scale) Nonlinear modes of deformation for a tube with $A/B = 0.8, L/B = 5$: (a) mode-1, at $P = 0.01$, (b) mode-2, at $P = 0.11$, (c) mode-3, at $P = 0.41$, (d) mode-4, at $P = 0.61$. The contours shown are for the radial displacement u superimposed on the (r, z) deformed profile.

Figure 5.23 shows the distributions of all the Cauchy stress components for the nonlinear case at $P = 0.22$. Again, there are two major differences when compared with the corresponding linear case (not shown). One is that the nonlinear model presents a higher mode (mode-4 in this case), where the corresponding linear case exhibits only mode-2. The other is the shear splitting pattern in the nonlinear model, which expands from the two ends towards the middle section. Although this is not shown here we note that the boundary effect is more limited to near the two ends in the linear model, with the same sign of $\sigma_{13} \geq 0$ near the upper end, and $\sigma_{13} \leq 0$ near the lower end. The patterns of σ_{22} and σ_{33} are also quite interesting, with the nonlinear effects more clearly focused on the boundaries.
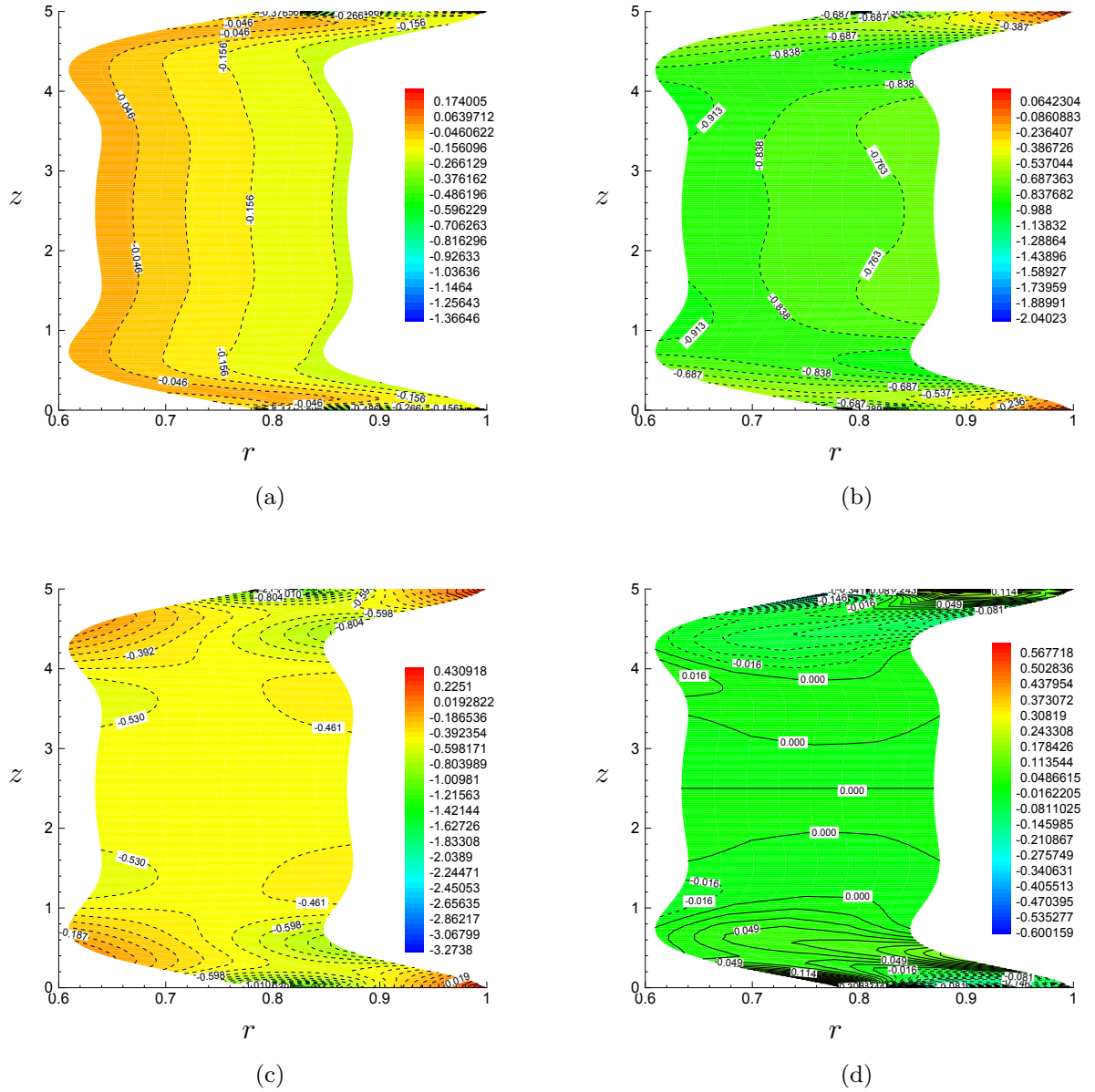
Figure 5.23: Cauchy stress distributions for the nonlinear case for a tube with $A/B = 0.8, L/B = 5$ at pressure $P = 0.22$ superimposed on the deformed tube section in (r, z) space: positive values are indicated by solid contours and negative values by dashed contours. (a) σ_{11}, (b) σ_{22}, (c) σ_{33}, (d) σ_{13}.

5.6 Discussion and conclusions

We have derived the general partial differential equations in Lagrangian form governing the large axisymmetric deformations of a thick-walled tube composed of incompressible isotropic elastic material, without any assumptions limiting the magnitude of the deformation or material nonlinearity. Comparison has been made with the corresponding linear

model for tubes with different wall-thickness and length ratios.

For small deformation the linear and nonlinear models give very similar results. However, the predictions of the linear and nonlinear models are very different under large external pressure, and the dominant nonlinear features are the corner bulging, and, for longer tubes, the occurrence of higher modes of deformation. Note, however, that the higher modes for longer and thinner tubes can be associated with geometrical nonlinearity and are not features unique to material nonlinearity [38], [36]. Although we don't distinguish the material and geometric nonlinearities in the present study, we have observed that material nonlinearity is more important in the shorter and thicker tubes, for which the strains computed are larger, while geometrical nonlinearity seems to dominate in the longer and thinner tubes, for which the strains are much smaller. The Cauchy stresses, especially the shear stress, exhibit the greatest differences between the predictions of the linear and nonlinear theories. Shear splitting, with alternating signs of the shear stress in different regions is a unique nonlinear feature. As a result, the end boundary constraints have a much stronger influence on the deformation and stresses in the rest of the tube for the nonlinear model. This is the first systematic nonlinear treatment of externally pressurized thick-walled elastic tubes, albeit using the simple neo-Hookean material, and the results may have significant implications for certain physiological applications involving soft vessels undergoing large deformation.

The nonlinear system of equations has been solved by using the C++ based finite element package Libmesh. It should be noted that due to the complex nature of the nonlinear equations, it was extremely difficult to obtain converged solutions numerically using approximate Newton solvers and it was necessary to derive the Jacobian matrix $\mathbf{J}$ analytically, and to use the corresponding linear solution as an initial solution in order to obtain convergence. In addition, since the geometry of the tube in the reference configuration and the boundary conditions and external pressure condition are all symmetric about the mid-plane of the tube, a symmetric mesh needs to be used to achieve perfectly symmetric solutions.

We have noted that the nonlinear effects for long, thin tubes are limited to a layer of width $\sqrt{(B-A)A}$ (see [47]) near the boundaries; see Fig. 5.22. This agrees broadly with the examples given by [47] on the behaviour of nonlinear shell-membrane materials. No direct results can be found in [47] for a neo-Hookean cylindrical shell under external pressure. However, qualitative comparison is possible with the results of [69] who studied

the deformation of a neo-Hookean cylindrical membrane under twist. They found that at larger values of the prescribed twist, wrinkling occurs in the interior and the membrane remains tense near the boundaries. Although these are obtained for different boundary conditions, the nonlinear effects such as the presence of the boundary layer and multi-modes are similar to these shown in Fig. 5.22.

Chapter 6

Three-dimensional large deformations

In this chapter we formulate the differential equations governing the large deformation of the cylindrical tube subject to pressure on its external lateral surface and the end conditions are zero displacement. The material is assumed to be an incompressible isotropic neo-Hookean one. The nonlinear set of equations were derived using both cylindrical and Cartesian coordinates. For the purpose of comparison the corresponding linear equations are also presented (using Cartesian coordinates).

6.1 Nonlinear case: cylindrical polar coordinates

Considering the special geometry of the tube, it is natural to formulate the differential equations based on the cylindrical coordinates. This is convenient, especially, when we impose the hydrostatic pressure on the external lateral surface of the tube.

6.1.1 Deformation gradient

Using the basic kinematic concepts described in Chapter 2 and we have the position vectors $\mathbf{X}, \mathbf{x}$ and displacement vector $\mathbf{u}$ (in cylindrical coordinates) in the form

$$\mathbf{x} = r\mathbf{e}_r + z\mathbf{e}_z, \tag{6.1}$$

$$\mathbf{X} = R\mathbf{E}_R + Z\mathbf{E}_Z, \tag{6.2}$$

$$\mathbf{x} = \mathbf{X} + \mathbf{u}, \tag{6.3}$$

where displacement vector is given by

$$\mathbf{u} = u\mathbf{e}_r + v\mathbf{e}_\theta + w\mathbf{e}_z. \tag{6.4}$$

Note that r, θ, z are functions of R, Θ, Z.

$$r = r(R, \Theta, Z), \quad \theta = \Theta(R, \Theta, Z), \quad z = Z(R, \Theta, Z), \tag{6.5}$$

$$u = u(R, \Theta, Z), \quad v = v(R, \Theta, Z), \quad w = w(R, \Theta, Z), \tag{6.6}$$

and the relation between bases of cylindrical coordinates and bases of Cartesian coordinates gives

$$\mathbf{e}_r = \cos\theta\mathbf{e}_1 + \sin\theta\mathbf{e}_2, \quad \mathbf{e}_\theta = -\sin\theta\mathbf{e}_1 + \cos\theta\mathbf{e}_2, \quad \mathbf{e}_z = \mathbf{e}_3,$$

$$\mathbf{E}_R = \cos\Theta\mathbf{E}_1 + \sin\Theta\mathbf{E}_2, \quad \mathbf{E}_\Theta = -\sin\Theta\mathbf{E}_1 + \cos\Theta\mathbf{E}_2, \quad \mathbf{E}_Z = \mathbf{E}_3. \tag{6.7}$$

Here we have

$$\mathbf{e}_i = \mathbf{E}_i, \quad i = 1, 2, 3. \tag{6.8}$$

The gradient in cylindrical coordinate system gives

$$\mathrm{Grad}\,\mathbf{x} = \frac{\partial\mathbf{x}}{\partial R} \otimes \mathbf{E}_R + \frac{1}{R}\frac{\partial\mathbf{x}}{\partial\Theta} \otimes \mathbf{E}_\Theta + \frac{\partial\mathbf{x}}{\partial Z} \otimes \mathbf{E}_Z. \tag{6.9}$$

We specialize the deformation gradient (2.2) and combined with (6.9), then

$$\begin{aligned}
\mathbf{F} &= \mathrm{Grad}\,\mathbf{x} \\
&= \frac{\partial r}{\partial R}\mathbf{e}_r \otimes \mathbf{E}_R + \frac{1}{R}\frac{\partial r}{\partial\Theta}\mathbf{e}_r \otimes \mathbf{E}_\Theta + \frac{\partial r}{\partial Z}\mathbf{e}_r \otimes \mathbf{E}_Z + r\frac{\partial\theta}{\partial R}\mathbf{e}_\theta \otimes \mathbf{E}_R + \frac{r}{R}\frac{\partial\theta}{\partial\Theta}\mathbf{e}_\theta \otimes \mathbf{E}_\Theta \\
&\quad + r\frac{\partial\theta}{\partial Z}\mathbf{e}_\theta \otimes \mathbf{E}_Z + \frac{\partial z}{\partial R}\mathbf{e}_z \otimes \mathbf{E}_R + \frac{1}{R}\frac{\partial z}{\partial\Theta}\mathbf{e}_z \otimes \mathbf{E}_\Theta + \frac{\partial z}{\partial Z}\mathbf{e}_z \otimes \mathbf{E}_Z. \tag{6.10}
\end{aligned}$$

Or by using u, v, w, we get the deformation gradient as follows

$$\mathbf{F} = \mathrm{Grad}\,\mathbf{x} = \mathrm{Grad}\,\mathbf{u} + \mathbf{I}, \tag{6.11}$$

and $\mathrm{Grad}\,\mathbf{u}$ gives

$$\begin{aligned}
\mathrm{Grad}\,\mathbf{u} &= (\frac{\partial u}{\partial R} - v\frac{\partial\theta}{\partial R})\mathbf{e}_r \otimes \mathbf{E}_R + (\frac{1}{R}\frac{\partial u}{\partial\Theta} - \frac{v}{R}\frac{\partial\theta}{\partial\Theta})\mathbf{e}_r \otimes \mathbf{E}_\Theta + (\frac{\partial u}{\partial Z} - v\frac{\partial\theta}{\partial Z})\mathbf{e}_r \otimes \mathbf{E}_Z \\
&\quad + (u\frac{\partial\theta}{\partial R} + \frac{\partial v}{\partial R})\mathbf{e}_\theta \otimes \mathbf{E}_R + (\frac{u}{R}\frac{\partial\theta}{\partial\Theta} + \frac{1}{R}\frac{\partial v}{\partial\Theta})\mathbf{e}_\theta \otimes \mathbf{E}_\Theta + (u\frac{\partial\theta}{\partial Z} + \frac{\partial v}{\partial Z})\mathbf{e}_\theta \otimes \mathbf{E}_Z \\
&\quad + \frac{\partial w}{\partial R}\mathbf{e}_z \otimes \mathbf{E}_R + \frac{1}{R}\frac{\partial w}{\partial\Theta}\mathbf{e}_z \otimes \mathbf{E}_\Theta + \frac{\partial w}{\partial Z}\mathbf{e}_z \otimes \mathbf{E}_Z. \tag{6.12}
\end{aligned}$$

¿From (6.22), we have connections between the coordinates in current and reference configurations in the form

$$
\begin{cases}
r\cos\theta = R\cos\Theta + u\cos\theta - v\sin\theta, \\
r\sin\theta = R\sin\Theta + u\sin\theta + v\cos\theta, \\
z = Z + w.
\end{cases}
\tag{6.13}
$$

¿From the first two equations in (6.13), we obtain the important relation

$$
\theta = \Theta \pm \arccos\frac{r-u}{R} + 2k\pi, \quad k = 1, 2, 3...
\tag{6.14}
$$

Then we could easily get $\frac{\partial\theta}{\partial R}, \frac{\partial\theta}{\partial\Theta}, \frac{\partial\theta}{\partial Z}$, but we don't want to express these derivatives explicitly due to the complexity of the expressions.

6.1.2 Nominal stress and Cauchy stress

The strain-energy function for neo-Hookean material is

$$
W(I_1) = \frac{1}{2}\mu(I_1 - 3).
\tag{6.15}
$$

Using the definition (2.53) the nominal stress for incompressible elastic material is specialized accordingly

$$
\mathbf{S} = \frac{\partial W}{\partial\mathbf{F}} - p\mathbf{F}^{-1} = \mu\mathbf{F}^T - p\mathbf{F}^{-1}.
\tag{6.16}
$$

For this case, the Cauchy stress tensor could be written

$$
\sigma = \mathbf{F}\frac{\partial W}{\partial\mathbf{F}} - p\mathbf{I} = \mu\mathbf{F}\mathbf{F}^T - p\mathbf{I}.
\tag{6.17}
$$

The inverse of the deformation gradient F is given by

$$
\mathbf{F}^{-1} =
\begin{Bmatrix}
\frac{r}{R}\left(\frac{\partial\theta}{\partial\Theta}\frac{\partial z}{\partial Z} - \frac{\partial\theta}{\partial Z}\frac{\partial z}{\partial\Theta}\right) & -\frac{1}{R}\left(\frac{\partial r}{\partial\Theta}\frac{\partial z}{\partial Z} - \frac{\partial r}{\partial Z}\frac{\partial z}{\partial\Theta}\right) & \frac{r}{R}\left(\frac{\partial r}{\partial\Theta}\frac{\partial\theta}{\partial Z} - \frac{\partial r}{\partial Z}\frac{\partial\theta}{\partial\Theta}\right) \\
-r\left(\frac{\partial\theta}{\partial R}\frac{\partial z}{\partial Z} - \frac{\partial\theta}{\partial Z}\frac{\partial z}{\partial R}\right) & \frac{\partial r}{\partial R}\frac{\partial z}{\partial Z} - \frac{\partial r}{\partial Z}\frac{\partial z}{\partial R} & -r\left(\frac{\partial r}{\partial R}\frac{\partial\theta}{\partial Z} - \frac{\partial r}{\partial Z}\frac{\partial\theta}{\partial R}\right) \\
\frac{r}{R}\left(\frac{\partial\theta}{\partial R}\frac{\partial z}{\partial\Theta} - \frac{\partial\theta}{\partial\Theta}\frac{\partial z}{\partial R}\right) & -\frac{1}{R}\left(\frac{\partial r}{\partial R}\frac{\partial z}{\partial\Theta} - \frac{\partial r}{\partial\Theta}\frac{\partial z}{\partial R}\right) & \frac{r}{R}\left(\frac{\partial r}{\partial R}\frac{\partial\theta}{\partial\Theta} - \frac{\partial r}{\partial\Theta}\frac{\partial\theta}{\partial R}\right)
\end{Bmatrix}
\tag{6.18}
$$

So, the nominal stress is given by in component form

$$
\mathbf{S} = \mu
\begin{Bmatrix}
\frac{\partial r}{\partial R} & r\frac{\partial\theta}{\partial R} & \frac{\partial z}{\partial R} \\
\frac{1}{R}\frac{\partial r}{\partial\Theta} & \frac{r}{R}\frac{\partial\theta}{\partial\Theta} & \frac{1}{R}\frac{\partial z}{\partial\Theta} \\
\frac{\partial r}{\partial Z} & r\frac{\partial\theta}{\partial Z} & \frac{\partial z}{\partial Z}
\end{Bmatrix}
- p
\begin{Bmatrix}
\frac{r}{R}\left(\frac{\partial\theta}{\partial\Theta}\frac{\partial z}{\partial Z} - \frac{\partial\theta}{\partial Z}\frac{\partial z}{\partial\Theta}\right) & -\frac{1}{R}\left(\frac{\partial r}{\partial\Theta}\frac{\partial z}{\partial Z} - \frac{\partial r}{\partial Z}\frac{\partial z}{\partial\Theta}\right) & \frac{r}{R}\left(\frac{\partial r}{\partial\Theta}\frac{\partial\theta}{\partial Z} - \frac{\partial r}{\partial Z}\frac{\partial\theta}{\partial\Theta}\right) \\
-r\left(\frac{\partial\theta}{\partial R}\frac{\partial z}{\partial Z} - \frac{\partial\theta}{\partial Z}\frac{\partial z}{\partial R}\right) & \frac{\partial r}{\partial R}\frac{\partial z}{\partial Z} - \frac{\partial r}{\partial Z}\frac{\partial z}{\partial R} & -r\left(\frac{\partial r}{\partial R}\frac{\partial\theta}{\partial Z} - \frac{\partial r}{\partial Z}\frac{\partial\theta}{\partial R}\right) \\
\frac{r}{R}\left(\frac{\partial\theta}{\partial R}\frac{\partial z}{\partial\Theta} - \frac{\partial\theta}{\partial\Theta}\frac{\partial z}{\partial R}\right) & -\frac{1}{R}\left(\frac{\partial r}{\partial R}\frac{\partial z}{\partial\Theta} - \frac{\partial r}{\partial\Theta}\frac{\partial z}{\partial R}\right) & \frac{r}{R}\left(\frac{\partial r}{\partial R}\frac{\partial\theta}{\partial\Theta} - \frac{\partial r}{\partial\Theta}\frac{\partial\theta}{\partial R}\right)
\end{Bmatrix}.
$$

6.1.3 Equilibrium equations

Using the Lagrangean equilibrium equation (2.18) we have

$$
\begin{aligned}
\text{Div}\,\mathbf{S} &= \frac{\partial S_{ij}}{\partial X_k}\mathbf{E}_k \cdot \mathbf{E}_i \otimes \mathbf{e}_j + S_{ij}\mathbf{E}_k \cdot \frac{\partial \mathbf{E}_i}{X_k} \otimes \mathbf{e}_j + S_{ij}\mathbf{E}_k \cdot \mathbf{E}_i \otimes \frac{\partial \mathbf{e}_j}{X_k} \\
&= \frac{\partial S_{ij}}{\partial X_i}\mathbf{e}_j + S_{ij}\mathbf{E}_k \cdot \frac{\partial \mathbf{E}_i}{\partial X_k}\mathbf{e}_j + S_{ij}\frac{\partial \mathbf{e}_j}{\partial X_i} = 0 \quad i,j = 1,2,3.
\end{aligned}
\tag{6.19}
$$

Non-zero components of $\mathbf{E_k} \cdot \mathbf{E_{i,k}}$ in cylindrical coordinate system are

$$
\mathbf{E}_2 \cdot \mathbf{E}_{1,2} = \frac{1}{R}\mathbf{E}_\Theta \cdot \mathbf{E}_{R,\Theta} = \frac{1}{R}.
\tag{6.20}
$$

The final equilibrium equations could be written as

$$
\begin{aligned}
\frac{\partial S_{11}}{\partial R} + \frac{1}{R}\frac{\partial S_{21}}{\partial \Theta} + \frac{\partial S_{31}}{\partial Z} + \frac{1}{R}S_{11} - \left(S_{12}\frac{\partial \theta}{\partial R} + \frac{1}{R}S_{22}\frac{\partial \theta}{\partial \Theta} + S_{32}\frac{\partial \theta}{\partial Z}\right) &= 0, \\
\frac{\partial S_{12}}{\partial R} + \frac{1}{R}\frac{\partial S_{22}}{\partial \Theta} + \frac{\partial S_{32}}{\partial Z} + \frac{1}{R}S_{12} + \left(S_{11}\frac{\partial \theta}{\partial R} + \frac{1}{R}S_{21}\frac{\partial \theta}{\partial \Theta} + S_{31}\frac{\partial \theta}{\partial Z}\right) &= 0, \\
\frac{\partial S_{13}}{\partial R} + \frac{1}{R}\frac{\partial S_{23}}{\partial \Theta} + \frac{\partial S_{33}}{\partial Z} + \frac{1}{R}S_{13} &= 0.
\end{aligned}
\tag{6.21}
$$

Considering the complicated connections in (6.13), (6.14) and the components of nominal stress tensor, we can easily imagine the final form of the equilibrium equations (6.21) would be very lengthy, which will add much difficulty in the procedure of numerical simulations.

6.2 Nonlinear case: cartesian coordinates

In order to avoid the complexity of the equilibrium equations (6.21), we obtain the corresponding equation system in Cartesian coordinates as follows.

6.2.1 Deformation gradient

The position vectors of an arbitral particle of the body are denoted by

$$
\mathbf{x} = x_i\mathbf{e}_i, \quad \mathbf{X} = X_i\mathbf{E}_i, \quad \mathbf{x} = \mathbf{X} + \mathbf{u}.
\tag{6.22}
$$

where $i = 1,2,3$ and the displacement vector is given by

$$
\mathbf{u} = u\mathbf{e}_1 + v\mathbf{e}_2 + w\mathbf{e}_3.
\tag{6.23}
$$

The deformation gradient (2.2) in Cartesian coordinates is given by

$$
\mathbf{F} = \text{Grad}\,\mathbf{x} = \frac{\partial x_i}{\partial X_j}\mathbf{e}_i \otimes \mathbf{E}_j \quad i,j = 1,2,3.
\tag{6.24}
$$

alternatively, which is

$$
\begin{aligned}
\mathbf{F} = \; & \frac{\partial x_1}{\partial X_1}\mathbf{e}_1 \otimes \mathbf{E}_1 + \frac{\partial x_1}{\partial X_2}\mathbf{e}_1 \otimes \mathbf{E}_2 + \frac{\partial x_1}{\partial X_3}\mathbf{e}_1 \otimes \mathbf{E}_3 + \\
& \frac{\partial x_2}{\partial X_1}\mathbf{e}_2 \otimes \mathbf{E}_1 + \frac{\partial x_2}{\partial X_2}\mathbf{e}_2 \otimes \mathbf{E}_2 + \frac{\partial x_2}{\partial X_3}\mathbf{e}_2 \otimes \mathbf{E}_3 + \\
& \frac{\partial x_3}{\partial X_1}\mathbf{e}_3 \otimes \mathbf{E}_1 + \frac{\partial x_3}{\partial X_2}\mathbf{e}_3 \otimes \mathbf{E}_2 + \frac{\partial x_3}{\partial X_3}\mathbf{e}_3 \otimes \mathbf{E}_3.
\end{aligned}
\tag{6.25}
$$

6.2.2 Nominal stress and Cauchy stress

The inverse of the deformation gradient F is given by

$$
\mathbf{F}^{-1} =
\begin{Bmatrix}
\frac{\partial x_2}{\partial X_2}\frac{\partial x_3}{\partial X_3} - \frac{\partial x_2}{\partial X_3}\frac{\partial x_3}{\partial X_2} & \frac{\partial x_1}{\partial X_3}\frac{\partial x_3}{\partial X_2} - \frac{\partial x_1}{\partial X_2}\frac{\partial x_3}{\partial X_3} & \frac{\partial x_1}{\partial X_2}\frac{\partial x_2}{\partial X_3} - \frac{\partial x_1}{\partial X_3}\frac{\partial x_2}{\partial X_2} \\[2mm]
\frac{\partial x_2}{\partial X_3}\frac{\partial x_3}{\partial X_1} - \frac{\partial x_2}{\partial X_1}\frac{\partial x_3}{\partial X_3} & \frac{\partial x_1}{\partial X_1}\frac{\partial x_3}{\partial X_3} - \frac{\partial x_1}{\partial X_3}\frac{\partial x_3}{\partial X_1} & \frac{\partial x_1}{\partial X_3}\frac{\partial x_2}{\partial X_1} - \frac{\partial x_1}{\partial X_1}\frac{\partial x_2}{\partial X_3} \\[2mm]
\frac{\partial x_2}{\partial X_1}\frac{\partial x_3}{\partial X_2} - \frac{\partial x_2}{\partial X_2}\frac{\partial x_3}{\partial X_1} & \frac{\partial x_1}{\partial X_2}\frac{\partial x_3}{\partial X_1} - \frac{\partial x_1}{\partial X_1}\frac{\partial x_3}{\partial X_2} & \frac{\partial x_1}{\partial X_1}\frac{\partial x_2}{\partial X_2} - \frac{\partial x_1}{\partial X_2}\frac{\partial x_2}{\partial X_1}
\end{Bmatrix}
\tag{6.26}
$$

We now substitute the strain-energy function for neo-Hookean material (6.15) and (6.26) into the the nominal stress (6.16) for incompressible elastic material to obtain

$$
\mathbf{S} = \mu
\begin{Bmatrix}
\frac{\partial x_1}{\partial X_1} & \frac{\partial x_2}{\partial X_1} & \frac{\partial x_3}{\partial X_1} \\[2mm]
\frac{\partial x_1}{\partial X_2} & \frac{\partial x_2}{\partial X_2} & \frac{\partial x_3}{\partial X_2} \\[2mm]
\frac{\partial x_1}{\partial X_3} & \frac{\partial x_2}{\partial X_3} & \frac{\partial x_3}{\partial X_3}
\end{Bmatrix}
- p
\begin{Bmatrix}
\frac{\partial x_2}{\partial X_2}\frac{\partial x_3}{\partial X_3} - \frac{\partial x_2}{\partial X_3}\frac{\partial x_3}{\partial X_2} & \frac{\partial x_1}{\partial X_3}\frac{\partial x_3}{\partial X_2} - \frac{\partial x_1}{\partial X_2}\frac{\partial x_3}{\partial X_3} & \frac{\partial x_1}{\partial X_2}\frac{\partial x_2}{\partial X_3} - \frac{\partial x_1}{\partial X_3}\frac{\partial x_2}{\partial X_2} \\[2mm]
\frac{\partial x_2}{\partial X_3}\frac{\partial x_3}{\partial X_1} - \frac{\partial x_2}{\partial X_1}\frac{\partial x_3}{\partial X_3} & \frac{\partial x_1}{\partial X_1}\frac{\partial x_3}{\partial X_3} - \frac{\partial x_1}{\partial X_3}\frac{\partial x_3}{\partial X_1} & \frac{\partial x_1}{\partial X_3}\frac{\partial x_2}{\partial X_1} - \frac{\partial x_1}{\partial X_1}\frac{\partial x_2}{\partial X_3} \\[2mm]
\frac{\partial x_2}{\partial X_1}\frac{\partial x_3}{\partial X_2} - \frac{\partial x_2}{\partial X_2}\frac{\partial x_3}{\partial X_1} & \frac{\partial x_1}{\partial X_2}\frac{\partial x_3}{\partial X_1} - \frac{\partial x_1}{\partial X_1}\frac{\partial x_3}{\partial X_2} & \frac{\partial x_1}{\partial X_1}\frac{\partial x_2}{\partial X_2} - \frac{\partial x_1}{\partial X_2}\frac{\partial x_2}{\partial X_1}
\end{Bmatrix}.
$$

6.2.3 Governing equations

Using (2.18) we have the equilibrium equations

$$
\begin{aligned}
\operatorname{Div}\mathbf{S} &= \frac{\partial S_{ij}}{\partial X_k}\mathbf{E}_k \cdot \mathbf{E}_i \otimes \mathbf{e}_j \\
&= \frac{\partial S_{ij}}{\partial X_i}\mathbf{e}_j = 0 \quad i,j = 1,2,3.
\end{aligned}
\tag{6.27}
$$

The final equilibrium equations in component form could be written as

$$
\frac{\partial S_{11}}{\partial X_1} + \frac{\partial S_{21}}{\partial X_2} + \frac{\partial S_{31}}{\partial X_3} = 0,
\tag{6.28}
$$

$$
\frac{\partial S_{12}}{\partial X_1} + \frac{\partial S_{22}}{\partial X_2} + \frac{\partial S_{32}}{\partial X_3} = 0,
\tag{6.29}
$$

$$
\frac{\partial S_{13}}{\partial X_1} + \frac{\partial S_{23}}{\partial X_2} + \frac{\partial S_{33}}{\partial X_3} = 0.
\tag{6.30}
$$

The pressure boundary conditions are given as

$$
\mathbf{S}^{\mathrm{T}}\mathbf{N} =
\begin{cases}
-P\mathbf{F}^{-\mathrm{T}}\mathbf{N} & \text{on } R = B \\[2mm]
\mathbf{0} & \text{on } R = A,
\end{cases}
\tag{6.31}
$$

In component form which are

$$\begin{cases} S_{11}N_1 + S_{21}N_2 = -P(F_{11}^{-1}N_1 + F_{21}^{-1}N_2), \\ S_{12}N_1 + S_{22}N_2 = -P(F_{12}^{-1}N_1 + F_{22}^{-1}N_2), \\ S_{13}N_1 + S_{23}N_2 = -P(F_{13}^{-1}N_1 + F_{23}^{-1}N_2). \end{cases} \tag{6.32}$$

The end conditions are zero displacements i.e.

$$u = v = w = 0. \tag{6.33}$$

And the incompressible condition is

$$J = \det \mathbf{F} = 1 \tag{6.34}$$

and J is

$$\begin{aligned} J = & \frac{\partial x_1}{\partial X_1}\Big(\frac{\partial x_2}{\partial X_2}\frac{\partial x_3}{\partial X_3} - \frac{\partial x_2}{\partial X_3}\frac{\partial x_3}{\partial X_2}\Big) + \frac{\partial x_1}{\partial X_2}\Big(\frac{\partial x_2}{\partial X_3}\frac{\partial x_3}{\partial X_1} - \frac{\partial x_2}{\partial X_1}\frac{\partial x_3}{\partial X_3}\Big) \\ & + \frac{\partial x_1}{\partial X_3}\Big(\frac{\partial x_2}{\partial X_1}\frac{\partial x_3}{\partial X_2} - \frac{\partial x_2}{\partial X_2}\frac{\partial x_3}{\partial X_1}\Big). \end{aligned} \tag{6.35}$$

6.2.4 Unit outward normal to the outer surface

Let P be the arbitrary point on the outer surface, O be the original point located on the center of the bottom of the cylinder. We choose the outer radius of the cylinder $B = 1$. We use $\mathbf{R}$ denoting the position vector $\overrightarrow{OP}$ which is given by

$$\mathbf{R} = B\cos\Theta\mathbf{E}_1 + B\sin\Theta\mathbf{E}_2 + Z\mathbf{E}_3 \tag{6.36}$$

The unit outward normal to the outer surface is given by

$$\begin{aligned} \mathbf{N} &= \frac{\mathbf{R}_\Theta \times \mathbf{R}_Z}{\parallel \mathbf{R}_\Theta \times \mathbf{R}_Z \parallel} \\ &= \cos\Theta\mathbf{E}_1 + \sin\Theta\mathbf{E}_2 \\ &= X_1\mathbf{E}_1 + X_2\mathbf{E}_2. \end{aligned} \tag{6.37}$$

6.3 Linear case

The linear case is presented for comparison with the above nonlinear one.

6.3.1   Deformation gradient and Cauchy stress

The deformation gradient in matrix form,

$$\mathbf{F} = \left\{ \begin{array}{ccc} \frac{\partial u_1}{\partial x_1} + 1 & \frac{\partial u_1}{\partial x_2} & \frac{\partial u_1}{\partial x_3} \\[2mm] \frac{\partial u_2}{\partial x_1} & \frac{\partial u_2}{\partial x_2} + 1 & \frac{\partial u_2}{\partial x_3} \\[2mm] \frac{\partial u_3}{\partial x_1} & \frac{\partial u_3}{\partial x_2} & \frac{\partial u_3}{\partial x_3} + 1 \end{array} \right\}. \tag{6.38}$$

We have the Cauchy stress tensor for isotropic incompressible material in the form

$$\boldsymbol{\sigma} = -p\mathbf{I} + \mu[\operatorname{grad}\mathbf{u} + (\operatorname{grad}\mathbf{u})^{\mathrm{T}}], \tag{6.39}$$

where

$$\operatorname{grad}\mathbf{u} = \frac{\partial u_i}{\partial x_j}\mathbf{e}_i \otimes \mathbf{e}_j \quad i,j = 1,2,3. \tag{6.40}$$

The final component form of Cauchy stress is given by

$$\sigma = \mu \left\{ \begin{array}{ccc} 2\frac{\partial u_1}{\partial x_1} - \frac{p}{\mu} & \frac{\partial u_1}{\partial x_2} + \frac{\partial u_2}{\partial x_1} & \frac{\partial u_1}{\partial x_3} + \frac{\partial u_3}{\partial x_1} \\[2mm] \frac{\partial u_1}{\partial x_2} + \frac{\partial u_2}{\partial x_1} & 2\frac{\partial u_2}{\partial x_2} - \frac{p}{\mu} & \frac{\partial u_2}{\partial x_3} + \frac{\partial u_3}{\partial x_2} \\[2mm] \frac{\partial u_1}{\partial x_3} + \frac{\partial u_3}{\partial x_1} & \frac{\partial u_2}{\partial x_3} + \frac{\partial u_3}{\partial x_2} & 2\frac{\partial u_3}{\partial x_3} - \frac{p}{\mu} \end{array} \right\} \tag{6.41}$$

6.3.2   Governing equations

Using the equilibrium equation (2.19) we obtain

$$\frac{\partial \sigma_{11}}{\partial x_1} + \frac{\partial \sigma_{21}}{\partial x_2} + \frac{\partial \sigma_{31}}{\partial x_3} = 0, \tag{6.42}$$

$$\frac{\partial \sigma_{12}}{\partial x_1} + \frac{\partial \sigma_{22}}{\partial x_2} + \frac{\partial \sigma_{32}}{\partial x_3} = 0, \tag{6.43}$$

$$\frac{\partial \sigma_{13}}{\partial x_1} + \frac{\partial \sigma_{23}}{\partial x_2} + \frac{\partial \sigma_{33}}{\partial x_3} = 0. \tag{6.44}$$

And the incompressible condition is

$$\operatorname{div}\mathbf{u} = \frac{\partial u_i}{\partial x_i} = \frac{\partial u_1}{\partial x_1} + \frac{\partial u_2}{\partial x_2} + \frac{\partial u_3}{\partial x_3} = 0, \tag{6.45}$$

where $\mathbf{u}$ is the displacement vector.

The pressure boundary conditions are

$$\boldsymbol{\sigma}\mathbf{n} = \left\{ \begin{array}{ll} -P\mathbf{n} & \text{on } R = B \\[2mm] \mathbf{0} & \text{on } R = A, \end{array} \right. \tag{6.46}$$

where $\mathbf{n}$ the unit outer normal to the external lateral surface of the tube. The component form is given by

$$
\begin{cases}
\sigma_{11}n_1 + \sigma_{12}n_2 = -Pn_1, \\
\sigma_{21}n_1 + \sigma_{22}n_2 = -Pn_2, \\
\sigma_{31}n_1 + \sigma_{32}n_2 = 0.
\end{cases}
\tag{6.47}
$$

The end conditions are zero displacement i.e.

$$
u = v = w = 0.
\tag{6.48}
$$

Chapter 7

Conclusions

The main contributions of this research are the investigation of both the axisymmetric and asymmetric bifurcations of thick-walled circular cylindrical elastic tubes under axial loading and external pressure based on the work of Haughton and Ogden [35] and the nonlinear analysis of the finite axisymmetric deformations of an elastic tube under external pressure based on the general fully nonlinear governing equations in Lagrangian form, and finally, the development of the partial differential equations for the three dimensional large deformations of an elastic tube under external pressure.

As stated in the discussion and conclusion in Chapters 4 and 5, we summarize our main results here.

In the work [78] (in Chapter 4), we found that the mode-2 bifurcation pressure is insensitive to the variation of the wall thickness and deviate from the thin shell prediction in both the very thin and thick-walled regimes. The mode transition from lower to higher ones occurs in the range of axial compression, for very short and sufficiently thick tubes. We have also shown that, contrary to thin-shell theory, for sufficiently thick tubes, mode 2 bifurcation becomes the only dominant mode, without transition from lower to higher modes for sufficiently short tubes.

In the work [79] (in Chapter 5), as expected, the linear and nonlinear models represent nearly the same results for small deformation. However, large differences have been found in the predictions of the linear and nonlinear models under large external pressure, and the dominant nonlinear features are the corner bulging, for relatively short tubes and, the occurrence of higher mode deformations for longer tubes. It has been observed that material nonlinearity dominates the deformations in the shorter and thicker tubes, for which the strains computed are larger, while geometrical nonlinearity seems to provide

more influence on the deformations in the longer and thinner tubes, for which the strains are much smaller. The shear components of Cauchy stress exhibits the greatest differences between the results of the linear and nonlinear theories. Shear splitting, with variation in signs of the shear stress in neighbouring regions is a unique nonlinear feature. The boundary layer formation at the ends of the long, thin tubes, which is a hallmark of classical shell theory, is also represented in the nonlinear analysis. This is the first systematic nonlinear analysis of externally pressurized thick-walled elastic tubes, although the simple neo-Hookean material has been adopted, and the results may have significant implications for certain physiological problems involving soft vessels undergoing large deformation.

Regarding future projects, there are several possibilities as follows.

In the next phase of the work in Chapter 4 we shall investigate the post-buckling behaviour of elastic tubes under external pressure and axial loading. In particular, the effect of wall-thickness on compliance of the tubes between buckling and self contact will be studied in order to interpret the puzzling phenomenon that for tubes subjected to external pressure, after a certain degree of collapse, thick tubes may be more compliant than thinner ones [11, 52].

Since we have dealt with axisymmetric problems in Chapter 5, we can only simulate the necked or barrelled states of a cylinder. In addition, we have not carried out any bifurcation analysis and it remains to ascertain the stability status of the solutions obtained, although previous studies on similar nonlinear problems, albeit with different boundary conditions [55], have shown that there exist nontrivial axisymmetric stable (half neck or multiple-neck) solutions. However, in many physiological situations, nonlinear deformations that break this symmetry (both for the original deformation or the bifurcation analysis) could be more significant. We shall continue to pursue this problem in subsequent work based on the results of Chapter 5. Considering the fully nonlinear structures of the system of the equations governing the three dimensional deformations, in the numerical solution, resulting in a dense and nonsymmetric coefficient matrix it is still not sure that the numerical simulation could be carried out successfully using the present finite element method and the algorithms for solving nonlinear sets of equations. (see details in section 9 in the book [62]). In order to avoid the difficulty of solving the nonlinear systems directly, we note that a more natural and effective analysis approach has been developed by Bathe [8] by referring all variables to a previously known calculated equilibrium configuration and linearizing the resulting equations to obtain an approximate

solution. Once the above questions are answered, a natural next step would be to replace the zero-displacement end boundary condition by axial loading including both compression and extension to provide a better approximation of the real physiological problem as mentioned in the Introduction.

Another very interesting but difficult future line of research would be to extend the formulations of all the above problems in Chapter 4-6 to the corresponding dynamics cases.

Appendix A

Appendix A

In this appendix we represent the derivation of discretizing integrations for the nonlinear axisymmetric case in Chapter 5. Note that the subscripts of components of nominal stress tensor S are changed. The connection between the alternative notations and the one used in Chapter 5 are $S_{11} = S_{Rr}, S_{31} = S_{Zr}, S_{13} = S_{Rz}, S_{33} = S_{Zz}, S_{22} = S_{\Theta\theta}$.

A.1   Integration of the equilibrium equations by parts

Applying Galerkin's method to the differential equilibrium equations,

$$\int_{\Omega} N_i[S_{11,1} + S_{31,3} + \frac{1}{R}(S_{11} - S_{22})]\mathrm{d}\Omega = 0 \tag{A.1}$$

$$\int_{\Omega} N_i(S_{13,1} + S_{33,3} + \frac{1}{R}S_{13})\mathrm{d}\Omega = 0 \tag{A.2}$$

where N_i is the i th shape function and Ω is the volume of the cylinder in reference configuration.

For axisymmetric deformations, the nominal stress components and shape functions are independent of the coordinate Θ, we can decompose the integral above as follows,

$$\int_{R,Z} RN_i[S_{11,1} + S_{31,3} + \frac{1}{R}(S_{11} - S_{22})]\mathrm{d}R\mathrm{d}Z = 0 \tag{A.3}$$

$$\int_{R,Z} RN_i(S_{13,1} + S_{33,3} + \frac{1}{R}S_{13})\mathrm{d}R\mathrm{d}Z = 0 \tag{A.4}$$

Integration by parts, the first term of (A.3) can be written as

$$\int_{R,Z} RN_iS_{11,1}\mathrm{d}R\mathrm{d}Z = -\int_{R,Z} (RN_i)_{,1}S_{11}\mathrm{d}R\mathrm{d}Z + \int_Z (RN_iS_{11})|_{R_1}^{R_2}\mathrm{d}Z$$

The second term of (A.3) can be written as

$$\int_{R,Z} RN_iS_{31,3}\mathrm{d}R\mathrm{d}Z = -\int_{R,Z} RN_{i,3}S_{31}\mathrm{d}R\mathrm{d}Z + \int_R R(N_iS_{31})|_{Z_1}^{Z_2}\mathrm{d}R$$

and hence we obtain from (A.3),

$$\int_{R,Z}[R(N_{i,1}S_{11} + N_{i,3}S_{31}) + N_iS_{22}]\mathrm{d}R\mathrm{d}Z = \int_Z (RN_iS_{11})|_{R_1}^{R_2}\mathrm{d}Z + \int_R R(N_iS_{31})|_{Z_1}^{Z_2}\mathrm{d}R \quad (A.5)$$

The similar techniques operate on (A.4), we have

$$\int_{R,Z} R(N_{i,1}S_{13} + N_{i,3}S_{33})\mathrm{d}R\mathrm{d}Z = \int_Z (RN_iS_{13})|_{R_1}^{R_2}\mathrm{d}Z + \int_R R(N_iS_{33})|_{Z_1}^{Z_2}\mathrm{d}R \quad (A.6)$$

We use notations int_1 and int_2 to denote the two integrands in (A.5) and (A.6), respectively,

$$int_1 = R(N_{i,1}S_{11} + N_{i,3}S_{31}) + N_iS_{22}$$

$$int_2 = R(N_{i,1}S_{13} + N_{i,3}S_{33})$$

By the help of mathematica, we obtain

$$\begin{aligned}
int_1 = {} & t_2N_i \\
& + RN_{i,1}\left\{\left[\frac{(1+\cos 2\psi)t_1}{2\lambda_1} + \frac{(1-\cos 2\psi)t_3}{2\lambda_3}\right](1+u_R) + \frac{1}{2}\sin 2\psi(\frac{t_1}{\lambda_1} - \frac{t_3}{\lambda_3})u_Z\right\} \\
& + RN_{i,3}\left\{\frac{1}{2}\sin 2\psi(\frac{t_1}{\lambda_1} - \frac{t_3}{\lambda_3})(1+u_R) \right. \\
& \left. + \left[\frac{(1-\cos 2\psi)t_1}{2\lambda_1} + \frac{(1+\cos 2\psi)t_3}{2\lambda_3}\right]u_Z\right\}
\end{aligned} \quad (A.7)$$

First term of (A.7),

$$\begin{aligned}
\int_{R,Z} t_2N_i\mathrm{d}R\mathrm{d}Z &= \int_{R,Z} N_i(\mu\lambda_2 - p\lambda_2^{-1})\mathrm{d}R\mathrm{d}Z \\
&= \int_{R,Z} N_i(\mu(1+\frac{u}{R}) - \frac{R}{R+u}p)\mathrm{d}R\mathrm{d}Z \\
&= \int_{R,Z} \mu N_i\mathrm{d}R\mathrm{d}Z + \int_{R,Z} \frac{\mu}{R}N_iN_j\mathrm{d}R\mathrm{d}Zu_j - \int_{R,Z} \frac{R}{R+u}N_iN_j'\mathrm{d}R\mathrm{d}Zp_j
\end{aligned}$$

Using $\frac{t_1}{\lambda_1} = \mu - p\lambda_1^{-2}$, second term of (A.7),

$$\begin{aligned}
& \int_{R,Z} RN_{i,1}\left\{\left[\frac{(1+\cos 2\psi)t_1}{2\lambda_1} + \frac{(1-\cos 2\psi)t_3}{2\lambda_3}\right](1+u_R) + \frac{1}{2}\sin 2\psi(\frac{t_1}{\lambda_1} - \frac{t_3}{\lambda_3})u_Z\right\}\mathrm{d}R\mathrm{d}Z \\
&= \int_{R,Z} RN_{i,1}\left[\frac{(1+\cos 2\psi)}{2}(\mu - \lambda_1^{-2}p) + \frac{(1-\cos 2\psi)t_3}{2\lambda_3}\right]\mathrm{d}R\mathrm{d}Z \\
&\quad + \int_{R,Z} RN_{i,1}\left[\frac{(1+\cos 2\psi)t_1}{2\lambda_1} + \frac{(1-\cos 2\psi)t_3}{2\lambda_3}\right]u_R\mathrm{d}R\mathrm{d}Z + \int_{R,Z} RN_{i,1}\frac{1}{2}\sin 2\psi(\frac{t_1}{\lambda_1} - \frac{t_3}{\lambda_3})u_Z\mathrm{d}R\mathrm{d}Z \\
&= \int_{R,Z} RN_{i,1}\left[\frac{1+\cos 2\psi}{2}\mu + \frac{(1-\cos 2\psi)t_3}{2\lambda_3}\right]\mathrm{d}R\mathrm{d}Z \\
&\quad + \int_{R,Z} RN_{i,1}\left\{\left[\frac{(1+\cos 2\psi)t_1}{2\lambda_1} + \frac{(1-\cos 2\psi)t_3}{2\lambda_3}\right]N_{j,1} + \frac{1}{2}\sin 2\psi(\frac{t_1}{\lambda_1} - \frac{t_3}{\lambda_3})N_{j,3}\right\}\mathrm{d}R\mathrm{d}Zu_j \\
&\quad - \int_{R,Z} R\frac{1+\cos 2\psi}{2}\lambda_1^{-2}N_{i,1}N_j'\mathrm{d}R\mathrm{d}Zp_j
\end{aligned}$$

Third term of (A.7),

$$\int_{R,Z} RN_{i,3}\left\{\frac{1}{2}\sin 2\psi(\frac{t_1}{\lambda_1} - \frac{t_3}{\lambda_3})(1 + u_R) + \left[\frac{(1 - \cos 2\psi)t_1}{2\lambda_1} + \frac{(1 + \cos 2\psi)t_3}{2\lambda_3}\right]u_Z\right\}\mathrm{d}R\mathrm{d}Z$$

$$= \int_{R,Z} \frac{1}{2}RN_{i,3}\sin 2\psi(\frac{t_1}{\lambda_1} - \frac{t_3}{\lambda_3})\mathrm{d}R\mathrm{d}Z$$

$$+ \int_{R,Z} RN_{i,3}\left\{\frac{1}{2}\sin 2\psi(\frac{t_1}{\lambda_1} - \frac{t_3}{\lambda_3})N_{j,1} + \left[\frac{(1 - \cos 2\psi)t_1}{2\lambda_1} + \frac{(1 + \cos 2\psi)t_3}{2\lambda_3}\right]N_{j,3}\right\}\mathrm{d}R\mathrm{d}Zu_j$$

Hence from equation (A.5), we obtain

$$\int_{R,Z} \frac{\mu}{R}N_iN_j + RN_{i,1}\left\{\left[\frac{(1 + \cos 2\psi)t_1}{2\lambda_1} + \frac{(1 - \cos 2\psi)t_3}{2\lambda_3}\right]N_{j,1} + \frac{1}{2}\sin 2\psi(\frac{t_1}{\lambda_1} - \frac{t_3}{\lambda_3})N_{j,3}\right\}$$

$$+ RN_{i,3}\left\{\frac{1}{2}\sin 2\psi(\frac{t_1}{\lambda_1} - \frac{t_3}{\lambda_3})N_{j,1} + \left[\frac{(1 - \cos 2\psi)t_1}{2\lambda_1} + \frac{(1 + \cos 2\psi)t_3}{2\lambda_3}\right]N_{j,3}\right\}\mathrm{d}R\mathrm{d}Zu_j$$

$$- \int_{R,Z} R\left[\frac{1}{R+u}N_i + \frac{1 + \cos 2\psi}{2}\lambda_1^{-2}N_{i,1}\right]N_j'\mathrm{d}R\mathrm{d}Zp_j = -\int_{R,Z}\mu N_i\mathrm{d}R\mathrm{d}Z \qquad \text{(A.8)}$$

$$- \int_{R,Z} RN_{i,1}\left[\frac{1 + \cos 2\psi}{2}\mu + \frac{(1 - \cos 2\psi)t_3}{2\lambda_3}\right]\mathrm{d}R\mathrm{d}Z - \int_{R,Z} \frac{1}{2}RN_{i,3}\sin 2\psi(\frac{t_1}{\lambda_1} - \frac{t_3}{\lambda_3})\mathrm{d}R\mathrm{d}Z$$

$$+ \int_Z (RN_iS_{11})|_{R_1}^{R_2}\mathrm{d}Z + \int_R R(N_iS_{31})|_{Z_1}^{Z_2}\mathrm{d}R$$

And the integrand of (A.6),

$$int_2 = RN_{i,1}\left\{\left[\frac{(1 + \cos 2\psi)t_1}{2\lambda_1} + \frac{(1 - \cos 2\psi)t_3}{2\lambda_3}\right]w_R + \frac{1}{2}\sin 2\psi(\frac{t_1}{\lambda_1} - \frac{t_3}{\lambda_3})(1 + w_Z)\right\}$$

$$+ RN_{i,3}\left\{\frac{1}{2}\sin 2\psi(\frac{t_1}{\lambda_1} - \frac{t_3}{\lambda_3})w_R + \left[\frac{(1 - \cos 2\psi)t_1}{2\lambda_1} + \frac{(1 + \cos 2\psi)t_3}{2\lambda_3}\right](1 + w_Z)\right\} \qquad \text{(A.9)}$$

First term of (A.9),

$$\int_{R,Z} RN_{i,1}\left\{\left[\frac{(1 + \cos 2\psi)t_1}{2\lambda_1} + \frac{(1 - \cos 2\psi)t_3}{2\lambda_3}\right]w_R + \frac{1}{2}\sin 2\psi(\frac{t_1}{\lambda_1} - \frac{t_3}{\lambda_3})(1 + w_Z)\right\}\mathrm{d}R\mathrm{d}Z$$

$$= \int_{R,Z} RN_{i,1}\frac{1}{2}\sin 2\psi(\frac{t_1}{\lambda_1} - \frac{t_3}{\lambda_3})\mathrm{d}R\mathrm{d}Z$$

$$+ \int_{R,Z} RN_{i,1}\left\{\left[\frac{(1 + \cos 2\psi)t_1}{2\lambda_1} + \frac{(1 - \cos 2\psi)t_3}{2\lambda_3}\right]N_{j,1} + \frac{1}{2}\sin 2\psi(\frac{t_1}{\lambda_1} - \frac{t_3}{\lambda_3})N_{j,3}\right\}\mathrm{d}R\mathrm{d}Zw_j$$

Using $\frac{t_3}{\lambda_3} = \mu - p\lambda_3^{-2}$, second term of (A.9),

$$\int_{R,Z} RN_{i,3}\left\{\frac{1}{2}\sin 2\psi(\frac{t_1}{\lambda_1} - \frac{t_3}{\lambda_3})w_R + \left[\frac{(1 - \cos 2\psi)t_1}{2\lambda_1} + \frac{(1 + \cos 2\psi)t_3}{2\lambda_3}\right](1 + w_Z)\right\}\mathrm{d}R\mathrm{d}Z$$

$$= \int_{R,Z} RN_{i,3}\left[\frac{(1 - \cos 2\psi)t_1}{2\lambda_1} + \frac{1 + \cos 2\psi}{2}(\mu - \lambda_3^{-2}p)\right]\mathrm{d}R\mathrm{d}Z$$

$$+ \int_{R,Z} RN_{i,3}\left\{\frac{1}{2}\sin 2\psi(\frac{t_1}{\lambda_1} - \frac{t_3}{\lambda_3})N_{j,1} + \left[\frac{(1 - \cos 2\psi)t_1}{2\lambda_1} + \frac{(1 + \cos 2\psi)t_3}{2\lambda_3}\right]N_{j,3}\right\}\mathrm{d}R\mathrm{d}Zw_j$$

$$= \int_{R,Z} RN_{i,3}\left[\frac{(1 - \cos 2\psi)t_1}{2\lambda_1} + \frac{1 + \cos 2\psi}{2}\mu\right]\mathrm{d}R\mathrm{d}Z$$

$$+ \int_{R,Z} RN_{i,3}\left\{\frac{1}{2}\sin 2\psi(\frac{t_1}{\lambda_1} - \frac{t_3}{\lambda_3})N_{j,1} + \left[\frac{(1 - \cos 2\psi)t_1}{2\lambda_1} + \frac{(1 + \cos 2\psi)t_3}{2\lambda_3}\right]N_{j,3}\right\}\mathrm{d}R\mathrm{d}Zw_j$$

$$- \int_{R,Z} R\frac{(1 + \cos 2\psi)}{2}\lambda_3^{-2}N_{j,3}N_j'\mathrm{d}R\mathrm{d}Zp_j$$

Hence from (A.6), we obtain

$$
\begin{aligned}
&\int_{R,Z} RN_{i,1} \left\{ \left[\frac{(1+\cos 2\psi)t_1}{2\lambda_1} + \frac{(1-\cos 2\psi)t_3}{2\lambda_3} \right] N_{j,1} + \frac{1}{2}\sin 2\psi(\frac{t_1}{\lambda_1} - \frac{t_3}{\lambda_3})N_{j,3} \right\} \\
&+ RN_{i,3} \left\{ \frac{1}{2}\sin 2\psi(\frac{t_1}{\lambda_1} - \frac{t_3}{\lambda_3})N_{j,1} + \left[\frac{(1-\cos 2\psi)t_1}{2\lambda_1} + \frac{(1+\cos 2\psi)t_3}{2\lambda_3} \right] N_{j,3} \right\} \mathrm{d}R\mathrm{d}Zw_j \\
&- \int_{R,Z} R\frac{1+\cos 2\psi}{2}\lambda_3^{-2}N_{i,3}N_j'\mathrm{d}R\mathrm{d}Zp_j = -\int_{R,Z} RN_{i,1}\frac{1}{2}\sin 2\psi(\frac{t_1}{\lambda_1} - \frac{t_3}{\lambda_3})\mathrm{d}R\mathrm{d}Z \\
&- \int_{R,Z} RN_{i,3} \left[\frac{(1-\cos 2\psi)t_1}{2\lambda_1} + \frac{1+\cos 2\psi}{2}\mu \right] \mathrm{d}R\mathrm{d}Z + \int_Z (RN_iS_{13})|_{R_1}^{R_2}\mathrm{d}Z + \int_R R(N_iS_{33})|_{Z_1}^{Z_2}\mathrm{d}R
\end{aligned}
\tag{A.10}
$$

Incompressible condition

$$
\lambda_1\lambda_3 = \lambda_2^{-1}
$$

expanding incompressible condition above, we have

$$
\frac{1}{R+u}u + u_R + (1+u_R)w_Z - u_Zw_R = 0 \tag{A.11}
$$

Integration (A.11), we obtain

$$
\begin{aligned}
&\int_{R,Z} RN_i' \left[\frac{1}{R+u}u + u_R + (1+u_R)w_Z - u_Zw_R \right] \mathrm{d}R\mathrm{d}Z \\
&= \int_{R,Z} RN_i' \left(\frac{1}{R+u}N_j + N_{j,1} \right) \mathrm{d}R\mathrm{d}Zu_j + \int_{R,Z} RN_i' \left[(1+u_R)N_{j,3} - u_ZN_{j,1} \right] \mathrm{d}R\mathrm{d}Zw_j
\end{aligned}
$$

Finally, we have

$$
\begin{aligned}
&\int_{R,Z} RN_i' \left(\frac{1}{R+u}N_j + N_{j,1} \right) \mathrm{d}R\mathrm{d}Zu_j \\
&+ \int_{R,Z} RN_i' \left[(1+u_R)N_{j,3} - u_ZN_{j,1} \right] \mathrm{d}R\mathrm{d}Zw_j = 0
\end{aligned}
\tag{A.12}
$$

Appendix B

Appendix B

In this appendix we present the mesh files used in Chapter 5. For details of the format of these files, we refer to the web page of libmesh: http://libmesh.sourceforge.net/publications.php.

B.1 Mesh files

The file `mesh.xda` for a tube with $A/B = 0.5, L/B = 1$ is give by

LIBM 0

4 # Num. of elements

6 # Num. nodes

20 # length of connectivity vector

6 # Num. boundary conds

65536 # string size

1 # Num. elements blocks

3 # Element types in each block

4 # Num. of elements in each block at each level

Id String

Title String

0 1 2 0 -1

0 2 3 1 -1

3 2 5 2 -1

2 4 5 3 -1

0.5 0 0

1 0 0

1 0.5 0

0.5 0.5 0

1 1 0

0.5 1 0

0 0 0

0 1 1

1 2 2

2 2 2

3 0 1

3 1 3

The file `mesh.xda` for a tube with $A/B = 0.5, L/B = 5$ is give by

LIBM 0

20 # Num. of elements

22 # Num. nodes

100 # length of connectivity vector

22 # Num. boundary conds

65536 # string size

1 # Num. elements blocks

3 # Element types in each block

20 # Num. of elements in each block at each level

Id String

Title String

0 1 2 0 -1

0 2 3 1 -1

3 2 4 2 -1

3 4 5 3 -1

5 4 6 4 -1

5 6 7 5 -1

7 6 8 6 -1

7 8 9 7 -1

9 8 10 8 -1

9 10 11 9 -1

11 10 13 10 -1

10 12 13 11 -1

13 12 15 12 -1

12 14 15 13 -1

15 14 17 14 -1

14 16 17 15 -1

17 16 19 16 -1

16 18 19 17 -1

19 18 21 18 -1

18 20 21 19 -1

0.5 0 0

1 0 0

1 0.5 0

0.5 0.5 0

1 1 0

0.5 1 0

1 1.5 0

0.5 1.5 0

1 2 0

0.5 2 0

1 2.5 0

0.5 2.5 0

1 3 0

0.5 3 0

1 3.5 0

0.5 3.5 0

1 4 0

0.5 4 0

1 4.5 0

0.5 4.5 0

1 5 0

0.5 5 0

0 0 0

0 1 1

1 2 2

2 1 1

3 2 2

4 1 1

5 2 2

6 1 1

7 2 2

8 1 1

9 2 2

10 2 2

11 0 1

12 2 2

13 0 1

14 2 2

15 0 1

16 2 2

17 0 1

18 2 2

19 0 1

19 1 3

References

[1] M. Amabili and M.P. Païdoussis. Review of studies on geometrically nonlinear vibrations and dynamics of circular cylindrical shells and panels, with and without fluid-structure intersection. *Applied Mechanics Reviews*, 56:349–381, 2003.

[2] M. Anliker, W.E. Moritz, and E. Ogden. Transmission characteristics of axial waves in blood vessels. *Journal of Biomechanics*, 1:235–246, 1968.

[3] B. Bader, R. Hooper, T. Kolda, R. Pawlowski, E. Phipps, and A. Salinger. Nox and loca: Object-oriented nonlinear solver and continuation packages. *The Trilinos Project website http://trilinos.sandia.gov/.*

[4] S. Balay, K. Buschelman, V. Eijkhout, W.D. Gropp, D. Kaushik, M.G. Knepley, L.C. McInnes, B.F. Smith, and H. Zhang. Petsc users manual. *Technical Report ANL-95/11 – Revision 3.0.0, Argonne National Laboratory*, 2008.

[5] F.C. Bardi and S. Kyriakides. Plastic buckling of circular tubes under axial compression–part i: Experiments. *International Journal of Mechanical Sciences*, 48:830–841, 2006.

[6] F.C. Bardi, S. Kyriakides, and H.D. Yun. Plastic buckling of circular tubes under axial compression–part ii: Analysis. *International Journal of Mechanical Sciences*, 48:842–854, 2006.

[7] S.B. Batdorf. A simplified method of elastic stability analysis for thin cylindrical shells. *NACA Report*, page 874, 1947.

[8] K.J. Bathe. *Finite ELement Procedures*. Prentice Hall, New Jersey, 1996.

[9] M.F. Beatty and P. Dadras. Some experiments on the elastic stability of some highly elastic bodies. *International Journal of Engineering Science*, 14:233–238, 1968.

[10] C.D. Bertram. Two modes of instability in a thick-walled collapsible tube conveying a flow. *Journal of Biomechanics*, 15:223–224, 1982.

[11] C.D. Bertram. The effects of wall thickness, axial strain and end proximity on the pressure-area relation of collapsible tubes. *Journal of Biomechanics*, 20:863–876, 1987.

[12] C.D. Bertram and N.S.J. Elliot. Flow-rate limitation in a uniform thin-walled collapsible tube, with comparison to a uniform thick-walled tube and a tube of tapering thickness. *Journal of Fluids and Structures*, 17:541–559, 2003.

[13] C.D. Bertram, C.J. Raymond, and T.J. Pedley. Mapping of instabilities for flow through collapsed tubes of differing length. *Journal of Fluids and Structures*, 4:125–153, 1990.

[14] C.D. Bertram, C.J. Raymond, and T.J. Pedley. Application of dynamical system concepts to the analysis of self-excited oscillations of a collapsible tube conveying a flow. *Journal of Fluids and Structures*, 5:391–426, 1991.

[15] G. Buzzi-Ferraris. *Scientific C++: Building Numerical Libraries the Object-Oriented Way.* Addison-Wesley, Reading, MA, 1993.

[16] G. Buzzi-Ferraris. *Object-Oriented Analysis and Design with Applications.* Benjamin-Cummings, Redwood City, CA, 1994.

[17] Z.X. Cai and X.Y. Luo. A fluidbeam model for flow in collapsible channel. *Journal of Fluids and Structures*, 17 (1):123–144, 2003.

[18] D.M. Cannell. *George Green mathematician and physicist.* The Athlone Press, London, 1993.

[19] G.F. Carey, M. Anderson, B. Carnes, and B. Kirk. Some aspects of adaptive grid technology related to boundary and interior layers. *J. Comput. Appl. Math.*, 166(1):5586, 2004.

[20] H. Demiray. Nonlinear waves in a prestressed thick elastic tube filled with an invisid fluid. *International Journal of Engineering Science*, 34:1519–1530, 1996.

[21] H. Demiray. Nonlinear wave modulation in a fluid filled thick elastic tube. *International Journal of Engineering Science*, 36:1061–1082, 1998.

[22] Hinton E. and Campbell J. Local and global smoothing of discontinuous finite element function using a least squares method. *Int. J. Numer. Meth. Eng.*, 8:461–480, 1974.

[23] H.A. Erbay and H. Demiray. Finite axisymmetric deformations of elastic tubes: An approximate method. *Journal of Engineering Mathematics*, 29:451–472, 1995.

[24] J.E. Flaherty, J.B. Keller, and S.I. Rubinow. Post buckling behavior of elastic tubes and rings with opposite sides in contact. *SIAM Journal of Applied Mathematics*, 23:446–455, 1972.

[25] W. Flügge. *Stresses in Shells.* Springer, Berlin, second edition, 1973.

[26] Y.B. Fu and R.W. Ogden. Nonlinear stability analysis of pre-stressed elastic bodies. *Continuum Mech. Thermodyn.*, 11:141172, 1999.

[27] Y.B. Fu and R.W. Ogden. *Nonlinear Elasticity: Theroy and Application, volume 283 of London Mathematical Society Lecture Notes Series.* Cambridge University Press, 2001.

[28] A.E. Green, R.S. Rivilin, and R.T. Shield. General theory of small elastic deformations superposed on finite elastic deformations. *Proceedings of the Royal Society of London A*, 211:128–154, 1952.

[29] D.E. Gregg and L.C. Fisher. *Blood supply to the heart. In Handbook of Physiology (ed. Hamilton W.F. and Dow P.).* American Physiological Society, Washington D.C., 1963.

[30] A.C. Guyton and L.H. Adkins. Quantitative aspects of the collapse factor in relation to venous return. *American Journal of Physiology*, 177:523–527, 1954.

[31] Si H. A quality tetrahedral mesh generator and a 3d delaunay triangulator. *http://tetgen.berlios.de/.*

[32] D.M. Haughton and R.W. Ogden. On the incremental equations in non-linear elasticity–i. membrane theory. *Journal of the Mechanics and Physics of Solids*, 26:93–110, 1978a.

[33] D.M. Haughton and R.W. Ogden. On the incremental equations in non-linear elasticity–ii. bifurcation of pressured spherical shells. *Journal of the Mechanics and Physics of Solids*, 26:111–138, 1978b.

[34] D.M. Haughton and R.W. Ogden. Bifurcation of inflated circular cylinders of elastic material under axial loading–i. membrane theory for thin-walled tubes. *Journal of the Mechanics and Physics of Solids*, 27:179–212, 1979a.

[35] D.M. Haughton and R.W. Ogden. Bifurcation of inflated circular cylinders of elastic material under axial loading–ii. exact theory for thick-walled tubes. *Journal of the Mechanics and Physics of Solids*, 27:489–512, 1979b.

[36] M. Heil. The stability of cylindrical shells conveying viscous flow. *Journal of Fluids and Structures*, 10:173–196, 1996.

[37] M. Heil. Stokes flow in collapsible tubes: computation and experiment. *Journal of Fluid Mechanics*, 353:258–312, 1997.

[38] M. Heil and T.J. Pedley. Large axisymmetric deformation of a cylindrical shell conveying a viscous flow. *Journal of Fluids and Structures*, 9:237–256, 1995.

[39] M. Heil and T.J. Pedley. Large post-buckling deformations of cylindrical shells conveying viscous flow. *Journal of Fluids and Structures*, 10:565–599, 1996.

[40] B.P.C. Ho and S. Cheng. Some problems in stability of heterogeneous aeolotropic cylindrical shells under combined loading. *AIAA Journal*, 1:1603–1607, 1963.

[41] O.E. Jensen and M. Heil. High-frequency self-excited oscillations in a collapsible-channel flow. *Journal of Fluid Mechanics*, 481:235–268, 2003.

[42] R.D. Kamm and T.J. Pedley. Flow in collapsible tubes: a brief review. *ASME Journal of Biomechanical Engineering*, 111:177–179, 1989.

[43] D.W. Kelly, J. P. Gago, O.C. Zienkiewicz, and I. Babuska. A posteriori error analysis and adaptive processes in the finite element method: Part i error analysis. *Int. J. Num. Meth. Engng.*, 19:15931619, 1983.

[44] B. Kirk, J.W. Peterson, R.H. Stogner, and G.F. Carey. Libmesh: A c++ library for parallel adaptive mesh refinement/coarsening simulations. *Engineering with Computers*, 22:237–254, 2006.

[45] B.S. Kirk. *Adaptive Finite Element Simulation of Flow and Transport Applications on Parallel Computers*. The University of Texas at Austin, 2007.

[46] A.N. Kounadis. Recent advances on postbuckling analyses of thin-walled structures: Beams, frames and cylindrical shells. *Journal of Constructional Steel Research*, 62:1101–1115, 2006.

[47] A. Libai and J.G. Simmonds. *The Nonlinear Theory of Elastic Shells*. Cambridge University Press, Cambridge, 1998.

[48] X.Y. Luo and T.J. Pedley. A numerical simulation of steady flow in a 2d collapsible channel. *Journal of Fluids and Structures*, 9:149–174, 1995.

[49] X.Y. Luo and T.J. Pedley. A numerical simulation of unsteady flow in a 2d collapsible channel. *Journal of Fluid Mechanics*, 314:191–225, 1996.

[50] X.Y. Luo and T.J. Pedley. The effects of the wall inertia on the 2d collapsible channel flow. *Journal of Fluid Mechanics*, 363:253–280, 1998.

[51] X.Y. Luo and T.J. Pedley. Flow limitation and multiple solutions in 2d collapsible channel flow. *Journal of Fluid Mechanics*, 420:301–324, 2000.

[52] A. Marzo, X.Y. Luo, and C.D. Bertram. Three-dimensional collapse and steady flow in thick-walled flexible tubes. *Journal of Fluids and Structures*, 20:817–835, 2005.

[53] T.B. Moodie and G.E. Swaters. Nolinear waves and shock calculations for a hyperelastic fluid-filled tube. *Quarterly Applied Mathematics*, 47:705–732, 1989.

[54] W.A. Nash. Buckling of thin cylindrical shells subject to hydrostatic pressure. *Journal of the Aeronautical Sciences*, 21:354–355, 1954.

[55] P.V. Negrón-Marrero. An analysis of the linearized equations for axisymmetric deformations of hyperelastic cylinders. *Mathematics and Mechanics of Solids*, 4:109–133, 1999.

[56] J.L. Nowinski and M. Shahinpoor. Stability of an elastic circular tube of arbitrary wall thickness subjected to an external pressure. *International Journal of Non-Linear Mechanics*, 4:143–158, 1969.

[57] R.W. Ogden. Large deformation isotropic elasticity i: On the correlation of theory and experiment for incompressible rubberlike solids. *Proceedings of the Royal Society of London A*, 326:565–584, 1972.

[58] R.W. Ogden. On stress rates in solid mechanics with application to elasticity theory. *Proceedings of the Cambridge Philosophical Society*, 75:303–319, 1974.

[59] R.W. Ogden. Elastic deformation of rubberlike solids. *Mechanics of Solids*, The Rodney Hill 6oth Anniversary Volume:499–537, 1982.

[60] R.W. Ogden. *Non-linear Elastic Deformations*. Dover Publications, New York, 1997.

[61] T.J. Pedley. Longitudinal tension variation in collapsible channels: a new mechanism for the breakdown of steady flow. *ASME Journal of Biomechanical Engineering*, 114:60–67, 1992.

[62] W.H. Press, S.A. Teukolsky, W.T. Vetterling, and B.P. Flannery. *Numerical Recipes in Fortran The Art of Scientific Computing Second Edition*. Cambridge University Press, Cambridge, 1992.

[63] S. Rodbard and L.H. Adkins. A hydrodynamics mechanism for autoregulation of flow. *Cardiologia*, 48:532–535, 1966.

[64] G. Rudinger. Shock waves in a mathematical model of the aorta. *Journal of Applied Mechanics*, 37:34–37, 1970.

[65] R.A. Scroggs, E.A. Patterson, and S.B.M. Beck. Numerical fluidstructure interaction model of a collapsible tube using ls-dyna. *IUTAM Symposium on Flowin Collapsible Tubes and Past other Highly Compliant Boundaries, Warwick, UK*.

[66] L.H. Sobel. Effects of boundary conditions on the stability of cylinders subject to lateral and axial pressure. *AIAA Journal*, 2:1437–1440, 1964.

[67] R.H. Stogner. *Parallel Adaptive C^1 Macro-Elements for Nonlinear Thin Film and Non-Newtonian Flow Problems*. The University of Texas at Austin, 2008.

[68] B. Stroustrup. *The C++ Progamming Language*. Addison-Wesley, 2007.

[69] R. J. Tait, D. J. Steigmann, and J. L. Zhong. Finite twist and extension of a cylindrical elastic membrane. *Acta Mechanica*, 117(1):129–143, 1996.

[70] D. Tang and C. Yang. 3-d steady and unsteady blood flowin stenotic collapsible arteries with symmetric and asymmetric stenoses. *Recent Advances in Biomechanics,Proceedings of First International Young Investigators Workshop on Biomechanics, Beijing*, 121:171191, 2001.

[71] D. Tang, J. Yang, and D.N. Ku. A nonlinear axisymmetric model with fluidwall interactions for viscous flows in stenotic elastic tubes. *ASME Journal of Biomechanical Engineering*, 121:494501, 1999.

[72] R. von Mises. Der kritische außendruck zylindrischer rohre. *VDI Zeitschrift*, 58:750–755, 1914.

[73] A.S.D. Wang and A. Ertepinar. Stability and vibrations of elastic thick-walled cylindrical and spherical shells subjected to pressure. *International Journal of Non-Linear Mechanics*, 7:539–555, 1972.

[74] M. Weissman and L. Mockros. The mechanics of a collapsing tube heart pump. *International Journal of Mechanical Sciences*, 9:113–121, 1967.

[75] N. Yamaki. Buckling of circular cylindrical shells under external pressure. *Reports of the Institute of High Speed Mechanics*, 20:35–55, 1969.

[76] N. Yamaki. Influence of prebuckling deformation on the buckling of circular cylindrical shells under external pressure. *Reports of the Institute of High Speed Mechanics*, 21:81–104, 1970.

[77] N. Yamaki. *Elastic Stability of Circular Cylindrical Shells*. North-Holland, Amsterdam, 1984.

[78] Y. Zhu, X.Y. Luo, and R.W. Ogden. Asymmetric bifurcations of thick-walled circular cylindrical elastic tubes under axial loading and external pressure. *International Journal of Solids and Structures*, 45:3410–3429, 2008.

[79] Y. Zhu, X.Y. Luo, and R.W. Ogden. Nonlinear axisymmetric deformations of an elastic tube under external pressure. *European Journal of Mechanics - A/Solids*, In Press, Accepted Manuscript:doi:10.1016/j.euromechsol.2009.10.004, 2010.

[80] O.C. Zienkiewicz, R.L. Taylor, and J.Z Zhu. *The finite element method its basis and fundamentals*. Elsevier Butterworth-Heinemann, Oxford, 2005.